

Materials Science and Design for Germanium Monolithic Light Source on Silicon

by

Yan Cai

B. E. Materials Science and Engineering
Tsinghua University, 2009

Submitted to the Department of Materials Science and Engineering
in Partial Fulfillment of the Requirement for the Degree of

Doctor of Philosophy in Materials Science and Engineering
at the
Massachusetts Institute of Technology

September 2014

© Massachusetts Institute of Technology. All rights reserved.

Signature of Author: _____

Department of Materials Science and Engineering
August 11th, 2014

Certified by: _____

Lionel C. Kimerling
Thomas Lord Professor of Materials Science and Engineering
Thesis Supervisor

Certified by: _____

Jurgen Michel
Senior Research Scientist
Thesis co-advisor

Accepted by: _____

Gerbrand Ceder
Chair, Departmental Committee on Graduate Students

Materials Science and Design for Germanium Monolithic Light Source on Silicon

by

Yan Cai

Submitted to the Department of Materials Science and Engineering
on August 11, 2014 in Partial Fulfillment of the Requirements for the Degree of
Doctor of Philosophy in Materials Science and Engineering

ABSTRACT

Germanium (Ge) is an optically active material with the advantages of Si-CMOS compatibility and monolithic integration. It has great potential to be used as the light emitter for Si photonics. Tensile strain and n-type doping are two key properties in Ge to achieve optical gain. This thesis mainly focuses on: (1) physical understandings of the threshold behavior of Ge-on-Si bulk laser and the temperature dependent performance; (2) process developments to grow and planarize the epitaxial Ge on Si in oxide trenches and corners; (3) introduction of n-type dopant into Ge-on-Si thin films while studying the threading dislocation behavior in n-Ge during annealing; (4) Design an external cavity Ge laser integrated with Si waveguides for a low threshold current and single mode operation.

Heavy n-type doping was observed to change the Ge electronic band structure by band gap narrowing effect. We also found a failure of using a simple Drude model to explain free carrier absorption in n-Ge. We modified the optical gain simulation based on the above two observations in Ge. We found a broad gain bandwidth of ~ 200 nm from 1550 nm to 1750 nm and a higher net materials gain. We predicted a theoretical lasing threshold current density of $5\sim 10$ kA/cm² in the bulk Ge laser device with the n-type doping of mid- 10^{19} cm⁻³ at room temperature. We also predicted the Ge laser device would have better temperature stability regarding the threshold current compared to the III-V laser.

Single crystalline Ge was epitaxial grown on Si in oxide trenches using ultra high vacuum chemical vapor deposition. The selective growth lead to the faceting in Ge because of the different growth rates of crystal orientations. We developed a suitable photolithography and oxide etch process to get the vertical oxide sidewall for Ge trench filling. We also tested the Ge growth in the T-shape corners to improve the reflectivity at the waveguide end. The T-shape structure was also useful for the Ge/Si waveguide coupling in the external cavity laser. Furthermore, we developed a chemical mechanical polishing (CMP) process for the over-grown Ge waveguides. The Ge CMP process was selective to oxide, flexible to change in the CMP rate by DI water dilution and controllable for a minimum dishing of Ge in the oxide trenches.

N-type doping helped to increase the direct band transition in Ge for light emission. We developed a delta-doping method to grow a dopant source called “delta doping layer” on the

single crystalline Ge layer without introducing extra defects. We then used rapid thermal annealing to drive the dopant into the underlying Ge layer. The dopant enhanced diffusion was discovered to speed up the drive-in process. The active n-type concentration in Ge could reach up to $5 \times 10^{19} \text{ cm}^{-3}$ using the delta doping source and annealing process. Since the dopant source layer had a disrupted Ge growth, we used the developed CMP process to remove it after the dopant drive-in. A comprehensive dopant diffusion simulation was developed to predict the annealing temperature and time to achieve high n-type doping and uniform distribution. We used plan-view transmission electron microscopy to examine the threading dislocation density (TDD) in n-Ge for both blanket films and trench grown waveguides. We found a high TDD of $\sim 1 \times 10^8 \text{ cm}^{-2}$ in 1 μm thick blanket Ge with doping of $3 \times 10^{18} \text{ cm}^{-3}$ after high temperature annealing at 850 $^\circ\text{C}$ for 40 min. The TDD is $1 \times 10^9 \text{ cm}^{-2}$ in the 300 nm thick and 1 μm wide Ge waveguide. We examined the effects of annealing temperature, Ge thickness, Si/Ge inter-diffusion and trench width on the threading dislocation behavior. However, we have not found the exact reason causing the high TDD and therefore, further study is required on the TDD reduction for the Ge waveguide.

Finally, we designed an external cavity Ge laser using distributed Bragg reflector (DBR) gratings on Si waveguides. A detailed discussion on the cross section design was presented to mitigate the internal optical loss from claddings and metal layers and to improve the current injection uniformity across the Ge waveguide. The aim of the DBR grating design was to achieve a single mode operation by controlling the full width half maximum of the grating reflectance spectrum. We also discussed the coupling between Ge and Si waveguides and different designs were presented to increase the coupling efficiency.

Thesis Supervisor: Lionel C. Kimerling

Title: Thomas Lord Professor of Materials Science and Engineering

Thesis Co-advisor: Jurgen Michel

Title: Singapore Research Professor; Senior Research Scientist

Acknowledgement

I joined EMAT group at MIT in the fall of 2009 after my four year undergraduate study at Tsinghua University in China. I came with the ambition to become both a critical-thinking scientist with solid theoretical background and an innovative engineer with practical hands-on experience. I came with the desire to learn, to work in and to experience the different research and cultural environment from China. Five years later, I'm here to be graduating, with a lot to recall, to share and to thank. This five year will be my most cherished period in my lifetime with so many impressive and happy memories with my lovely EMAT family, my friends and my husband.

I first would like to thank my thesis supervisor Prof. Lionel C. Kimerling. Kim's extraordinary knowledge in materials science and Si photonics always impresses me and inspires me to keep learning and understanding the unknowns. Kim likes to encourage me to think independently, to challenge me to think differently and to guide me to solve a problem in a logical and rational way. Kim's guidance and help to my research and thesis are tremendous. His optimistic attitude to research and to life is also something I have to remind myself. I feel very lucky to have Kim as my thesis supervisor. The influence will not only be the past five years, but throughout my entire lifetime.

I would like to thank my thesis co-advisor Dr. Jurgen Michel for bringing me into EMAT and for guiding me on the Ge light emitter project. I talk with Jurgen almost every week on all kinds of details in my research. He will be happy for me about every small progress in the project. He is also very patient to correct me for my mistakes and to help me figure out the reason of any failure. I can find his corrections in all my publications, presentations and also in this thesis. I admire Jurgen's rigorous attitude to research and his sense of humor to life. He is the role model to me.

I also want to deliver my thank to Dr. Anuradha Agarwal. Anu is not my direct advisor on this thesis but she advises on the Ge application in mid-IR region. Anu is very open-minded to listen to what I am thinking and also very sharp to help me make decisions. Another thing I always want to learn from her is her ability to balance her family and research as a successful women scientist.

Dr. Xiaoman Duan is someone I don't know how much thank I should say to her. She is the "Angel Mom" that cares me and cares us with all her heart. She loves everyone and I also love her as my second Mom. She shares with me her lifetime experience as a Chinese in US and teaches me to make friends with everyone and never hesitate to help anyone even if my help is tiny. I also want to thank her for the TEM imaging and analysis discussion.

In the last five years, there are so many people joining and leaving EMAT group. Everyone helps me a lot and makes a difference to my life here. Rodolfo Camacho is my mentor, my labmate and also my good friend. We worked together on the Ge light emitter project very closely for four years. His energy and enthusiasm on the research always encourages me to work harder and learn more. He is a talented researcher and I really enjoyed the collaboration with him. I am very proud to say that we made the first electrically pumped Ge laser together.

Prof. Jifeng Liu was a previous student and research scientist in EMAT. Although he left when I just joined the group, he is always ready to answer all kinds of questions from me regarding the Ge material, the growth tube, the theory and so on. I appreciate his continuous and unrequired help.

Dr. Marco Romagnoli was a visiting scientist in our group. We worked together on the Ge laser characterization and advanced laser design. His background on electrical engineering helped tremendously on the laser project.

Jonathan Bessette was a post-doc working on the Ge laser project. He taught me and Rodolfo a lot on the optical setup and characterization. He is like my elder brother, sharing with me his knowledge on the phd life, especially when I encounter difficulties.

Lin Zhang is a post-doc now in the group, working together with me on the Ge laser project. He is an expert on the non-linear optics and optical simulation. The discussion with him is always very fruitful because he has a lot of new ideas.

Lirong Z. Broderick is like my elder sister in the group. We always have lunch together and have discussions about research, family, TV shows and a lot. She is both a good experimentalist and a good theorist. I miss her so much when she left the group last year.

Brian Albert, Brian Pearson and I are currently taking the responsibility of UHVCVD tool and also the three main students working on the Ge related devices. They are both very gentle, doing all the heavy work for me. They are very responsible so that I can call them for help if I meet any problem.

Zhaohong Han and Wei Yu are the two successors to work on Ge laser project. They are very smart and eager to learn everything. We also organize Chinese Association of Science and Technology (CAST) together. Although they are younger than me, I feel like that they take care of me more when we go out for vacations for example.

Tim Milakovich is a graduate student in Prof. Fitzgerald group and he is also an expert on TEM spectroscopy. We collaborate on the work of the threading dislocation analysis in n-Ge. He is so helpful and responsible that he will spend hours for the TEM sample preparation and imaging on weekends. This piece of work is very important for the next generation devices.

I worked in MTL a lot for the device fabrication so I want to thank all the technicians helped me there. And I want to specially thank Bernard Alamariu, Paul Tierney, Eric Lim, Paudely Zamora and Kurt Broderick for their tremendous help to me on the training, discussion and repairing tools I desperately want to use as soon as possible.

I have another long list to thank who are my friends regardless how long we have known each other. I cannot list everyone's name but they are all in my heart. The happy time we spent together will be my treasure forever.

My last and deepest thank will give to my parents and my husband, Yinxuan Yang for their continuous support. My parents gave me a lot of freedom to choose my own way and to chase my dream across the Pacific Ocean. We have twelve-hour time difference so that we mostly talk through video chat once a week on the weekend. They told me when I left my hometown that, "whenever you want to come back, just turn back your head, we are always here". I want to thank Yinxuan for his eight year's company from Beijing to Boston. We share the same interest. We support, encourage and love each other. He is my soul mate. He is the one I can rely on no matter what kind of difficulty I meet. I want to say thank you and love you forever.

Table of Contents

Abstract.....	3
Acknowledgement.....	5
List of Figures.....	10
List of Tables	18
Chapter 1. Introduction	19
1.1 Silicon Photonics.....	21
1.1.1 Bandwidth, Power and Market	22
1.1.2 Optical Components in Photonic Network.....	25
1.2 Ge Light Emitters for Silicon Photonics	29
1.2.1 Ge Band Structure Engineering	29
1.2.2 Literature Review on Ge-on-Si Material and Devices	30
1.2.3 General Laser Physics and Theory	35
1.3 Thesis Goal and Outline.....	39
Chapter 2. Theoretical Prediction of Threshold Current Behavior of Bulk Ge Laser	41
2.1 Effects of Heavy n-type Doping.....	42
2.1.1 Free Carrier Absorption in Ge	42
2.1.2 Band Gap Narrowing Effect due to Heavy Doping.....	44
2.2 Optical Gain Modeling.....	47
2.2.1 Optical Gain.....	48
2.2.2 Net Materials Gain.....	52
2.2.3 Extended Ge Gain Bandwidth to Mid-IR.....	55
2.3 Temperature Dependent Optical Performances of Ge	57
2.3.1 Photoluminescence Dependence with Temperature.....	57
2.3.2 Photoluminescence Simulation.....	60
2.3.3 Materials Gain Dependence with Temperature	69
2.4 Threshold Current Density Prediction.....	72

Chapter 3. Ge Epitaxial Growth on Si and Planarization.....	78
3.1 Ge Epitaxy using UHVCVD.....	79
3.1.1 Two-step Ge Epitaxial Growth on Si	80
3.1.2 Ge Selective Growth.....	83
3.1.3 Ge Bufferless Growth.....	92
3.2 Chemical Mechanical Polishing of Ge.....	96
3.2.1 Experiments Details.....	97
3.2.2 Ge Removal Rate with Slurry Composition	99
3.2.3 Ge Removal Rate with Pattern Density	102
3.2.4 Waveguide Characterization after CMP.....	106
3.2.5 CMP for Ge Waveguides with Extremely Low Pattern Density.....	108
Chapter 4. N-type Doping and Dopant Diffusion in Ge	112
4.1 Ge n-type Doping.....	113
4.1.1 n-Ge with <i>in situ</i> Doping	117
4.1.2 n-Ge with Dopant Source	119
4.1.3 Dopant Drive-in Process through Annealing.....	122
4.2 Dopant Diffusion Behavior in Ge	126
4.3 Threading Dislocation in n-Ge.....	132
4.3.1 Effect of Annealing Temperature	134
4.3.2 Effect of the Ge Layer Thickness	136
4.3.3 Effect of Si/Ge Inter-diffusion.....	139
4.3.4 Effect of the Trench Width.....	140
Chapter 5. Ge External Cavity Laser Design on SOI.....	145
5.1 Internal Optical Loss	146
5.2 Current Injection in Ge Laser on SOI	152
5.2.1 Physical Models in Sentaurus.....	152
5.2.2 Sentaurus Simulation Results	154
5.3 Distributed Bragg Reflector Design and the Corresponding Coupling for Ge Laser on SOI	161
5.3.1 Ge DBR Laser Design	161

5.3.2 Ge/Si Waveguide Coupling Design.....	166
5.4 Fabrication Process Flows.....	172
Chapter 6. Summary and Future Work	176
6.1 Summary	176
6.2 Future Work	179
Appendix.....	183
Appendix I. Phosphorus Diffusion Modeling in n-Ge	183
Appendix II. Electrical Simulation of Ge pnn Junction	187
References	190

List of Figures

Figure 1.1	Silicon photonics application trend to fill the gap between electrical interconnect and fiber optical interconnect with the requirements of shorter distance and higher bandwidth.....	23
Figure 1.2	Network energy cost per bit calculation from DSENT model including optical devices and electrical backend circuitry.....	24
Figure 1.3	Schematic of an on-chip optical interconnect with optical components of laser, modulator, photodetector and other passive resonators and waveguides	25
Figure 1.4	Ge band structures under injection. (a) bulk Ge (b) Ge with 1.8% tensile strain (c) Ge with 0.25% tensile strain and n-type doping concentration of $7.6 \times 10^{19} \text{ cm}^{-3}$	30
Figure 2.1	Free electron absorption coefficients at different electron injection levels calculated from first principles (black) and from λ^2 -dependent model (red)..	45
Figure 2.2	Direct and indirect BGN results in n-Ge at room temperature (T=300K).....	46
Figure 2.3	Population inversion factor with injected carrier density ranging from $1 \times 10^{18} \text{ cm}^{-3}$ to $1 \times 10^{20} \text{ cm}^{-3}$ for Ge with $4.5 \times 10^{19} \text{ cm}^{-3}$ n-type doping and 0.25% tensile strain at $\lambda=1600 \text{ nm}$	49
Figure 2.4	Optical gain from the direct transition in 0.25% tensile strained, n+ Ge with $N=4.5 \times 10^{19} \text{ cm}^{-3}$ at different injected carrier densities..	51
Figure 2.5	Gain spectra from the direct transition in 0.25% tensile strained n+ Ge with $N=4.5 \times 10^{19} \text{ cm}^{-3}$ at different injected carrier densities.	51

Figure 2.6	Gain from the direct transition, free carrier loss and net gain as a function of injected carrier density in 0.25% tensile strained, n+ Ge with $N=4.5 \times 10^{19} \text{ cm}^{-3}$ at $\lambda=1600 \text{ nm}$	53
Figure 2.7	Gain from the direct transition, free carrier loss and net gain as a function of injected carrier density in 0.25% tensile strained, n+ Ge with $N=4.5 \times 10^{19} \text{ cm}^{-3}$ at $\lambda=1700 \text{ nm}$	54
Figure 2.8	Net materials gain as a function of injected carrier density in 0.25% tensile strained, n+ Ge with $N=4.5 \times 10^{19} \text{ cm}^{-3}$ at $\lambda=1550 \text{ nm}$, 1600 nm , 1650 nm and 1700 nm	54
Figure 2.9	Optical gain spectra for Ge with tensile strain of 0.25%, 1.8% and 2.5%.	56
Figure 2.10	Optical gain spectra for un-doped Ge and n-type doped Ge with 1.8% and 2.5%.	56
Figure 2.11	Photoluminescence spectra measured for the Ge thin film with n-type doping concentration of $3 \times 10^{18} \text{ cm}^{-3}$ at temperatures of $-40 \text{ }^\circ\text{C}$, $0 \text{ }^\circ\text{C}$, $40 \text{ }^\circ\text{C}$, $80 \text{ }^\circ\text{C}$ and $120 \text{ }^\circ\text{C}$	59
Figure 2.12	FWHM for PL spectra for different Ge samples compared to $2kT$ broadening	59
Figure 2.13	Normalized maximum intensity from PL spectra with temperature for the Ge-on-Si thin film with $N=1 \times 10^{19} \text{ cm}^{-3}$	61
Figure 2.14	Photoluminescence spectrum measured for the Ge thin film with n-type doping concentration of $3 \times 10^{18} \text{ cm}^{-3}$ at $40 \text{ }^\circ\text{C}$	67
Figure 2.15	Calculated photoluminescence spectra for the Ge thin film with n-type doping concentration of $3 \times 10^{18} \text{ cm}^{-3}$ at temperatures of $-40 \text{ }^\circ\text{C}$, $0 \text{ }^\circ\text{C}$, $40 \text{ }^\circ\text{C}$, $80 \text{ }^\circ\text{C}$ and $120 \text{ }^\circ\text{C}$	67
Figure 2.16	Maximum PL intensity with temperature for the Ge thin film doped to $3 \times 10^{18} \text{ cm}^{-3}$	68

Figure 2.17	Maximum PL intensity with temperature for the Ge thin film doped to $1 \times 10^{19} \text{ cm}^{-3}$	69
Figure 2.18	(a) Net materials gain simulation with temperature. Gain curves are plotted for Ge doped to $1 \times 10^{19} \text{ cm}^{-3}$, $5 \times 10^{19} \text{ cm}^{-3}$ and $7 \times 10^{19} \text{ cm}^{-3}$ respectively. (b) The effective injected carriers for radiative recombination under various temperatures considering the non-radiative recombination.	71
Figure 2.19	Theoretical estimation of the threshold current density for Ge with different n-type doping levels.	74
Figure 2.20	Laser threshold current densities with temperature ranging from 200 K to 450 K for Ge doped to different levels.	74
Figure 3.1	Plan view TEM image of misfit dislocations in the Ge buffer	81
Figure 3.2	SEM image of the positive photoresist after hard baking at 130 °C for 1min	86
Figure 3.3	SEM images of oxide sidewall angles after dry etch for (a) device waveguides and (b) packed waveguides.	86
Figure 3.4	Cross sectional SEM image of a Ge waveguide selectively grown on Si	87
Figure 3.5	Cross sectional SEM images for over-grown Ge (a) roof-top structure (b) mushroom-like structure	88
Figure 3.6	Cross sectional TEM images for Ge waveguide grown in oxide trench (a) overview image (b) enlarged image of Ge/Si interface (c) enlarged image of Ge/oxide interface	89
Figure 3.7	Photoresist after exposure and development showing rounded corners at the resist ends	91
Figure 3.8	Selective Ge growth in rounded corners.	91

Figure 3.9	Ge selective growth in a T-shape corner	92
Figure 3.10	SEM of Ge by bufferless growth in different oxide trench widths of 750 nm, 1000 nm, 1250 nm, 2250 nm, 5250 nm and 10250 nm	94
Figure 3.11	SEM of Ge by bufferless growth with 1250 nm oxide trench width and the waveguide is along the direction of 45 ° to the [110] wafer flat	95
Figure 3.12	Cross sectional TEM images of 500 nm wide Ge waveguides (a) buffered growth (b) bufferless growth.....	96
Figure 3.13	Cross sectional SEM image of 1µm wide Ge waveguide grown in oxide trench on Si substrate.....	99
Figure 3.14	Ge dissolution rate change with slurry pH values using W2000-C.....	101
Figure 3.15	Ge removal rate variation with pattern density for CMP Slurry W2000-B and W2000-C.....	102
Figure 3.16	(a) Cross sectional SEM graphs for Ge waveguides with various pattern densities after CMP for 80s using slurry W2000-C. (b) The corresponding step height profiles for each pattern density measured by AFM.....	104
Figure 3.17	Schematic graphs of the Ge selective growth geometries before CMP for simulation.....	105
Figure 3.18	(a) 2D profile of a 1 µm wide waveguide spaced by 10 µm oxide before CMP, after CMP for 60s and 80s using slurry W2000-C. (b) Top view SEM image of the waveguide. (c) Cross sectional SEM image of the waveguide. (d) AFM image of the waveguide	107
Figure 3.19	(a) 2D profile of Ge waveguides separated by 280 µm oxide measured by AFM after CMP for 60s and after an additional 20s over-polishing using W2000-C. (b)	

Ge waveguide height profile measured by AFM after CMP for 90s and after an additional 60s over-polishing using G1000.....	109
Figure 4.1 Solid solubility of P, As and Sb in Ge.....	114
Figure 4.2 Molecular counts of PH _x and GeH ₄ species under different tube temperatures.....	115
Figure 4.3 Arrhenius plot of <i>in situ</i> phosphorus doping concentration in Ge epitaxial films..	118
Figure 4.4 (a) P depth profile of Ge with delta-doped layer by SIMS (b) schematic drawing of Ge films with multiple delta-doped layers on Si substrate	120
Figure 4.5 (a) SEM image (b) AFM image of as grown delta-doped blanket Ge film.....	121
Figure 4.6 Cross sectional SEM image of a Ge waveguide with delta-doped layers	121
Figure 4.7 SIMS depth profiles of Phosphorus in Ge for an as-grown sample and after RTA at 600 °C for 30s, 1min, and 3min.....	124
Figure 4.8 P depth profile of the <i>in situ</i> doped Ge after annealing at 650 °C for 5 min measured by SIMS	125
Figure 4.9 SIMS depth profiles of P in Ge for an as-grown sample and after RTA at 600 °C and 700 °C for 1 min.	129
Figure 4.10 SIMS depth profiles of P from different Ge-on-Si films. P in intrinsic Ge with delta doped layers on top as-grown and annealed at 600 °C for 1 min. P in <i>in situ</i> doped Ge with delta doped layers on top as-grown and annealed at 600 °C for 1 min ..	130
Figure 4.11 Full circles represent the intrinsic diffusivity of phosphorous in Ge from this work. Open squares represent the extrinsic diffusivity of phosphorous in Ge from this work. Intrinsic diffusivities from other groups for temperature ranging from 600 °C to 750 °C are plotted by lines as comparisons	131

Figure 4.12	Plan-view TEM showing uniform threading dislocations in n-type Ge annealed by rapid thermal annealing at 750 °C for 1 min. (TEM courtesy of Tim Milakovich)	134
Figure 4.13	Plan-view TEM showing uniform threading dislocations in a 1 μm wide and 350 nm thick n-type Ge waveguide by annealing at 850 °C for 40 min. (TEM courtesy of Tim Milakovich)	136
Figure 4.14	PVTEM showing the threading dislocations in Ge from thicker buffer to the top of Ge film (TEM courtesy of Tim Milakovich)	138
Figure 4.15	TDD from our Ge films (stars) compared to the TDD from the Ref. [156]	138
Figure 4.16	Cross sectional TEM of the buffered grown Ge waveguide (a) 500 nm wide with 25KX magnification (b) 2 μm wide with 10KX magnification (c) 2 μm wide with 25KX magnification after annealing at 850 °C for 40 min.	142
Figure 5.1	A schematic drawing of the cross section of Ge pnn junction	147
Figure 5.2	Cross section of doping concentration for Ge pnn junction with a symmetric current injection	156
Figure 5.3	Cross section of current injection distribution for Ge pnn junction with a symmetric current injection	156
Figure 5.4	Cross section of current injection distribution for Ge pnn junction with a diagonal current injection (a) metal full-cover (b) metal half-cover (c) metal quarter-cover	157
Figure 5.5	Cross section of current injection distribution for Ge pnn junction with a diagonal current injection with a thin p-Si cladding	158

Figure 5.6	Cross section of current injection distribution for a 500 nm wide Ge pnn junction with a diagonal current injection	159
Figure 5.7	Cross section of current injection distribution for Ge pnn junction with a diagonal current injection and a thicker n-Si cladding (a) metal full-cover (b) metal half-cover (c) metal quarter-cover.....	160
Figure 5.8	Ge DBR laser schematic illustrating various components and the corresponding lengths.....	162
Figure 5.9	Schematic illustration of how a single axial mode is selected in an in-plane DBR laser.....	164
Figure 5.10	Reflectance and transmittance spectrums for a Si/SiO ₂ DBR grating with a 25 nm etch depth.....	164
Figure 5.11	Reflectance spectrum for Si ₃ N ₄ /SiO ₂ DBR grating with a 100 nm etch depth	165
Figure 5.12	Schematics of Ge/Si off-center coupling with both the longitudinal cross section view and top-down view.....	168
Figure 5.13	Transmittance of the fundamental TE mode from Ge to the Si waveguide for various oxide gaps	168
Figure 5.14	Reflectance of fundamental TE mode from Ge to Si waveguide for various oxide gaps	169
Figure 5.15	Transmittance of a fundamental TE mode from Ge to the tapered Si waveguide with a 20 nm oxide gap.....	169
Figure 5.16	Transmittance of the fundamental TE mode from Ge to the Si waveguide with and without height compensation.....	171
Figure 5.17	Process flow for fabricating a Ge DBR laser on SOI with off-center coupling ...	173

Figure 6.1 (a) Cavity structure of a widely tunable Ge laser. (b) Lasing mode selection and tuning by aligning the reflection peaks in both spectra of the sampled gratings (SGRs). 181

List of Tables

Table 2.1	Values for the germanium material parameters used in our calculations	66
Table 2.2	Characteristic temperature T_0 extracted from the calculated threshold current curves for Ge	76
Table 3.1	Partial pressure of contamination chemical molecules for UHVCVD tube in idle mode.....	79
Table 3.2	CMP removal rate for 1 μm Ge waveguides separated by 1 μm oxide, Ge dissolution rate and oxide removal rate with different slurry compositions	100
Table 4.1	Average phosphorous concentration from SIMS measurements and activated carrier concentration from Hall Effect measurements	123
Table 4.2	Active P doping concentration in Ge films under various annealing conditions with the oxide cap and amorphous Si cap.....	126
Table 5.1	Internal optical loss of a pnn junction with 1 μm wide Ge and metals directly above Ge.....	149
Table 5.2	Internal optical loss of a pnn junction with 1 μm wide Ge and metals not directly above Ge	149
Table 5.3	Internal optical loss of a pnn junction with 500 nm wide Ge and metals not directly above Ge	150
Table 5.4	Ge parameters for SRH recombination	153
Table 5.5	Ge parameters for doping dependent mobility.....	154

Chapter 1

Introduction

Integrated circuits (ICs) based on Silicon (Si) technology have been widely used in all the electronic devices, especially computers and mobile phones. Since the invention in 1959, the semiconductor industry has improved the productivity of ICs by 25%~30% annually [1] following Moore's law, predicted by Gordon Moore that the number of transistors per square centimeter on Si based ICs doubles approximately every 18 months [2]. While the transistor density is increasing, the transistor size, typically the gate length shrinks from 10 μm in 1971 to 14 nm in 2014 [3] and the clock frequency boosts from 100 MHz to 5.5 GHz from IBM zEC12 microprocessor in 2012 [4].

However, the classical scaling starts to slow down. For example, the physical gate length scales $\sim 0.9\times$ from 90nm node in 2004 to 32nm node in 2010 [5] compared to the predicted scaling factor of $0.7\times$ [2]. The main reason is the off-state leakage current [6]. In current high-

performance logic technologies, the leakage power of complementary metal oxide semiconductor (CMOS) transistors is approximately 20-30 W (out of a total power budget of 100W). The leakage current will increase packaging cost because of cooling and energy consumption [7].

Additionally, the clock frequency has not increased exponentially since 2005 and even decreased [8]. The main reason is that the metal wires connecting the transistors now become the dominant factor regarding delay and power dissipation. The delay of a wire is directly proportional to the product of resistance of the metal and capacitance between the metal wires, also called as “RC delay”. While following the scaling rule, wire resistance goes up because wires are made smaller and the capacitance between wires also increases because the pitches of metal wires are smaller. And therefore RC delay increases. The dynamic power dissipation follows a simple rule which is CV^2f and therefore, the power density will increase linearly while the speed goes up and the corresponding heat dissipation issues come up. Multi-core architectures shifting towards parallelism is a current solution to keep on improving the performance of a CPU [9].

A lot of research is ongoing to increase the transistor speed while controlling the off-state leakage current. Multi-gate or tri-gate transistors (also known as FinFET technology [10]), which is a complete different architecture than planar MOSFET, enables the VLSI industry to continue the pace of Moore's Law for 14 nm, 10 nm and smaller feature-size technologies [11]. In 2014, TSMC reported that the 16 nm FinFET process is ready to be delivered with a 40% performance increase at the same power consumption compared to the 20 nm planar (20SoC) process node and 10 nm, 7 nm FinFET processes are planned to be delivered in 2016 and mid-2017, respectively [12]. Another different approach to increase the transistor speed is to use high

mobility channel materials like Ge [13] or III-V [14]. Combined with the FinFET, strain engineering, high-k/metal gate and SiGe/Ge/III-V materials, it is projected that with the scaling can be continued to 2.5 nm [15].

Therefore, the current speed and power bottle neck so far is not from the intrinsic transistor speed, but rather from the metal wires connecting these transistors as discussed before, dominated by RC delay and CV^2f power consumption. To continue increasing the speed and bandwidth while lowering the power consumption and utilizing Si based high volume manufacturing, a new disruptive technology is required and Silicon Photonics using optical interconnects is one of the potential solutions.

1.1 Silicon Photonics

Silicon photonics is a technology that photonic devices are produced and integrated within standard silicon factory and with standard silicon processing. Photonics devices are based on Si or materials compatible with Si. The devices generate, modulate, guide and detector light or photons in order to transfer data at high speed and bandwidth with predicted low power consumption rather than using electrical signals over aluminum or copper wires. Silicon photonics is fully compatible with CMOS process flows and therefore, high volume manufacturing is intrinsically possible using current foundries and also the production cost can be easily scaled down to very low [16].

1.1.1 Bandwidth, Power and Market

Since the invention of optical fibers, optical interconnects have been widely used for the long haul telecommunication, enabling the fast development of the global information exchange such as the internet with the advantages of high speed or bandwidth and low loss over a long distance. As predicted in Figure 1.1, optical interconnect, using optical fibers will be the main technology for middle to long haul (1-10km) information transmission with a high bandwidth over 1Tbit/s. Regarding electrical interconnects, due to the signal delay and power consumption at high speed, it will be still limited to the speed less than 10G. However, Moore's law is still required to continue to enable more and more data processing and transmission. This is where Silicon photonics can be utilized to fill the gap of the requirements of both high bandwidth and short data transmission. Silicon photonics uses light to transmit information which is inherently high speed or bandwidth because of no RC delay as the electrical interconnect. Additionally, the data rate can scale with channels or wavelengths since the light with different wavelengths do not interfere with each other while transmitted through the same medium. For example, if one channel has a bandwidth of 10 Gbit/s, 10 channels can have a total bandwidth of 100 Gbit/s. This is usually called wavelength-division multiplexing (WDM). Additionally, since Silicon photonics is based on CMOS technology, the integration of each optical component onto the same chip is also inherently possible.

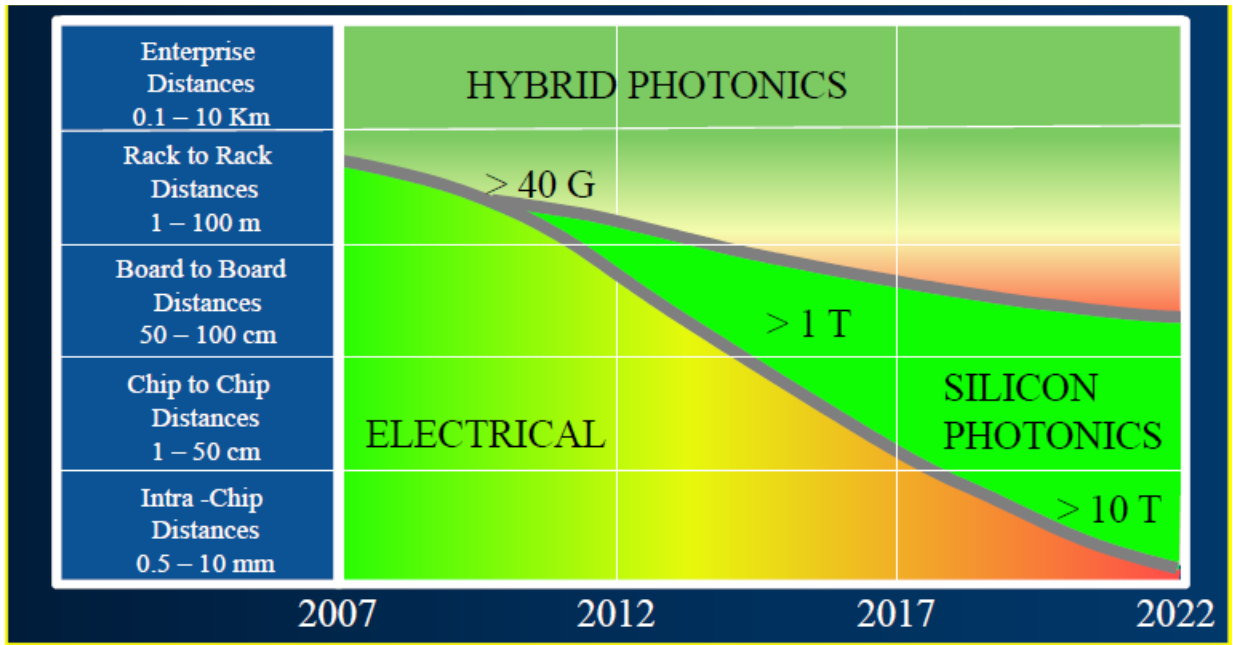


Figure 1.1 Silicon photonics application trend to fill the gap between electrical interconnect and fiber optical interconnect with the requirements of shorter distance and higher bandwidth [17].

Another appealing advantage is the power saving using Silicon photonics. Ideally the transmission of light does not cost any power if no propagation loss is considered. In fact, there is power consumption to electrically generate light, to modulate light and also current leakage while detecting light. Overall, the energy cost per bit can be in the order of several pJ/bit or even lower depending on the different photonic components and systems [18]. Figure 1.2 shows a comprehensive power consumption study in an optical transceiver including electrical backend circuitry. In a 256 Gbit/s network, the power cost is less than 5 pJ/bit, which implies a total power consumption of 1.28 W [18]. Among the usage of power, thermal tuning and laser (always on) consume the most amount of power. Therefore, for a further power saving at the high data rate, laser power gating will be very helpful and this indicates the necessity and value to integrate the light source on chip.

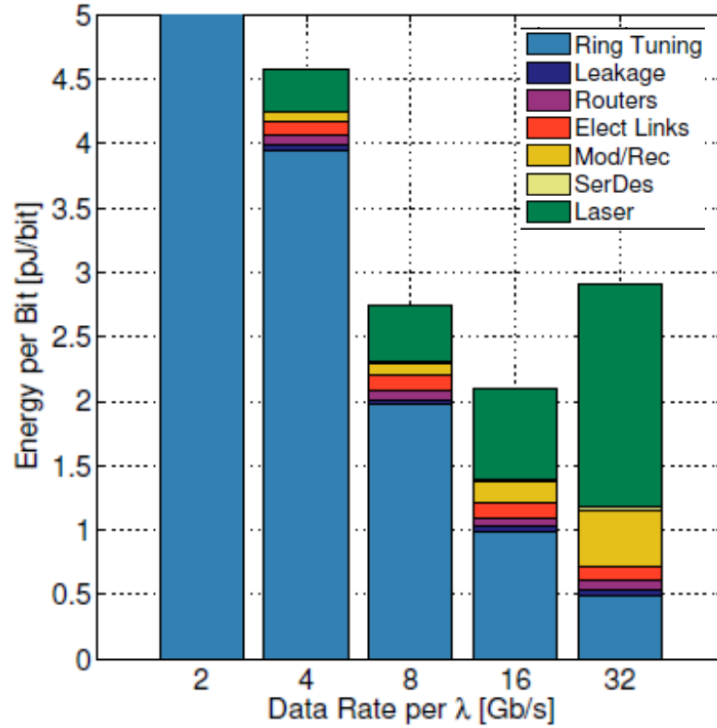


Figure 1.2 Network energy cost per bit calculation from DSENT model including optical devices and electrical backend circuitry such as modulator driver, receiver and ring tuning circuits. The throughput of each link is 128 bits/core-cycle at a 2 GHz core clock, a data-rate of 2, 4, 8, 16, 32 Gb/s per wavelength implies 128, 64, 32, 16, 8 wavelengths per link, respectively [18].

Data centers are one of the big drivers for Silicon photonics because data centers are demanding high bandwidth and low power consumption due to the rapidly increasing traffic over the Internet. On Jan 16, 2013, Intel Corporation announced a collaboration with Facebook to use their 100G Silicon photonics rack-to-rack technology to power the world's largest data centers [19]. Except for data centers, silicon photonics also has large application potential in telecom, sensors and imaging. The market size is expected to increase from \$65M in 2011 to \$215M in 2017 [20].

1.1.2 Optical Components in Photonic Network

Silicon photonics is composed by multiple passive and active optical components including their electronic circuitry to realize electric to optic signal (EO) transition and then optic signal transmission and finally optic to electric signal (OE) transition. In a simplified optical link, light is generated by electrically pumped lasers with the wavelengths normally around 1300 nm or 1550 nm. The output light is guided in waveguides which have a high refractive index in the core region to confine the light. Modulators are used to encode the light with the electric signal by intensity or phase or polarization modulation. Encoded light at certain wavelength is then passed through filters, which usually are ring resonators, to the main waveguide bus. The optic signal travels along the bus and then is dropped by another filter which can pick up the light wavelength. Photodetectors (PDs) are then used to convert the optic signal back to electric signal for further processing.

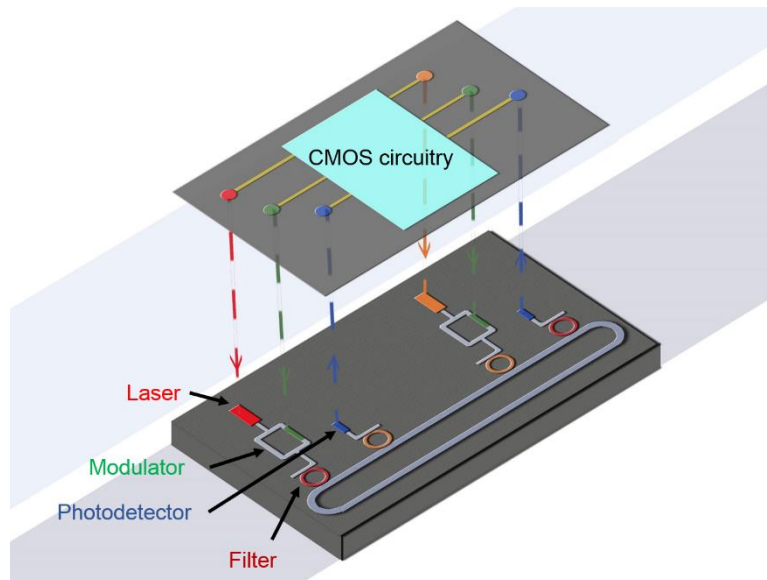


Figure 1.3 Schematic of an on-chip optical interconnect with optical components of laser, modulator, photodetector and other passive resonators and waveguides. The photonic layer is hybrid integrated with the electronic layer.

Figure 1.3 shows a schematic of an on-chip optical interconnect 3-D integrated with the electronic circuitry. In other chip-to-chip or rack-to-rack communications, the modulated optic signals from multiple channels are normally multiplexed to a single mode waveguide. And then light is coupled from the waveguide to certain kind of optical interconnect such as polymer waveguide or optical fiber between chips or racks. After that, light is coupled back to a single mode waveguide on another chip, demultiplexed to different wavelengths and detected by the PDs.

There has been a lot of extraordinary research on each single optical component and their integration. The fundamental requirement to each component is the compatibility with Si CMOS. Silicon is the most ideal material for passive devices such as waveguides, filters, resonators and gratings due to its transparency in the telecommunication wavelength range and high refractive index which provides small footprints. Single mode silicon waveguides are usually fabricated by the SOI wafer with 220 nm thick Si with the width of 450 nm~500 nm and 2~3 μm thick oxide underneath. Researchers have successfully demonstrated low loss single mode Si waveguides, which have the loss less than 1 dB/cm at the telecommunication wavelengths [21, 22]. Other lower index waveguides such as Si_3N_4 are also attractive owing to the ultra-low loss of 1.2 dB/m [23], efficient coupling with optical fibers, reduced sensitivity to perturbations and the application in ultra-high-Q resonators [24].

Since Si is transparent in the 1.3~1.6 μm range, it cannot be used for light detection. Instead, Germanium (Ge) has a direct band gap of 0.8 eV and thus a high direct band gap absorption below 1.55 μm . With tensile strain band engineering, the band gap of Ge can be further reduced so that it can be suitable to detect light of longer wavelengths, covering both L band (1.56–1.62 μm) and C band (1.53–1.56 μm) [25]. Ge is also fully compatible with the Si

CMOS process. Ge can be grown on Si epitaxially while overcoming a 4.2% lattice mismatch. The typical growth method is a two-step growth using chemical vapor deposition (CVD) [26, 27]. With a further high temperature cyclic annealing, threading dislocations which are the major source of dark current [28], can be reduce to the order of 10^7 cm^{-2} for the blanket 1 μm thick Ge film and 10^6 cm^{-2} for 10 μm \times 10 μm Ge mesa [26]. High performance Ge p-i-n [29-32] or avalanche [33-35] PDs have already been developed by many research groups and research centers. The typical features from Ge p-i-n PDs can have a dark current of $\sim 20 \text{ nA}$ and responsivity of $\sim 1 \text{ A/W}$ with the bandwidth of over 40 GHz [36].

The most common modulators are Si modulators using plasma dispersion effect, in which the concentration of free charges in silicon changes the real and imaginary parts of the refractive index [37]. There are two kinds of device structures to achieve intensity modulation using above effects. One is Mach–Zehnder interferometer (MZI) and the mechanism is that the refractive index change is used to shift the relative phase of two propagating waves in two parallel waveguides such that they interfere either constructively or destructively. Some of the example devices have been presented in Ref. [38, 39]. The other is a resonant structure such as a ring resonator and the mechanism is that the refractive-index change can change the resonant condition, thus allowing the device to be switched between on- and off-resonance states at any given wavelength. Some of the example devices have been presented in Ref. [40-42]. Another method to achieve light modulation is using Franz–Keldysh effect in Ge and the quantum-confined Stark effect (QCSE) in Ge quantum wells, which are both electric-field-induced changes in optical absorption. Some of the example devices have been presented in Ref. [43, 44]. Other progresses on strained Si research report a realization of Pockels effect based Si electro-optic modulators [45, 46].

A light source is another key component in the optical interconnect and it is also the most challenging device to realize. Since Si is an indirect band gap material, it is not an efficient light emitter. Many different approaches have been proposed to provide a light source based on Si, such as optically pumped Si Raman laser using stimulated Raman scattering in Si waveguides [47], optical gain and stimulated emission found in periodically nano-patterned crystalline Si [48], optical gain and efficient LED demonstrated in Si nanocrystals in dielectric (SiO₂) matrix [49], optically pumped erbium-doped waveguide lasers [50] and so on. The challenges of most of these devices are the lack of efficient electrical injection. III-V materials have been demonstrated to be an efficient and reliable laser for a long time. However, the integration of III-V lasers with Si has also been a problem for a long time. One way to integrate III-V with Si is by growing III-V epitaxially on Si with the Si_xGe_{1-x} buffer [51]. However, the laser degrades in 15 min due to resistive heating issue. Another common way is a hybrid integration to bond the III-V layer on Si and these quantum well lasers have already been demonstrated to have a high performance by many groups [52-56]. Some potential problems for the hybrid lasers are the cost effectiveness of scaling, the performance degradation with temperature and the production yield. Tensile strained Ge on Si is our approach to solve the light source problem for Si photonics with the advantages of high density scaling, low cost due to the monolithic integration and better temperature stability. The details about Ge lasing physics, material and key device processing steps will be discussed in details in the following chapters.

1.2 Ge Light Emitters for Silicon Photonics

1.2.1 Ge Band Structure Engineering

Traditionally, indirect band gap material is treated as an inefficient light emitter because the probability of direct electron-hole recombination is less with a phonon to conserve the momentum. However, bulk Ge has the conduction band energy at the Γ valley which is 136 meV higher than the energy at the L valleys at room temperature as shown in Figure 1.4(a). The properties of Ge are rather close to those of III-V compounds with the direct band gap. As proposed by Liu [57] that with an additional tensile strain applied to Ge, the Γ valley in Ge can shrink faster than the L valleys due to the smaller effective mass in the Γ valley and with $\sim 1.8\%$ tensile strain Ge becomes a direct band gap material. Therefore, we can achieve optical gain in Ge, as shown in Figure 1.4(b). It is obvious that the smaller energy difference is between the Γ and L valleys, the higher is the internal quantum efficiency. The internal quantum efficiency is defined by the ratio of the number of emitted photons from direct band transition to the numbers of injected electrons. However, the band gap shrinks to ~ 0.53 eV with 1.8% strain, corresponding to a wavelength of 2500 nm. To achieve efficient light emission while still keeping the emission wavelength around 1550 nm, Liu [57] then proposes to use n-type doping to raise the Fermi level and thus raise the effective bottom of the indirect L valleys to the Γ valley or even higher, as shown in Figure 1.4(c). Therefore, fewer carriers are required to be injected in order to reach transparency and also gain in Ge. The simulation shows that n-type doping has to be $7.6 \times 10^{19} \text{ cm}^{-3}$ with 0.25% tensile strain to fill the Fermi level to the Γ valley. Additionally, there is a positive net materials gain in Ge when it is doped to higher than around $1 \times 10^{19} \text{ cm}^{-3}$ taking the free carrier absorption from n-type doping into consideration.

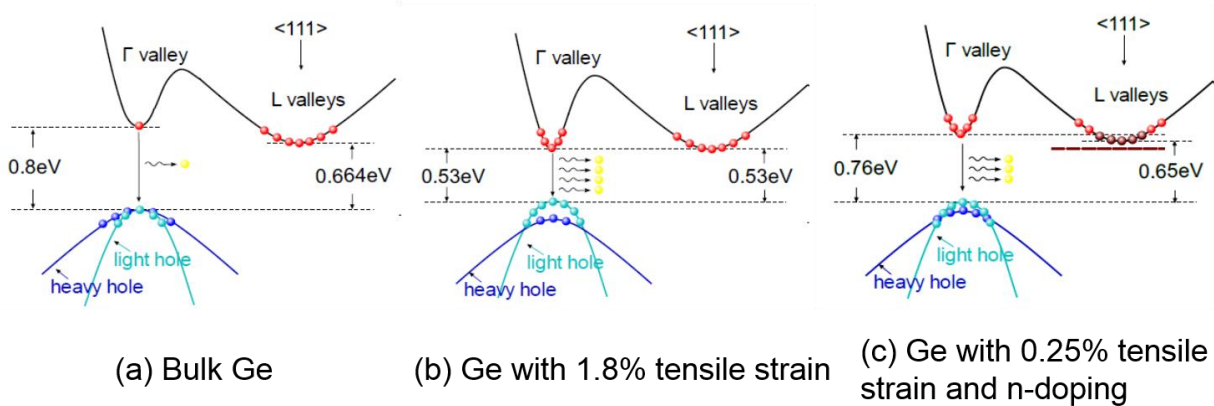


Figure 1.4 Ge band structures under injection. (a) bulk Ge (b) Ge with 1.8% tensile strain (c) Ge with 0.25% tensile strain and n-type doping concentration of $7.6 \times 10^{19} \text{ cm}^{-3}$ [57].

This theoretical prediction in 2007 stimulated a lot of interests in Ge on Si research including deeper physical understanding of band structure and carrier dynamics, epitaxial Ge growth and doping, Ge strain engineering and Ge light emitting device studies. Specifically, the room temperature optically pumped Ge-on-Si laser was demonstrated in 2010 [58] and the electrically pumped Ge-on-Si laser was demonstrated in 2012 [59]. The Ge laser demonstrations further highlight the potential of using Ge as a light source for Si photonics.

1.2.2 Literature Review on Ge-on-Si Material and Devices

1.2.2.1 Tensile Strain Study

There are two main research efforts and directions to make Ge as an efficient light emitter. One is to apply as high tensile strain as possible to reduce the need for n-type doping which contributes to free carrier loss and low minority carrier lifetime.

In order to apply the larger tensile strain, Ge can be epitaxially grown on the substrate with larger lattice constant, such as GeSn [60] or $\text{In}_{1-x}\text{Ga}_x\text{As}$ [61, 62] buffer layer. The Ge epitaxial grown on GeSn offers the possibility to get tensile strained Ge quantum well structure, which could be a big improvement for lowering the laser threshold. With a step-graded $\text{In}_{1-x}\text{Ga}_x\text{As}$ buffer, Ge can have very high tensile strain of 2.33% within a few nm [62] and a moderate strain of 0.75% with a thickness of 150 nm [63]. Although strong photoluminescence enhancement is observed with higher strain, this growth method is inherently not CMOS compatible for the real application.

Tensile strain and enhanced direct band gap emission have also been demonstrated on bulk Ge [64] and nano-membranes [65] using external stressor or micromechanical strain engineering. However, the strain applied by these methods is localized and non-uniform and hinders further device fabrication. Another noticeable and promising method is to use silicon nitride as a stressor layer because of its CMOS compatibility [66, 67]. An initially compressively strained silicon nitride layer deposited by plasma-enhanced chemical vapor deposition can relax and efficiently transfer its stress to Ge, as it is free to move laterally, which makes Ge tensile strained. The strain transferred to Ge depends on the Ge waveguide structure. So far, a uniaxial strain up to 1% has been observed on the room temperature direct band gap photoluminescence (PL) of germanium waveguides with a PL peak around 1650 nm [67]. Another group has even demonstrated a direct band gap emission with wavelength above 1.9 μm [68], indicating a higher tensile strain. Although the emission shifts to a longer wavelength which is not suitable for telecommunication, these studies expand the application of Ge as a light emitter or photodetector into the mid-IR region.

1.2.2.2 N-type Doping Study

Besides of tensile strain study, there is a large number of research focusing on the incorporation of high n-type doping into Ge while keeping a reasonable tensile strain to achieve emission around 1550 nm.

Generally, ion implantation is the most common way to introduce n-type dopant into semiconductors such as Si or Ge. This technique implants high energy ions accelerated by an electrical field into solids. Through annealing, the implanted ions can be mostly electrically activated. The advantages of ion implantation are very obvious that the process is well known in the Si CMOS industry and the amount of ions and position of ions implanted into solids can be precisely targeted and controlled. A challenge is that the dopant such as phosphorus tends to form phosphorus-vacancy (P-V) complexes which are electrical inactive and relatively immobile during annealing [69]. The vacancies are generated by the ion implantation process. Another issue is dopant loss during thermal annealing which is mediated by ion implantation damage, giving rise to lower active doping concentration [70]. Therefore, it seems that there is an activation limit of $5\sim 6\times 10^{19} \text{ cm}^{-3}$ for P obtained in the conventional rapid thermal annealing method [71]. In order to get a higher activation ratio after annealing, co-implantation with non-doping impurities can be utilized to trap the vacancy and suppress P-V complex formation. This technique is called point-defect engineering. For example, fluorine (F) is co-implanted with P into the epitaxial Ge film and after annealing, the overall activated fraction of P is enhanced compared to the P implanted-only sample and the activated carrier concentration can be as high as $1\times 10^{20} \text{ cm}^{-3}$ [72]. The reason is that F passivates the vacancies. Other work on antimony (Sb) and P co-implantation has also shown an activated n-type doping concentration of $1.3\times 10^{20} \text{ cm}^{-3}$ [73]. Different capping layers have been studied to evaluate their capability to prevent dopant

loss through out-diffusion during annealing, including silicon oxide, silicon nitride and amorphous Si. Silicon nitride is found to be the best capping layer with the least out-diffusion and highest activation fraction [74]. However, the implantation damages, such as clustering of vacancies and amorphous material, created by the heavy ion collision are difficult to completely remove during thermal annealing [75]. These defects can be additional non-radiative recombination centers for carriers. Our previous work on the photoluminescence studies on implanted Ge samples showed a five times lower emission from the implanted Ge compared to the *in situ* doped Ge [76]. Motivated by our work, photoluminescence studies have been carried out on the implanted Ge samples extensively. The strongest PL intensity is observed from the sample with lowest sheet resistance and this phenomenon matches with the theoretical prediction that n-type doping can fill the L valleys and thus enhance the direct band gap transition. However, the higher implantation dose doesn't always give a higher PL intensity because the implantation damage trades-off with the n-type doping [74]. Therefore, our studies together with other research on the Ge implantation imply that ion implantation might not be a good way for high n-type doping in Ge since the implantation damage cannot be removed completely.

To avoid implantation damage, *in situ* doping methods are studied with different growth techniques. Using the molecular beam epitaxy (MBE) technique, researchers can achieve an electrical active Sb incorporation ranging from $5 \times 10^{17} \text{ cm}^{-3}$ to $2 \times 10^{20} \text{ cm}^{-3}$ in Ge at a substrate temperature of 160 °C, and the highest doping level is well above the maximum equilibrium solid solubility of $1.2 \times 10^{19} \text{ cm}^{-3}$ [77, 78]. The electroluminescence increases with doping concentration from $5 \times 10^{17} \text{ cm}^{-3}$ to $4 \times 10^{19} \text{ cm}^{-3}$ and then drops with even higher doping [78]. This behavior is contradictory to theoretical predictions that the PL is enhanced with higher doping, indicating a possible worse Ge quality with higher doping. If using a gas phase

phosphorus source in a chemical vapor deposition (CVD) tool, a maximum active doping concentration of $1 \times 10^{19} \text{ cm}^{-3}$ is achieved both by reduced pressure chemical vapor deposition (RPCVD) and ultra-high vacuum chemical vapor deposition (UHVCVD) [76, 79]. The doping concentration is limited by P desorption at high growth temperatures and limited by activation at low growth temperatures. Further development with an *in situ* method to achieve mid- 10^{19} cm^{-3} will be discussed in the following chapters. The key innovation is to dope Ge heavily without extra damage introduction or crystal quality degradation.

Electrically pumped Ge light emitting diodes (LEDs) have been fabricated and tested from several groups around the world. A Stanford university group fabricated a surface emitting Ge n⁺/p LED with Ge doped to $7.5 \times 10^{18} \text{ cm}^{-3}$ and electroluminescence (EL) was observed at $1.6 \mu\text{m}$ [80]. The device showed both an enhanced emission with higher n-type doping and with higher temperature. They also showed another Ge PN junction with Ge membranes and external stressor technique was employed to introduce a 0.76% bi-axial tensile strain. EL emission was one order of magnitude higher than the bulk Ge device [81]. A Stuttgart university group used MBE Ge epitaxy growth and fabricated a Si/Ge/Si heterojunction p⁺nn⁺ LED with Ge doped to $5 \times 10^{17} \sim 1 \times 10^{20} \text{ cm}^{-3}$ [78]. Direct band gap EL was observed and band gap narrowing with higher doping as well. A Glasgow university group reported a Ge LED structure on Si with an average power of $\sim 10 \mu\text{W}$ at the wavelength of $1.7 \mu\text{m}$, which opened the route for integrated light sources and PDs above $1.6 \mu\text{m}$ on Si with applications for lab-on-a-chip and healthcare [82]. Our group also reported EL emission from the Ge p-i-n structure [83] and the Ge p-n-n structure [84]. The EL intensity has a superlinear relationship with injection. Challenges are still existing to make the Ge device from a LED to a laser. First is that optical gain has to be high enough to

overcome the free carrier loss from the active Ge and also claddings. Second is that the lasing threshold current has to be as low as possible to make an energy efficient and long lifetime laser device. Third is to make a resonant cavity with a reasonable reflectivity considering the trade-off between the output power and lasing threshold current.

1.2.3 General Laser Physics and Theory

Semiconductor diode lasers generally incorporate an optical gain medium in a resonant optical cavity. The gain medium consists of a material which can absorb incident radiation below a certain energy and then amplify the incident radiation by stimulated emission along with the generation of additional radiation. Besides of the optical pumping, the uniqueness of diode lasers is that they can be directly pumped by an electrical current. If the resulting gain is sufficient to overcome the losses of certain resonant mode in the cavity, the mode reaches the threshold to lase, and a coherent light will be emitted. The resonant cavity provides a positive feedback for radiation being amplified while the laser light is emitted through one end of the cavity. Therefore, a lasing oscillation is established and sustained above threshold current with a stable output power.

1.2.3.1 Radiative Transition and Optical Gain

For carriers injected into conduction bands and valence bands, there are three types of radiative transitions which are important in the semiconductor lasers. They are stimulated absorption with the transition rate R_{12} , stimulated emission with the transition rate R_{21} and spontaneous emission

with the transition rate R_{sp} . Because R_{12} absorbs photons and R_{21} generates photons, the net generation rate of photons is:

$$R_{st} = R_{21} - R_{12} = R_r(f_c - f_v) \quad (1.1)$$

where R_r is radiation transition rate and f_c is the occupation probability of electrons in the conduction band and f_v is the occupation probability of holes in the valence band.

$$f_c = \frac{1}{e^{(E_2 - E_{Fc})/kT} + 1} \quad (1.2)$$

$$f_v = \frac{1}{e^{(E_1 - E_{Fv})/kT} + 1} \quad (1.3)$$

E_{Fc} and E_{Fv} are the conduction band and valence band quasi Fermi levels, respectively.

To have the stimulated emission rate larger than the absorption rate, Equation (1.1), (1.2) and (1.3) reveals that

$$E_{Fc} - E_{Fv} > E_{21} \quad (1.4)$$

where $E_{21} = E_2 - E_1$ is the photon energy.

Optical gain is defined by the proportional growth of the photon density per unit length as it propagates along the optical cavity. The unit usually is cm^{-1} or dB/cm . Therefore, the optical gain can be expressed as follows:

$$g = \frac{1}{N_p} \frac{dN_p}{dz} = \frac{1}{v_g N_p} \frac{dN_p}{dt} = \frac{1}{v_g N_p} (R_{21} - R_{12}) \quad (1.5)$$

With the Fermi's Golden rule, we can then derive an explicit equation for optical gain:

$$g(E_{21}) = \frac{\pi q^2 \hbar}{n \epsilon_0 c m_0^2 \hbar v_{21}} |M_T(E_{21})|^2 \rho_r(E_{21}) (f_c - f_v) \quad (1.6)$$

where $|M_T(E_{21})|^2$ is related to transition matrix element and n is the refractive index of the material. ρ_r is the joint density of states of the conduction band (Γ valley) and the valence bands (heavy hole and light hole). The Equation 1.6 is used to calculate the Ge optical gain in Chapter

2.

1.2.3.2 Threshold Current and Output Power

Optical gain is a function of carrier density and it can be approximated as a linear relationship near the carrier injection transparency. Therefore, it can be represented by the following equation:

$$g \approx a(N - N_{tr}) \quad (1.7)$$

where N_{tr} is the transparency carrier density and a is the differential gain near the transparency, $\left(\frac{\partial g}{\partial N}\right)_{N_{tr}}$.

To reach the lasing threshold, the optical gain has to overcome losses in the device, such as mirror loss α_m and absorption loss α_i including free carrier losses from gain medium as well as cladding layers. The detailed calculation for the mirror loss and the absorption loss for Ge devices will be discussed in detail later.

The threshold gain has the following equation:

$$\Gamma g_{th} = \alpha_i + \alpha_m \quad (1.8)$$

where Γ is the optical mode confinement factor in the gain medium. Derived from Equation 1.7 and Equation 1.8, we can get that:

$$\Gamma a(N_{th} - N_{tr}) = \alpha_i + \alpha_m \quad (1.9)$$

where the parameters a and N_{tr} are from the gain relationship with carrier injection density in Equation 1.7.

When carriers are injected into the gain material by electrical current, not all the electrons and holes will recombine in the active region in practical. The internal quantum efficiency η_i is defined by the fraction of injected current that generates carriers in the active region. The current leakage by possible shunt paths around the active region is one of the sources contributing to reduced η_i .

In the active diode region, the injected current provides a generation term and various radiative and non-radiative recombination processes provide recombination terms. Therefore, the rate equation is:

$$\frac{dN}{dt} = G_{gen} - R_{rec} \quad (1.10)$$

where $G_{gen} = \frac{\eta_i I}{qV}$ and recombination includes spontaneous recombination R_{sp} , non-radiative recombination R_{nr} and stimulated recombination R_{st} . It is natural to describe a decay process by a carrier lifetime, τ . Thus, in the absence of photons or a generation term, $\frac{N}{\tau} = R_{sp} + R_{nr}$. We will discuss the non-radiative recombination in Ge in details in the following chapters.

At the lasing threshold, the rate Equation 1.10 is in a steady-state, and therefore we have the generation rate equals the recombination rate:

$$\frac{\eta_i I_{th}}{qV} = \frac{N_{th}}{\tau} \quad (1.11)$$

When we insert Equation 1.9 into Equation 1.11, the threshold current can be expressed by the following equation:

$$I_{th} = \frac{qV}{\eta_i \tau} \left(N_{tr} + \frac{\alpha_i + \alpha_m}{\Gamma_a} \right) \quad (1.12)$$

The optical output power from the mirrors is [85]:

$$P_{out} = \eta_d \frac{hv}{q} (I - I_{th}) \quad (1.13)$$

where η_d is defined as differential quantum efficiency and has the following expression:

$$\eta_d = \frac{\eta_i \alpha_m}{\alpha_m + \alpha_i} \quad (1.14)$$

Equation 1.12 and Equation 1.13 are also used for the threshold current and output power simulation for the Ge-on-Si laser in Chapter 2.

1.3 Thesis Goal and Outline

The goal of thesis is to understand the properties of Ge under heavy doping and high temperature, to develop proper processing steps for Ge growth and light emitting device and to design a Ge laser with a low threshold current and single mode emission.

In Chapter 2, we focus on the theoretical understanding of Ge gain material and laser performance. We will investigate the effects of heavy n-type doping on Ge electronic band structure, materials net gain and threshold current. We will study the Ge material and device performance under high temperature to explore the possibility to make a Ge laser with the good temperature stability.

In Chapter 3, we focus on the single crystalline Ge growth on Si in oxide trenches using UHVCVD. We will present the process developments on the vertical oxide sidewall, the Ge trench and corner filling and the trench size dependent Ge non-buffer growth. In the second part of Chapter 3, we describe the Ge CMP process in detail.

In Chapter 4, we focus on the n-type doping related processes and understandings in Ge. We will describe the process we developed to incorporate n-type doping in Ge to as high as mid- 10^{19} cm^{-3} using the delta doping source and annealing without introducing extra defects. We will show our comprehensive dopant diffusion simulation to predict the annealing temperature and time to achieve high n-type doping and uniform distribution. We also use plan-view transmission electron microscopy to examine the threading dislocation density (TDD) in n-Ge for both blanket films and trench grown waveguides. The result may explain the high threshold current in our first generation of the electrically pumped Ge laser.

In Chapter 5, we will present our design of an external cavity Ge laser using distributed Bragg reflector (DBR) gratings on Si waveguides. The discussion includes (1) the cross section

design to mitigate the internal optical loss and to improve the current injection uniformity across the Ge waveguide; (2) The DBR grating design to achieve single mode operation and different mirror reflectivity; (3) the coupling design between Ge and Si waveguides to increase the coupling efficiency.

In Chapter 6, we summarize the achievements in this thesis and discuss some possible future work to improve the Ge laser performance and to have more functionality such as tunability.

The appendixes contain examples of my simulation codes for Ge diffusion by MATLAB and electrical simulation of Ge pnn devices by Sentaurus.

Chapter 2

Theoretical Prediction of Optical Behavior of Bulk Ge Laser

This chapter is intended to study the optical properties of Ge material and laser devices in theory. We first discuss the effects of heavy n-type doping on the free carrier absorption (FCA) and the electronic band structure of Ge. We then incorporate both effects demonstrated experimentally from our band-engineered Ge into a gain calculation model to predict a revised Ge net material gain spectrum at room temperature. Our revised modeling shows that the optical gain is actually higher than the original prediction in Ref [57], consistent with the data from the electrically pumped Ge-on-Si laser in Ref [59]. After that we study the Ge optical performance with

temperature and show that non-radiative recombination is a dominant factor for degradation of Ge optical properties at high temperature. Finally, we predict the threshold current density for a bulk Ge laser with the doping dependence and temperature dependence.

2.1 Effects of Heavy n-type Doping

As discussed in Chapter 1, n-type doping in Ge can raise the Fermi level closer to the bottom of the Γ valley in the conduction band and thus enhance the direct band gap transition. However, impurity doping in semiconductor can also contribute to free carrier absorption as a loss term which can reduce the net material gain, leading to a higher threshold current. The small difference between the Γ and L valleys in the Ge band structure allows the achievement of a pseudo-direct band gap with an n-type doping of $7.6 \times 10^{19} \text{ cm}^{-3}$ and 0.25% tensile strain. However, this kind of doping level is high in Ge so that it is very important to study the n-type doping effects on the electronic and optical properties of Ge.

2.1.1 Free Carrier Absorption in Ge

When Ge is n-type doped with 0.25% tensile strain, the electron population in the indirect L valleys is about 4 orders of magnitude higher than in the direct Γ valley because the L valleys are 110 meV lower than the Γ valley and also because the effective electron mass is $0.22m_0$ in the L valleys and $0.038m_0$ in the Γ valley. Free carriers in the L valleys can occupy empty states with higher energy inside the L bands and the phenomenon is called “free carrier absorption” or intra-valley scattering. Free carriers in the L valleys can also be scattered to the Γ valley with phonon

assistance and then contribute to the direct band gap transition. This is called inter-valley scattering. The Drude model is commonly used to explain the free carrier loss in Si, stating the FCA is proportional to doping. We also use the Drude model to extrapolate the FCA at shorter wavelengths near the direct band gap from absorption data measured in the far infrared regime [57]. However, it is known that the Drude model does not apply to wavelengths near the band gap for III-V semiconductors. A first-principle model [86] has been employed to describe the FCA in GaAs in the near infrared regime, which takes into account the band structure as well as optical phonon, acoustic phonon, and charged impurity scattering mechanisms. Our studies on the infrared absorption of tensile strained n^+ Ge also show that the classic λ^2 -dependent Drude model of intra-valley free electron absorption only holds true at $\lambda \geq 15 \mu\text{m}$ [87]. It is a collaborative work with Prof. Jifeng Liu in Dartmouth College. At $\lambda < 15 \mu\text{m}$ the free electron absorption decreases much faster with wavelength than the prediction of the Drude model. This observation motivates us to apply the first principle model described in Ref [86] to intra-valley free electron absorption near the band gap of the tensile strained n-type Ge. Indeed, the first principle model agrees with the measured absorption spectra of tensile-strained n^+ Ge very well. It also explains the deviation from the classic Drude model at $\lambda < 15 \mu\text{m}$: band structure, impurity scattering, and photon scattering all have to be taken into account at shorter wavelengths. Therefore, we are confident to use the first principle model to calculate the free electron absorption in n^+ Ge in the wavelength range of 1500~1700 nm, which is difficult to measure directly due to the overlap of FCA with direct gap absorption. Figure 2.1 shows the calculated free electron carrier absorption coefficient at $\lambda=1550 \text{ nm}$ using the first principle model. The free electron absorption coefficient is 6~8 times lower than the values used in the Drude model at injection levels from 10^{19} cm^{-3} to mid- 10^{20} cm^{-3} [57]. With the correction of the free electron

absorption in the material gain calculation, a higher net gain is expected.

2.1.2 Band Gap Narrowing Effect due to Heavy Doping

Band gap narrowing (BGN) is a well-known effect in heavily n-type or p-type doped semiconductors, such as Si, Ge, GaAs and so on. However, there are only a few experimental research studying the BGN in heavily n-type doped Ge. Haas [88] observed both direct band and indirect band gap narrowing by experimentally measuring the infrared absorption in heavily n-type Ge and stated that the direct and the indirect energy gap showed approximately the same change with doping. One drawback of the optical absorption measurement is that the band-to-band absorption spectrum overlaps strongly with the free-carrier absorption for photon energies close to the band-gap energy [89]. Recently, the direct band BGN was also observed in n-type doped Ge LEDs with ~ 38 meV band gap shrinkage at $1 \times 10^{20} \text{ cm}^{-3}$ doping [78]. From the PL measurements of n-Ge at room temperature (300 K), we also observed that the direct band gap related PL peaks red-shifted with higher doping concentration, as shown in Figure 2.2. Details can be found in the reference from Camacho et al [90]. The PL spectrums are measured by a Horiba LabRam system with a 1064 nm laser of a power density of $\sim 10^6 \text{ mW/cm}^2$, and an EOS InGaAs IGA1.9 photodetector. The emission is from the band-edge of direct gap near the Γ valley, and hence, the PL peak emission is directly related to the energy gap, E_{Γ} . Since the Fermi level is still below the Γ valley, Boltzmann distribution is used to interpret the PL spectrums. The energy of the peak emission is $kT/2$ higher than the direct band gap. The band gap without BGN is calculated by adding $kT/2$ to the energy difference between the valence

band and the Γ valley. The difference between the peak emission and the base band provides the BGN in the Γ valley, which is the values plotted in Figure 2.2.

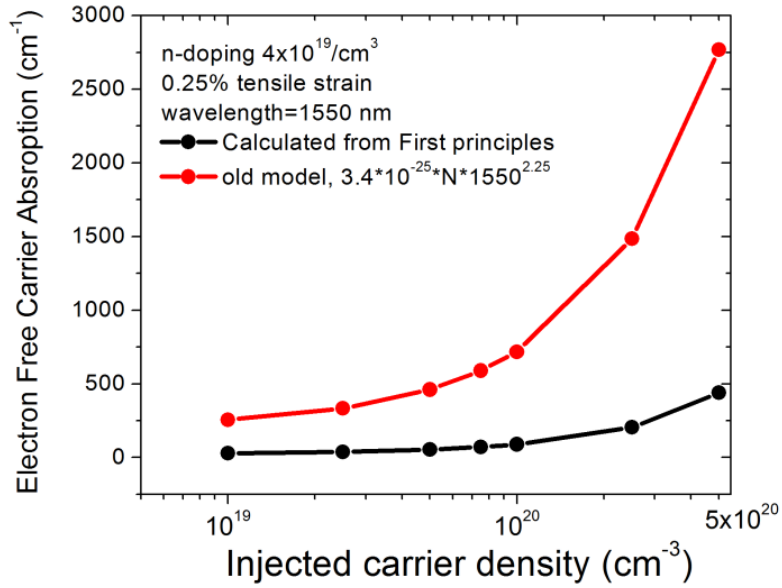


Figure 2.1 Free electron absorption coefficients at different electron injection levels calculated from first principles (black) and from λ^2 -dependent model [57] (red). Ge has $4 \times 10^{19} \text{ cm}^{-3}$ n-type doping level with 0.25% tensile strain [91].

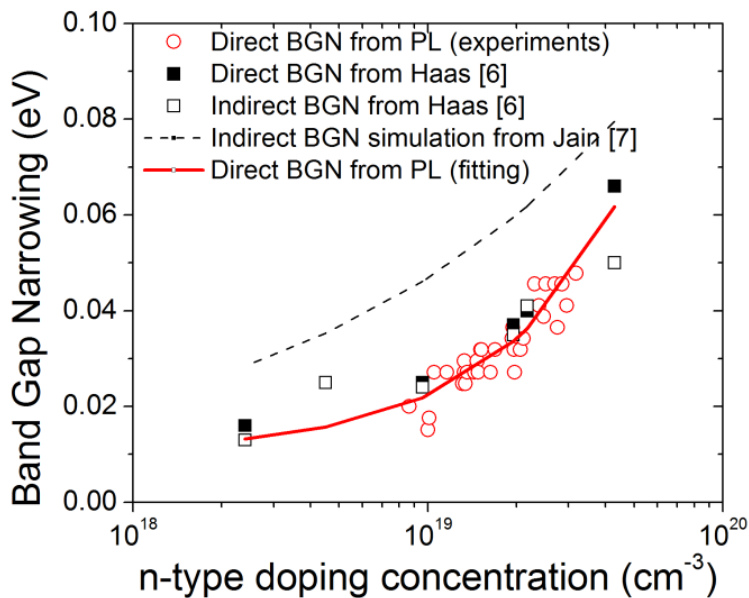


Figure 2.2 Direct and indirect BGN results in n-Ge at room temperature (T=300K). Solid squares represent direct BGN from Haas; empty squares represent indirect BGN from Haas [88]; dashed line represents Jain's equation for indirect BGN [92]; empty circles represent direct BGN derived from our PL measurements and solid line represents a linear fit of our experimental results (Note that the horizontal axis is in log scale so the fitting curve does not appear linear).

Jain and Roulston [92] pointed out that there are four major contributions to the BGN: (1) shift of the majority band edge due to exchange interactions; (2) shift of the minority band edge due to carrier-carrier or electron-hole interactions; (3) shift of the majority band edge due to carrier-impurity interactions; and (4) shift of the minority band edge due to carrier-impurity interactions. The Ref [92] gives an empirical expression for the indirect band gap narrowing while considering the above four interactions for n-Ge:

$$\Delta E_g^L = 8.67\left(\frac{N}{10^{18}}\right)^{1/3} + 8.14\left(\frac{N}{10^{18}}\right)^{1/4} + 4.31\left(\frac{N}{10^{18}}\right)^{1/2} \quad (2.1)$$

However, the above model overestimates the indirect BGN at room temperature shown in Figure 2.2 and that is due to the fact that the fitting parameters in this model were obtained at 80K. Furthermore, there is no complete theoretical model to explain the direct BGN in Ge yet. Figure 2.2 confirms that direct BGN due to heavy doping in Ge has to be included when calculating the Ge band gap. Due to the lack of a convincing physical explanation, we fit our direct BGN data with a linear relationship and thus, get an empirical equation [90]:

$$\Delta E_g^\Gamma = 0.013 \text{ eV} + 10^{-21} \text{ eV/cm}^{-3} \cdot N_D \quad (2.2)$$

The direct band gap E_g^Γ is 0.76 eV and indirect band gap E_g^L is 0.65 eV and the split energy of heavy hole (hh) and light hole (lh) is 0.02 eV when Ge has a 0.25% tensile strain [57]. Using Equation 2.2, we can get a direct BGN of $\Delta E_g^\Gamma = 0.06 \text{ eV}$ at a doping of $4.5 \times 10^{19} \text{ cm}^{-3}$. Because our data matches pretty well with Haas's results [88] on the direct BGN, we make the

assumption that the indirect BGN value is the same as ΔE_g^Γ considering the observed comparable narrowing for both direct and indirect BGN at room temperature that Haas showed. Therefore, for Ge with n-type doping concentration of $4.5 \times 10^{19} \text{ cm}^{-3}$, the direct band gap E_g^Γ is 0.70 eV and indirect band gap E_g^L is 0.59 eV. However, more studies on the indirect BGN are needed to confirm our assumption. The study of BGN in Ge is very important for the following optical gain calculation because the heavy doping and the resulting carrier-carrier and impurity-carrier interaction changes the Ge band structure.

2.2 Optical Gain Modeling

Direct optical band-to-band transition between the direct Γ valley of the conduction band (CB) and the split valence bands (VB) is calculated to determine the optical gain coefficient since Ge is a pseudo-direct band gap material. For simplicity, electron equilibrium distributions in the Δ -valleys have not been considered although the Δ -valleys are only 50 meV separated from the Γ valley minimum due to the inconsistent data on the deformation potential of the Δ valleys [93]. A more accurate simulation is to use 30 band $k \cdot p$ formalism to describe simultaneously the Δ , Γ , L, heavy-hole and light-hole bands all over the Brillouin zone and their dependences as a function of strain [94]. In our simulation, we assume a simple parabolic band structure while including the BGN effect with heavy n-type doping. We will compare the calculated gain coefficients with and without BGN effect and analyze the difference.

2.2.1 Optical Gain

Equation 1.6 in Chapter 1 is commonly used for optical gain calculation, where $f_c - f_v$ is the population inversion factor for direct band transitions. Only when $f_c - f_v > 0$, the optical gain can be positive. To calculate f_c and f_v using Equation 1.2 and Equation 1.3, a single quasi Fermi level exists for electrons in both the Γ valley and the L valleys because of the fast inter-valley scattering. At steady state, the electrons and the holes obey quasi Fermi distribution with respect to the electron quasi Fermi level and the hole quasi Fermi level, respectively. The inversion factor has to be considered separately for heavy hole and light hole due to the tensile strain induced valence band splitting. The optical gain coefficient is the sum of the transitions from both valence bands with respect to the corresponding absorption coefficient.

We plot the population inversion factor with injected carrier density for Ge with $N = 4.5 \times 10^{19} \text{ cm}^{-3}$ n-type doping and 0.25% tensile strain at $\lambda = 1600 \text{ nm}$ (Figure 2.3). Generally, the inversion factor increases with injected carrier density because the injected electrons and holes will fill the CBs and VBs and thus increase the Fermi levels. The reduction of the band gap energy with heavy doping can play a determining role for the inversion factor. If no BGN is introduced into the modeling, the heavy hole VB does not contribute to the inversion factor at $\lambda = 1600 \text{ nm}$ because the band gap energy is larger than the photon energy. If BGN is considered, both light hole and heavy hole VBs are involved in the population inversion for this wavelength. The inversion factor for the transitions between CB and light hole VB without BGN (dashed) is larger than that with BGN (solid) due to the smaller energy difference to the band edge and thus larger occupation possibility of electrons in the CB when the band gap is larger. Furthermore, the inversion factor increases with higher doping or more strain if we compare the photon energy near the band edge. The reason is that the two conditions can increase the Fermi level in the CB

and thus lead to higher occupation probability of electrons in the conduction band.

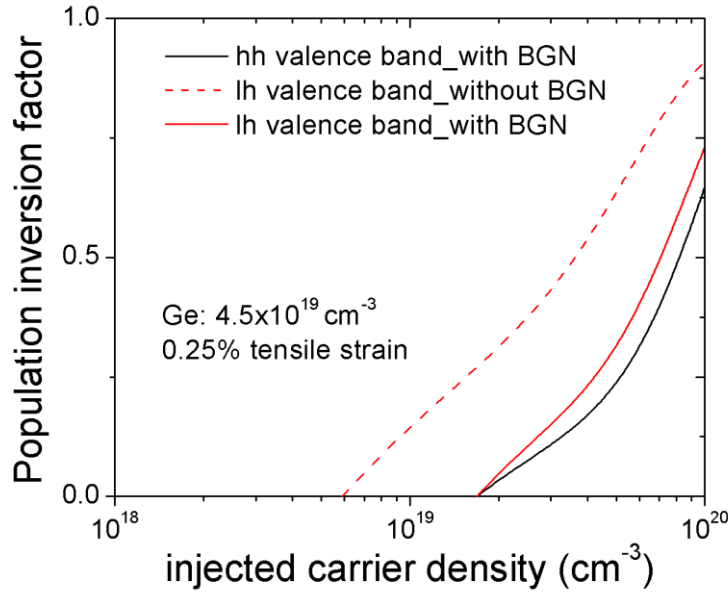


Figure 2.3 Population inversion factor with injected carrier density ranging from $1 \times 10^{18} \text{ cm}^{-3}$ to $1 \times 10^{20} \text{ cm}^{-3}$ for Ge with $4.5 \times 10^{19} \text{ cm}^{-3}$ n-type doping and 0.25% tensile strain at $\lambda=1600 \text{ nm}$.

Figure 2.4 shows the optical gain from the direct Γ transition in 0.25% tensile strained, n^+ Ge with $N=4.5 \times 10^{19} \text{ cm}^{-3}$ at different injected carrier densities with and without the BGN effect. The BGN effect decreases the direct band gap energy and therefore causes a red shift in the lasing wavelengths. When not taking the BGN into account our previous model indicates that there is no optical gain for wavelengths above 1630 nm. However, as indicated by the blue line in Figure 2.4, optical gain can be expected at $\lambda=1700 \text{ nm}$. The population inversion for lasing at 1700 nm occurs when the injected carrier density reaches $9 \times 10^{18} \text{ cm}^{-3}$. For a carrier injection density as high as $4.4 \times 10^{19} \text{ cm}^{-3}$, the optical gain can be $\sim 2000 \text{ cm}^{-1}$, significantly higher than the number predicted by the old model. Figure 2.4 also compares the optical gain at 1600 nm of the

previous model with the BGN modified calculations. The onset of optical gain is shifted to higher injected carrier density since the quasi Fermi levels have to enter deeper into the conduction and valence bands due to BGN. On the other hand, as the injection carrier density increases beyond $2 \times 10^{19} \text{ cm}^{-3}$ the optical gain is significantly larger than predicted by the previous model. Although the inversion factor with respect to light hole VB without BGN is larger than that with BGN as we see in Figure 2.3, the gain coefficient is higher when BGN is considered because of two reasons: (1) the contributions from both heavy hole and light hole valence bands; (2) the increase of joint density of states (JDOS) at the selected photon energy as the energy band gap decreases. These results indicate that the BGN shifts the gain spectrum to longer wavelengths and leads to a higher optical gain at low 10^{19} cm^{-3} injection densities.

Figure 2.5 shows the gain spectra modeled with and without BGN effect for different injected carrier densities from the direct band transitions of 0.25% tensile strained Ge with $4.5 \times 10^{19} \text{ cm}^{-3}$ n-type doping. At this doping level, the L valleys are not completely filled with electrons and the quasi Fermi level is 34.4 meV below the Γ valley. As previously mentioned, the optical gain spectra without the BGN effect cuts off at $\lambda > 1630 \text{ nm}$. When BGN is included, the spectra are extended to longer wavelengths. With $5 \times 10^{19} \text{ cm}^{-3}$ injected carrier density, the optical gain is $> 500 \text{ cm}^{-1}$ in a very broad wavelength range of 1500 nm - 1770 nm. Such a broad gain spectrum has indeed been demonstrated in Ref. [59].

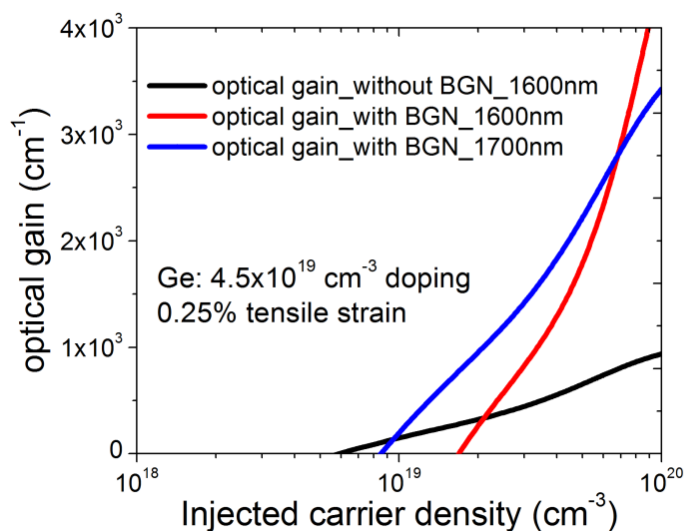


Figure 2.4 Optical gain from the direct transition in 0.25% tensile strained, n+ Ge with $N=4.5 \times 10^{19} \text{ cm}^{-3}$ at different injected carrier densities. The black line represents the optical gain calculated without BGN at $\lambda=1600 \text{ nm}$ and the red line represents the optical gain calculated with BGN at $\lambda=1600 \text{ nm}$. Blue line represents the optical gain calculated with BGN at $\lambda=1700 \text{ nm}$.

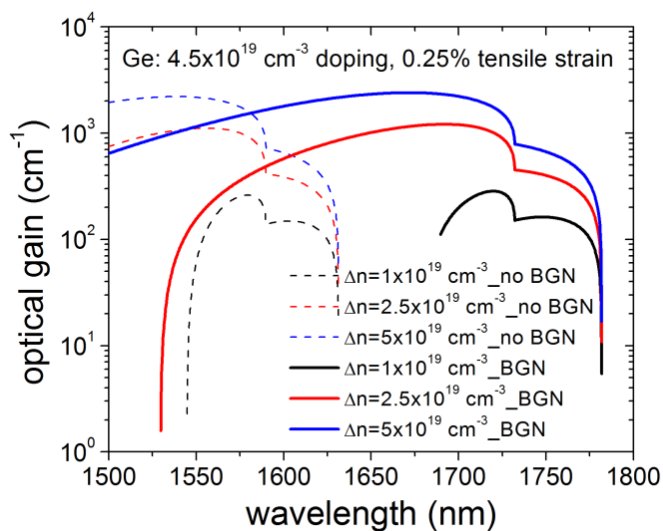


Figure 2.5 Gain spectra from the direct transition in 0.25% tensile strained n+ Ge with $N=4.5 \times 10^{19} \text{ cm}^{-3}$ at different injected carrier densities. Dashed lines are results from the model without BGN effect and solid lines are results from the modified model with BGN effect.

2.2.2 Net Materials Gain

When evaluating the lasing threshold current, the optical gain has to overcome all loss mechanisms related to the active gain medium, cladding materials and also mirror losses. If we consider the Ge active material only, the optical gain has to overcome the free carrier absorption in n-type doped Ge. We define “net materials gain” as the optical gain subtracted by the FCA in Ge. Free carrier absorption includes free electron absorption (contributed by n-type doping and injected electrons) and free hole absorption (contributed by injected holes). We use the free electron absorption derived from the first principle calculation in Chapter 2.1.1 and free hole absorption derived from the classic Drude model since there are no new experimental data for the free hole absorption in Ge. The equation to calculate free hole absorption is:

$$\alpha_{free\ hole} = -3.2 \times 10^{-25} p_v \lambda^{2.43} \quad [57] \quad (2.3)$$

Considering the BGN effect due to n^+ doping and correcting the overestimated free electron absorption in n-Ge, we plot the gain from the direct transition, free carrier loss and net gain as a function of injected carrier density in 0.25% tensile strained, n^+ Ge with n-type doping concentration of $4.5 \times 10^{19} \text{ cm}^{-3}$ at $\lambda=1600 \text{ nm}$ in Figure 2.6 and $\lambda=1700 \text{ nm}$ in Figure 2.7. All the calculations are for room temperature. At $\lambda=1700 \text{ nm}$, the injected carrier density to reach transparency is $1.13 \times 10^{19} \text{ cm}^{-3}$ and the differential gain a is $d\gamma/d\Delta n = 1.03 \times 10^{-16} \text{ cm}^2$. At $\lambda=1600 \text{ nm}$, the transparency carrier density is $2.5 \times 10^{19} \text{ cm}^{-3}$ and the differential gain a is $d\gamma/d\Delta n = 5.5 \times 10^{-17} \text{ cm}^2$. The free carrier absorption is mainly dominated by free hole absorption. Due to the lower JDOS in the conduction and valence bands at $\lambda=1700 \text{ nm}$ compared to the JDOS at $\lambda=1600 \text{ nm}$, the differential gain is higher at longer wavelength. Figure 2.8 shows a full scale of net materials gain change with injection carrier density at various wavelengths. The lasing can occur in a certain range of injected carrier densities between 10^{19} cm^{-3} and mid- 10^{20} cm^{-3} because

a minimum injection is required to reach population inversion and overcome the absorption loss, while the maximum injection is limited by the free carrier absorption losses. It shows a trend that lasing at the shorter wavelength requires higher injection current density while the maximum net materials gain is also higher due to the high JDOS.

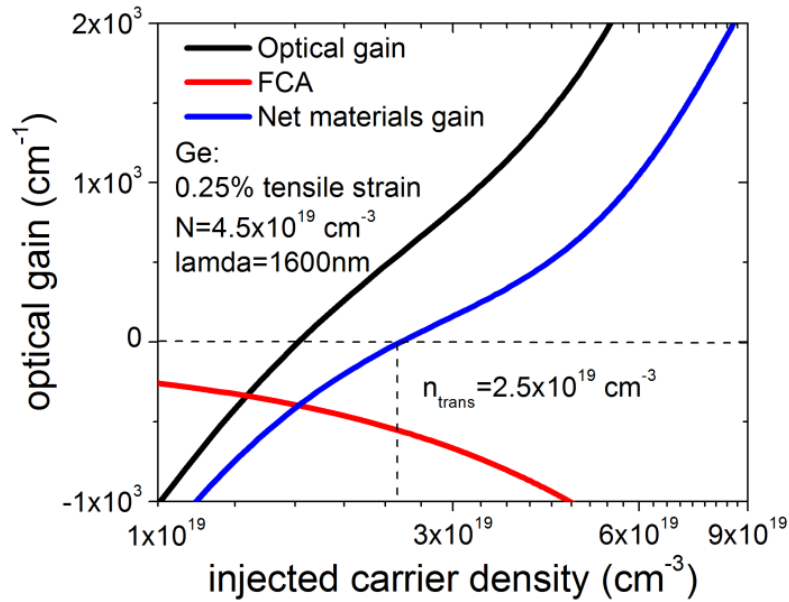


Figure 2.6 Gain from the direct transition, free carrier loss and net gain as a function of injected carrier density in 0.25% tensile strained, n+ Ge with $N=4.5 \times 10^{19} \text{ cm}^{-3}$ at $\lambda=1600 \text{ nm}$.

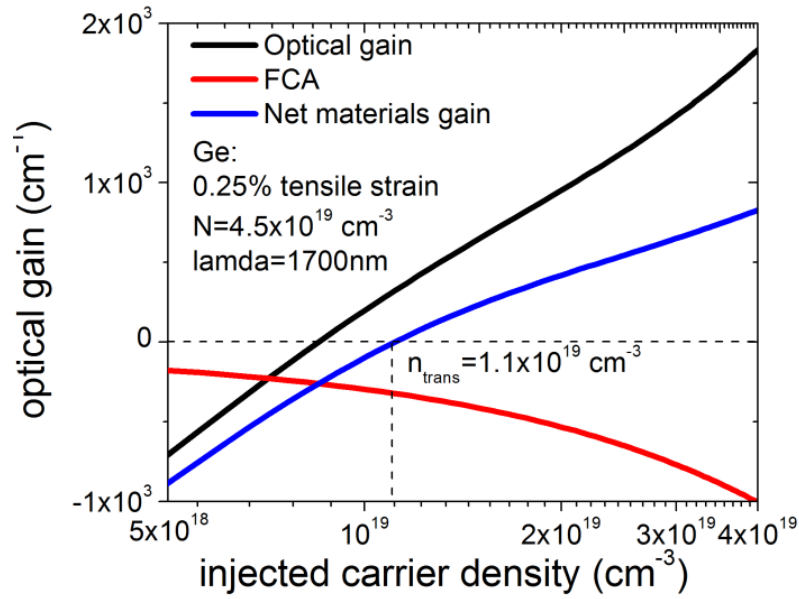


Figure 2.7 Gain from the direct transition, free carrier loss and net gain as a function of injected carrier density in 0.25% tensile strained, n+ Ge with $N=4.5 \times 10^{19} \text{ cm}^{-3}$ at $\lambda=1700 \text{ nm}$.

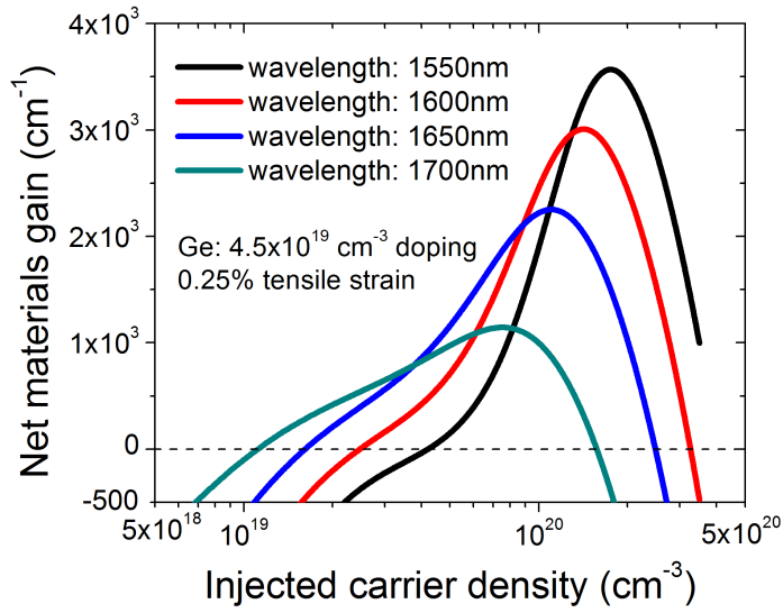


Figure 2.8 Net materials gain as a function of injected carrier density in 0.25% tensile strained, n+ Ge with $N=4.5 \times 10^{19} \text{ cm}^{-3}$ at $\lambda=1550 \text{ nm}$, 1600 nm , 1650 nm and 1700 nm .

2.2.3 Extended Ge Gain Bandwidth to Mid-IR

Tensile strain engineering can shrink the Ge band gap to longer wavelengths. Although emission at these wavelengths is not interesting for telecommunication applications, it shows large potential for the Ge light source to be used in the mid-IR range, such as mid-IR gas sensing, chemical sensing or imaging. Therefore, we calculate the Ge optical gain spectra with higher biaxial tensile strain of 1.8% and 2.5% using the previously discussed method, as shown in Figure 2.9. The Ge with 0.25% tensile strain is doped to $4.5 \times 10^{19} \text{ cm}^{-3}$ and Ge with 1.8% and 2.5% tensile strain is un-doped because tensile strain has already moved the Γ valley below the L valleys in the conduction band. In order to achieve optical gain of $\sim 1000 \text{ cm}^{-1}$, different injection levels are chosen, which are $3 \times 10^{19} \text{ cm}^{-3}$ for Ge with 0.25% strain, $1 \times 10^{19} \text{ cm}^{-3}$ for Ge with 1.8% strain and $2 \times 10^{18} \text{ cm}^{-3}$ for Ge with 2.5% strain. The trend is clear that higher strain can lower the required injection levels and hence the threshold current for lasing. Extended gain spectra to longer wavelengths are also shown in Figure 2.9. For Ge with 0.25% tensile strain, the gain bandwidth is 1550 nm \sim 1750 nm; For Ge with 1.8% tensile strain, the gain bandwidth is 1800 nm \sim 2400nm; For Ge with 2.5% tensile strain, the gain bandwidth is 2400 nm \sim 3000 nm. The theoretical gain calculation predicts that Ge has great potential to lase at a longer wavelength range with the benefit of low threshold current and quantum efficiency.

Furthermore, we evaluate the n-type doping effect on the Ge optical gain when Ge has tensile strain up to 1.8% and 2.5%. We find that the doping still enhance the optical gain because there are more available electrons in the Γ valley to contribute to the direct transition (Figure 2.10).

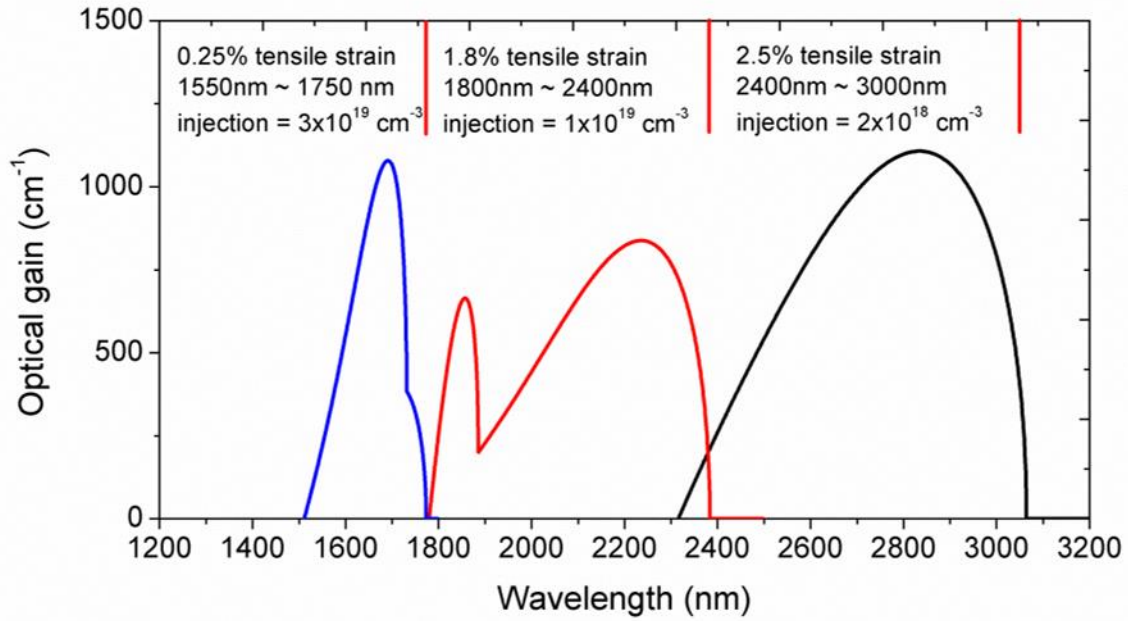


Figure 2.9 Optical gain spectra for Ge with tensile strain of 0.25%, 1.8% and 2.5% respectively.

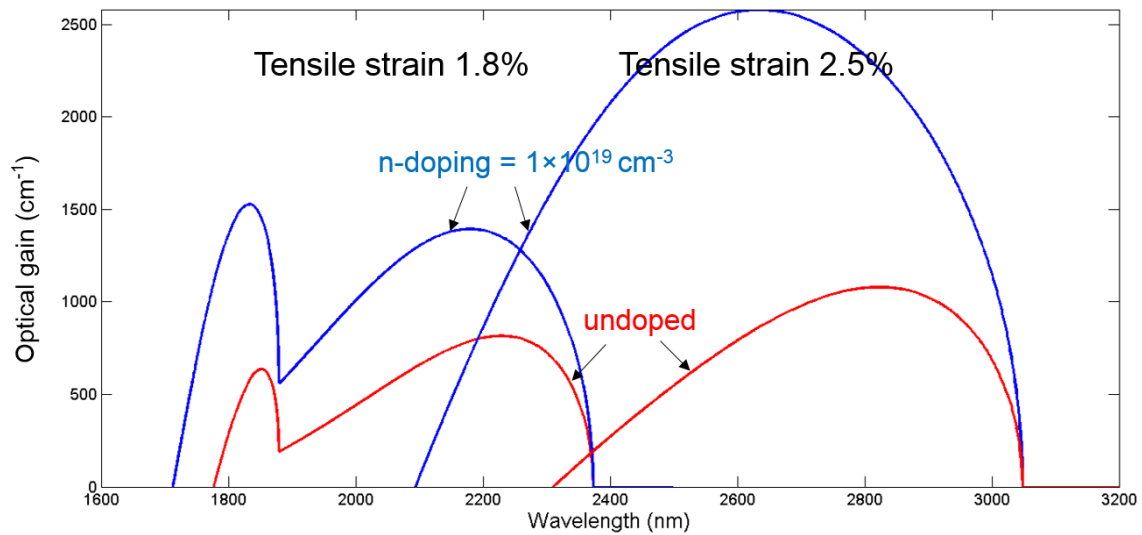


Figure 2.10 Optical gain spectra for un-doped Ge and n-type doped Ge with 1.8% and 2.5% respectively.

2.3 Temperature Dependent Optical Performances of Ge

Compared to direct band gap III-V materials, Ge exhibits a different temperature dependent optical performance, for instance in photoluminescence spectroscopy (PL). It has been experimentally shown that the integrated PL from n-Ge with a doping concentration of $1 \times 10^{19} \text{cm}^{-3}$ increases with temperature up to 100 °C [95]. This kind of temperature behavior can be very beneficial for Ge devices since the environmental temperature for Ge light sources in a microprocessor might be above room temperature due to the heat generation from the electronics. Furthermore, it is very interesting to study the PL performance of n-Ge at other doping levels with temperature, as well as the temperature dependence of the materials gain and laser threshold current.

2.3.1 Photoluminescence Dependence with Temperature

The Ge samples for PL measurements are epitaxial films grown on Si (100) substrate with a standard two-step growth [26]. Ge films with doping concentration of $1 \times 10^{19} \text{cm}^{-3}$ are prepared by an *in situ* doping method. Ge films with doping concentration of $3 \times 10^{18} \text{cm}^{-3}$ are prepared by the *in situ* doping method and followed by annealing at 850 °C for 40min. Ge films with doping concentration of $2 \times 10^{19} \text{cm}^{-3}$ are prepared by the delta doping method [96] and followed by chemical mechanical polishing [97]. The detailed Ge doping technique will be discussed in details in Chapter 3. We use a Horiba LabRam microPL system with a 1064nm laser and liquid nitrogen cooled InGaAs detector for the PL measurements. Ge samples are located inside of a

small chamber where the temperature can be adjusted and controlled by liquid nitrogen cooling and electrical heating. The temperature measurement range for PL is from 150K to 433K. Figure 2.11 shows the PL spectra measured at various temperatures for Ge doped to $3 \times 10^{18} \text{ cm}^{-3}$. These PL spectra have been corrected taking the grating efficiency curve and photodetector responsivity curve into account. The peak positions of PL spectra shift to longer wavelength with increasing temperature because the band gap is shrinking with temperature. The maximum intensity of the PL spectra shows an increasing trend up to $\sim 80 \text{ }^\circ\text{C}$ and then starts to decrease. The PL spectrum usually broadens by $2kT$, however, we measure a larger full width half maximum (FWHM) for all the PL spectra from different Ge samples (Figure 2.12). The black curve shows the expected $2kT$ broadening and the dotted data are measured FWHM from intrinsic bulk Ge, Ge thin film of doping at $3 \times 10^{18} \text{ cm}^{-3}$ and Ge thin film of doping at $2 \times 10^{19} \text{ cm}^{-3}$. However, Sun measured the PL spectra with normal $2kT$ broadening with similar samples but from a different PL setup [98]. The FWHM broadening difference might come from the measurement system. We need a standard sample with a known FWHM to estimate the system error. For the current sets of data, we think the integrated PL intensities directly related with the FWHM are not suitable for further analysis. Instead, we use the PL peak emission intensity or maximum intensity as the key feature to understand the Ge PL performance with temperature.

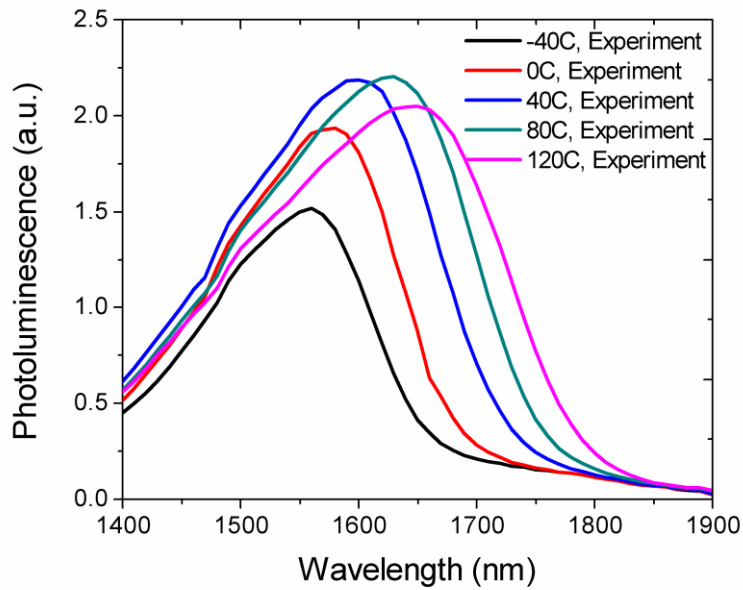


Figure 2.11 Photoluminescence spectra measured for the Ge thin film with n-type doping concentration of $3 \times 10^{18} \text{ cm}^{-3}$ at temperatures of $-40 \text{ }^\circ\text{C}$, $0 \text{ }^\circ\text{C}$, $40 \text{ }^\circ\text{C}$, $80 \text{ }^\circ\text{C}$ and $120 \text{ }^\circ\text{C}$, respectively.

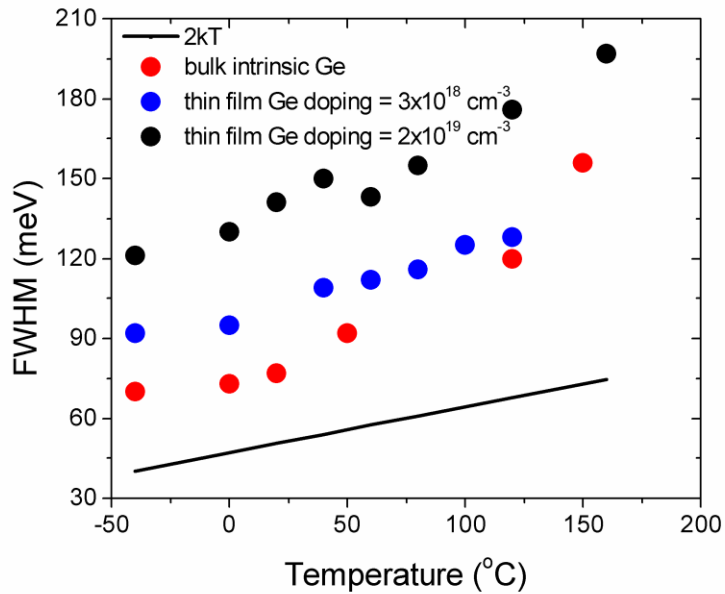


Figure 2.12 FWHM for PL spectra for different Ge samples compared to $2kT$ broadening

2.3.2 Photoluminescence Simulation

In order to fully understand the PL performance with temperature, we simulate the spontaneous emission under different temperatures. We first assume that the PL reduction at high temperature is only due to the wider Fermi distribution. Only the direct Γ valley and the indirect L valleys are considered. The simulation result is shown in Figure 2.13. The PL intensity is calculated by the following model:

$$I(\text{PL}) \propto n_0^\Gamma p_0 \quad (2.4)$$

where n_0^Γ is the electron population in the Γ valley by both n-type doping and carrier injection and p_0 is the hole population in the valence bands. In the simulation result (solid red line), the thermalization process of electrons from the indirect L valleys to the direct Γ valley dominates and maximum PL intensity keeps increasing with temperature. The y-axis of Figure 2.13 is in an arbitrary unit and therefore, the maximum PL intensity is dependent on normalization. It is very apparent that the simulation does not match with our experimental observation (open squares). The reason is that the density of states (DOS) reduction with temperature is not large enough to dominate over the increase of electrons in the direct Γ valley due to thermalization. Therefore, this PL simulation model is too simple that we need to consider other effects which probably contribute to the PL intensity reduction at high temperature.

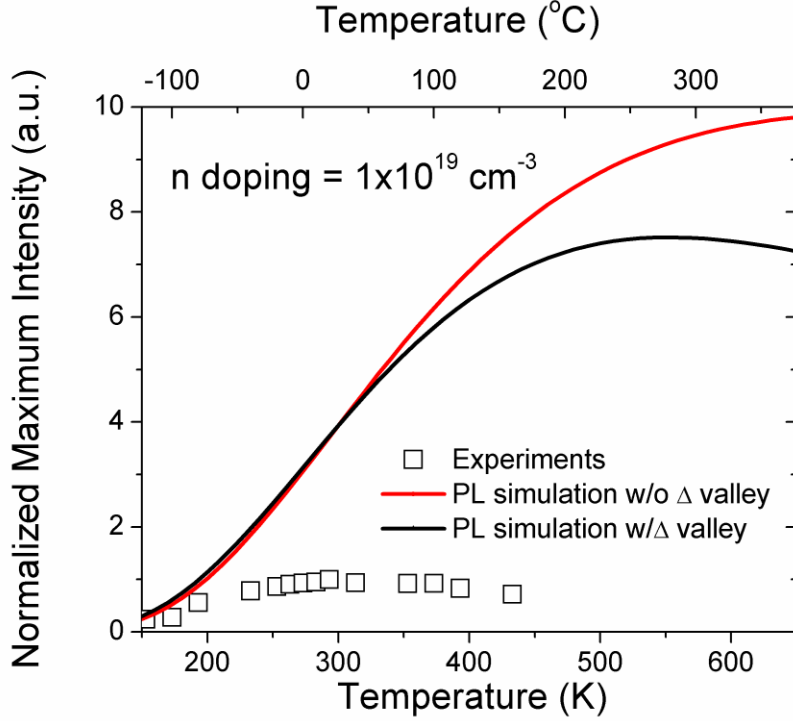


Figure 2.13 Normalized maximum intensity from PL spectra with temperature for the Ge-on-Si thin film with $N=1 \times 10^{19} \text{ cm}^{-3}$. The red line is the simulation result without considering the Δ valley and the non-radiative recombination. The black line is the simulation result considering the Δ valley but no non-radiative recombination.

2.3.2.1 Effect of the Δ Valleys on PL

In the Ge band structure, the Δ valley in the conduction band is only 50 meV above the direct Γ valley. It is possible that the electrons will be thermalized to the Δ valley from the L valley at high temperature and thus affect the direct band gap PL at the Γ valley. To analyze the effect of the Δ valley on PL, we will consider the carrier distribution equilibrium among the Γ valley, the L valley and the Δ valley. Due to the lack of material parameters at the Δ valley, we assume the effective electron mass at the Ge Δ valley is the same as the effective electron mass at the Si Δ valley, which is $0.321 m_0$ [99]. We assume the band gap energy of the Δ valley is always 50 meV

higher than the direct Γ valley under different temperatures. In Figure 2.13, the black line represents the simulation result considering the thermalization of electrons from the L valleys to both the Γ valley and the Δ valley. The simulation result shows a maximum PL drop at the temperatures higher than 277 °C, indicating that the Δ valley plays a significant role on the photoluminescence at high temperatures. We cannot simply neglect the Δ valley when we discuss the Ge high temperature photoluminescence. However, the predicted PL turning temperature with the consideration of the Δ valley contribution is still higher than the experimental results. The inconsistency brings us to consider the non-radiative recombination in the Ge film due to the high threading dislocation density.

2.3.2.2 Effect of Non-radiative Recombination on PL

In this part, we make an assumption that the non-radiative recombination also contributes to the PL reduction with temperature. Since the Ge film on Si is about 500 nm ~ 1000 nm thick, we assume that the excess carrier generated by laser excitation is uniform through the film depth and reabsorption is not considered in the simulation due to small path length. The Shockley-Read-Hall (SRH) recombination due to threading dislocations and surface recombination are two types of non-radiative recombination mechanisms considered in the simulation, similar as in Ref [100, 101]. Auger recombination is not included because there is no consistent data with temperature dependence from the literature. First, we calculate the injected electron concentration Δn^Γ into the direct Γ valley, Δn^Δ into the indirect Δ valleys and Δn^L into the indirect L valleys by solving a detailed balance equation to obtain the steady state $\frac{\partial \Delta n}{\partial t} = 0$, which means the carrier generation rate equals to the carrier recombination rate [102]. Because we assume a uniform excess carrier

distribution through the film depth, the carrier generation rate $G = \frac{P}{hc/\lambda V_{Ge}}$, where P is the pump power and V_{Ge} is the Ge excitation volume. Recombination includes direct band gap radiative recombination R_{rad}^Γ , indirect band gap radiative recombination R_{rad}^L and R_{rad}^Δ , SRH recombination R_{SRH} and surface recombination R_{surf} . These recombination rates can be represented by the following well-known equations [102, 103]:

$$R_{rad}^\Gamma = B^{\Gamma c\Gamma v}[(n_0^\Gamma + \Delta n_0^\Gamma)(p_0 + \Delta p) - n_0^\Gamma p_0] \quad (2.5)$$

$$R_{rad}^L = B^{Lc\Gamma v}[(n_0^L + \Delta n_0^L)(p_0 + \Delta p) - n_0^L p_0] \quad (2.6)$$

$$R_{rad}^\Delta = B^{\Delta c\Gamma v}[(n_0^\Delta + \Delta n_0^\Delta)(p_0 + \Delta p) - n_0^\Delta p_0] \quad (2.7)$$

$$R_{SRH} = \frac{(n_0 + \Delta n)(p_0 + \Delta p) - n_i^2}{\tau_p(n_0 + \Delta n + n_1) + \tau_n(p_0 + \Delta p + p_1)} \quad (2.8)$$

$$R_{surf} = \frac{(n_0 + \Delta n)(p_0 + \Delta p) - n_i^2}{(n_0 + \Delta n)/s_p + (p_0 + \Delta p)/s_n} \quad (2.9)$$

$B^{\Gamma c\Gamma v} = 1.3 \times 10^{-10} \text{ cm}^3/\text{s}$ in Equation 2.5 is the direct gap recombination coefficient [104]. $B^{Lc\Gamma v} = 5.1 \times 10^{-15} \text{ cm}^3/\text{s}$ in Equation 2.6 is the indirect gap recombination coefficient [104]. Due to the lack of material parameter in the Δ valley, we assume $B^{\Delta c\Gamma v}$ is the same as $B^{Lc\Gamma v}$ in Equation 2.7. n_0^Γ , n_0^Δ and n_0^L are electron concentrations in the direct and indirect conduction bands, respectively with an equilibrium equation that *Doping* $n_0 = n_0^\Gamma + n_0^L + n_0^\Delta$. Δn_0^Γ , Δn_0^Δ and Δn_0^L are injected electron concentrations in the direct and indirect conduction bands, respectively with an equilibrium equation that $\Delta p = \Delta n = \Delta n_0^\Gamma + \Delta n_0^L + \Delta n_0^\Delta$. n_0 and p_0 are the equilibrium electron and hole concentrations after n-type doping and n_i is the intrinsic carrier concentration under certain temperature.

SRH recombination is normally through some defect levels in the band gap. In Equation 2.8, n_1 and p_1 are related to the deep defect states with the relations $n_1 = n_i e^{(E_T - E_i)/kT}$ and $p_1 = n_i e^{(E_i - E_T)/kT}$. In the simulation, we make an assumption that the defect level is right in the mid-

gap that $E_T = E_i$ for simplicity. τ_p and τ_n in Equation 2.8 are the lifetime for holes and electrons related to the defects and they are widely observed to have doping and temperature dependence in Silicon [103, 105]. Since Ge is n-type doped, the Fermi level is close to the conduction band. From Ref. [106], we learn that the charged kink sites (non-radiative recombination centers or dangling bonds) increases with n-type doping when the doping is above 10^{18} cm^{-3} . The non-radiative recombination lifetime is doping dependent. Since the doping dependence can be generally approximated by an empirical expression [105] as Equation 2.10, we can extract the coefficient n_{ref} and γ by fitting the curve of number of charged kink site versus doping in Ref. [106].

$$\tau_p(n, 300K) = \frac{1}{\sigma_p v_p N_k N_{\text{dislocation}}} \quad (2.10)$$

$$N_k = N_{k0} \times \left(1 + \left(\frac{n}{n_{\text{ref}}}\right)^\gamma\right) / \text{cm} \quad (2.11)$$

We assume the SRH recombination is related to the threading dislocation. n is the doping concentration and n_{ref} means a threshold doping concentration measuring when dopant seems to be important to affect the electron recombination with hole through defects. The effective capture cross-section of the deep defect state traps related to the threading dislocation is $\sigma_p = 4 \times 10^{-14} \text{ cm}^2$ at 300K [107]. We assume the defect states are localized in the k-space. The threading dislocation density is $N_{\text{dislocation}} = 1 \times 10^8 \text{ cm}^{-2}$ for the 1 μm thick Ge film after high temperature anneal. Normally, the number of charged kink sites (dangling bonds) is small compared to the number of sites on the dislocation line, less than 5% [108]. If we assume the number of kink sites without doping is 2% of the number of sites on the $\langle 110 \rangle$ dislocation line in Ge, the number of kink sites per unit length of dislocation is $N_{k0} = 2.5 \times 10^5 / \text{cm}$, which is similar to the number mentioned in Ref. [107]. The thermal velocity of hole is $v_p = 1.9 \times$

10^7 cm/s . The extracted $n_{\text{ref}} = 1 \times 10^{18} \text{ cm}^{-3}$ and $\gamma = 0.63$ in Equation 1.20. Therefore the $\tau_p(n, 300K)$ at the doping concentration of $1 \times 10^{19} \text{ cm}^{-3}$ is 10 ns.

SRH recombination also usually has temperature dependence that higher temperature means the larger kinetic energy of carriers and then higher probability to recombine. Ref. [109] gives an approximation equation:

$$\tau_{p,T} = \tau_{p,300K} e^{(-T_\alpha \times (\frac{T}{300K} - 1))} \quad (2.12)$$

where T_α is a positive coefficient so that we expect a decrease of minority carrier lifetime with rising temperature. T_α is a fitting parameter in the simulation. The temperature dependence is controlled by the hole thermal velocity v_p and the capture cross-section σ_p [105]. For the electron lifetime $\tau_{n,T}$, we make a reasonable assumption that it is the same as the hole. Because the non-radiative recombination rate due to electron has to be weighed with the hole carrier concentration, the contribution of non-radiative recombination from electrons will be small in the n-type doped Ge.

Since the Ge-on-Si film is unpassivated, we assume the surface recombination velocity s is 800 cm/s [101]. In Equation 2.9, $s_p = s_n = s/\text{depth}$ where the depth is the excitation depth in Ge which is set to be 500 nm in the simulation. In the overall simulation, we only assume the SRH recombination is temperature dependent and all the other recombination mechanisms have no temperature dependence.

Once the excess injected carrier concentrations into different valleys have been determined, we can calculate the PL spectra as the direct radiative transitions with energy E_{ph} between electrons in the direct Γ valley and holes in the valence bands (both light hole band and heavy hole band induced by 0.25% biaxial tensile strain), a simple expression can be used as the following:

$$PL(E_{ph}) \propto DOS_n(E_{ph})f_n(E_{ph})DOS_p(E_{ph})f_p(E_{ph}) \quad (2.13)$$

where $DOS_n(E_{ph})f_n(E_{ph})$ and $DOS_p(E_{ph})f_p(E_{ph})$ are the electron and hole populations in the direct Γ valley and valence bands for the transition energy of E_{ph} , respectively. During the calculation, we use quasi Fermi level E_{Fn} for electrons and E_{Fp} for holes to describe the non-equilibrium condition of the excess injected carriers. Table 2.1 lists all the parameters related to Ge material in our PL calculations.

Table 2.1 Values for the germanium material parameters used in our calculations

Parameter	Value	Parameter	Value
Generation rate G	$4.3 \times 10^{26} \text{ cm}^{-3}/\text{s}$	T_α	2
$B^{\Gamma_c \Gamma_v}$	$1.3 \times 10^{-10} \text{ cm}^3/\text{s}$	Surface recombination velocity s	800 cm/s
$B^{L_c \Gamma_v}$	$5.1 \times 10^{-15} \text{ cm}^3/\text{s}$	n_{ref}	$1 \times 10^{18} \text{ cm}^{-3}$
N_{k0}	$2.5 \times 10^5 / \text{cm}$	γ	0.63

We use the above model to simulate PL spectra at different temperatures. Figure 2.14 plots both the experimental and theoretical PL spectrum for Ge doped to $3 \times 10^{18} \text{ cm}^{-3}$ at 40 °C as an example. The calculated peak position matches pretty well with the PL spectrum, which is mainly dependent on the Ge band gap. Since Ge is tensile strained, the valence band splits into heavy hole and light hole. Therefore, there are two overlap peaks in the simulated spectrum while the higher peak is contributed mainly by the light hole and the other is mainly contributed by the heavy hole. However, the calculated FWHM is close to 2kT while the actual FWHM is $\sim 4\text{kT}$. We plot the simulated PL spectra for various temperatures for Ge doped to $3 \times 10^{18} \text{ cm}^{-3}$ in Figure 2.15. Compared with the experimental results in Figure 2.11, the simulated PL spectra

match pretty well regarding the peak position shift and peak intensity change, which makes us believe the validity of our assumptions and calculations.

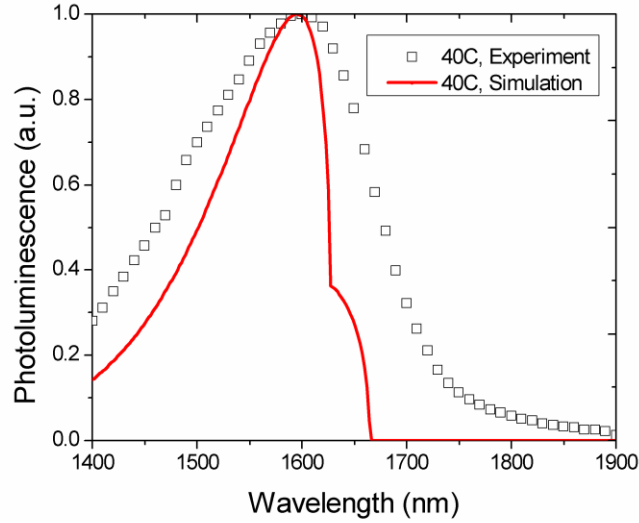


Figure 2.14 Photoluminescence spectrum measured for the Ge thin film with n-type doping concentration of $3 \times 10^{18} \text{ cm}^{-3}$ at 40 °C (open square). The solid line is the simulation result.

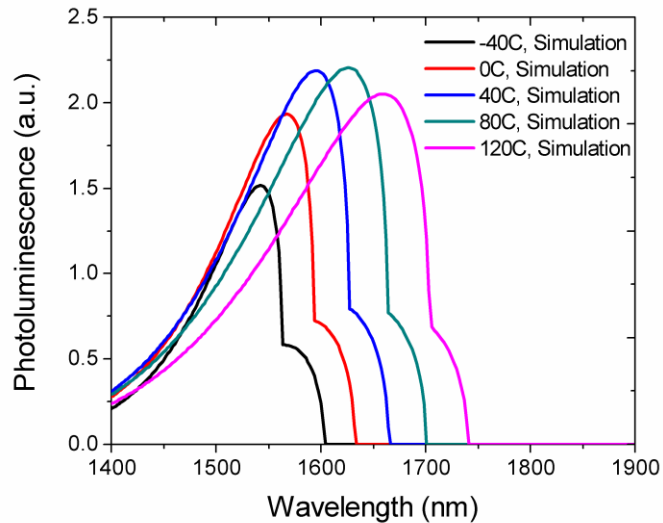


Figure 2.15 Calculated photoluminescence spectra for the Ge thin film with n-type doping concentration of $3 \times 10^{18} \text{ cm}^{-3}$ at temperatures of -40 °C, 0 °C, 40 °C, 80 °C and 120 °C, respectively.

We extract the maximum PL intensities from the above PL spectra and plot them with temperature in Figure 2.16 for Ge doped to $3 \times 10^{18} \text{ cm}^{-3}$. The maximum intensity peaks around $80 \text{ }^\circ\text{C}$ with a good agreement between the experimental results and simulation results. Similarly, Figure 2.17 plots maximum PL intensity with temperature for Ge thin films with n-type doping concentration of $1 \times 10^{19} \text{ cm}^{-3}$ with the maximum intensity peaking around $50 \text{ }^\circ\text{C}$. From the agreement of the experiment and simulation, we can conclude that the assumptions of the Δ valleys and non-radiative recombination are reasonable to explain the PL performance with temperature in the n-Ge films.

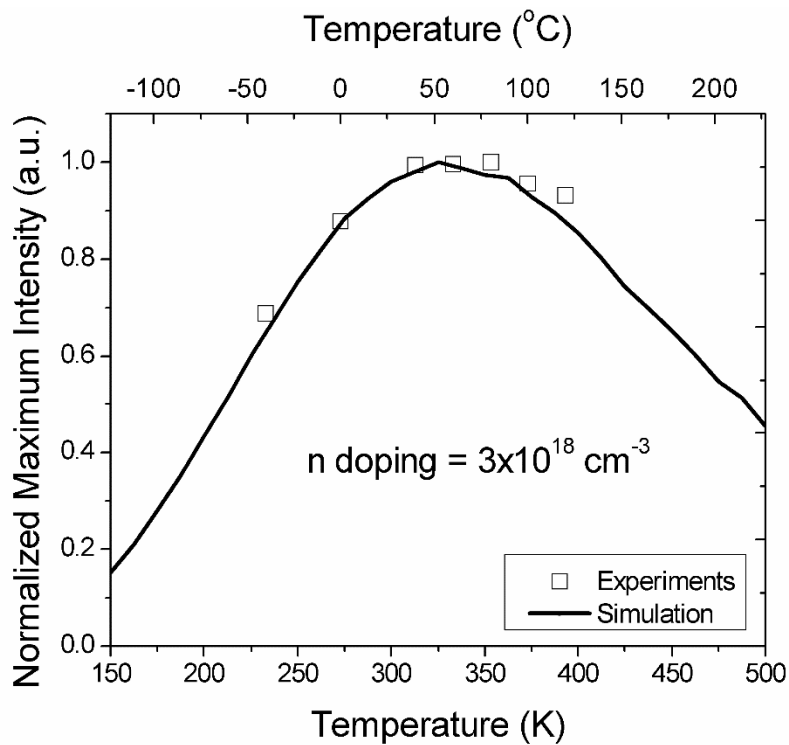


Figure 2.16 Maximum PL intensity with temperature for the Ge thin film doped to $3 \times 10^{18} \text{ cm}^{-3}$

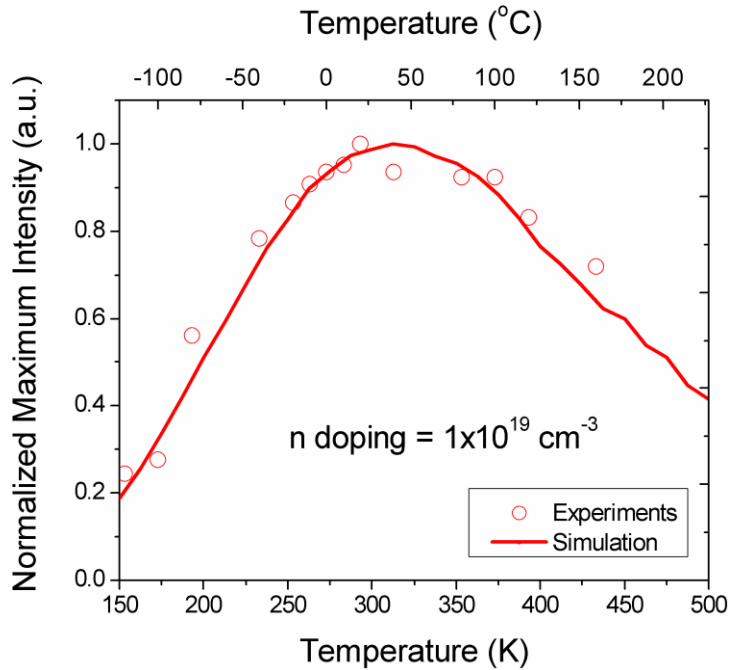


Figure 2.17 Maximum PL intensity with temperature for the Ge thin film doped to $1 \times 10^{19} \text{ cm}^{-3}$

2.3.3 Materials Gain Dependence with Temperature

The detailed net materials gain calculation at room temperature has been discussed in the previous paragraph. From the above PL simulation with temperature, we find that the two assumptions of the Δ valley and the non-radiative recombination are reasonable to consider especially under high temperature. The materials gain is different from the photoluminescence where materials gain measures the net transition rate of radiative emission over absorption and PL measures the radiative emission only. Therefore, it is interesting to investigate the trend of materials gain with temperature for n-Ge.

From Section 2.3.2, we know that the effective carrier concentration injected Ge changes with temperature at the same injection rate because the distribution of injected carriers to

radiative recombination and non-radiative recombination varies with temperature. Therefore, it is not appropriate to consider materials gain under a certain injected carrier concentration. Instead, we compare peak materials gain with temperature under a certain injection rate G . Similarly as the previous part, we can get the effective excess carrier concentration by solving the equilibrium between the recombination rate and the injection rate. Figure 2.18a plots the peak materials gain with temperature for n-Ge with various doping concentrations compared with the InGaAsP material. The peak materials gain is defined by the maximum gain in the net materials gain spectrum with wavelength. Different injection rates are chosen to achieve similar net materials gain of 500 cm^{-1} around room temperature for n-Ge doped to different levels and InGaAsP as well in order to compare their gain dependence with temperature. In Figure 2.18b, we plot the effective injected carrier density into Ge over the temperature of 200K to 450K. At higher temperatures, the non-radiative recombination rate increases and thus the effective injected carrier concentration contributed to radiative recombination reduces. Although the PL increases with temperature in Ge, the materials gain shows a singular decreasing trend with temperature. The influence of temperature on the materials gain mainly resulted from three effects: (1) the relative distribution of the electron between the direct Γ valley, the indirect L valleys and Δ valleys; (2) the fraction of the electrons and holes contributing to the light emission at the given photon energy; (3) the fraction of carriers contributing to the radiative recombination. The second and third effects dominate the temperature dependent gain. In the temperature dependent PL, there is no effect from the fraction of hole contribution and thus, PL shows a different temperature behavior than the materials gain.

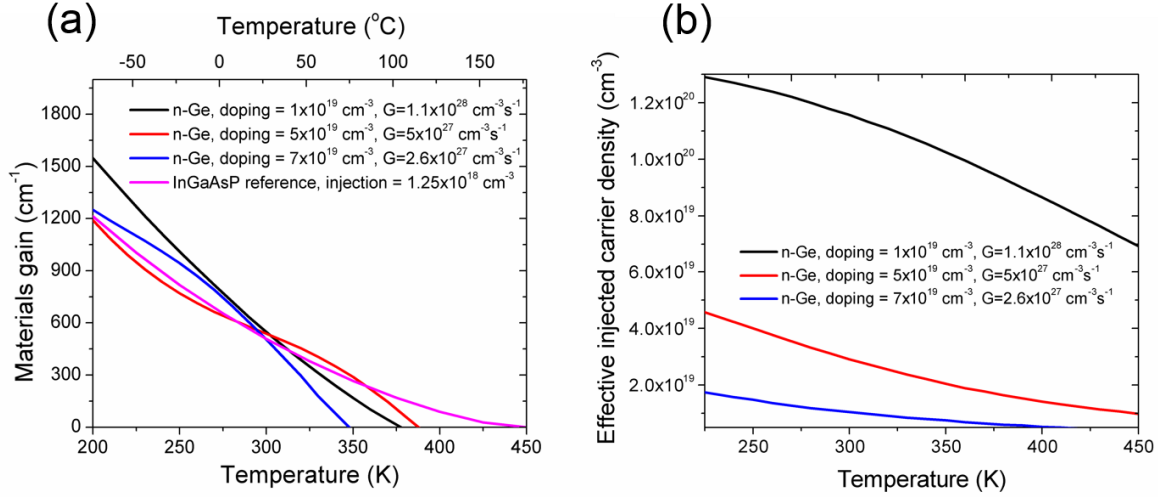


Figure 2.18 (a) Net materials gain simulation with temperature. We use InGaAsP material as the reference. Gain curves are plotted for Ge doped to $1 \times 10^{19} \text{ cm}^{-3}$, $5 \times 10^{19} \text{ cm}^{-3}$ and $7 \times 10^{19} \text{ cm}^{-3}$ respectively. (b) The effective injected carriers for radiative recombination under various temperatures considering the non-radiative recombination.

As shown in Figure 2.18a, materials gain from InGaAsP is calculated as a reference and non-radiative recombination is not considered. Therefore, a constant injected carrier density of $1.25 \times 10^{18} \text{ cm}^{-3}$ is used. The materials gain decreases with temperature due to a wider carrier distribution above the band edges and lower density of states at the peak gain, which is typical in the III-V laser material. In Ge, the injected carrier concentration (Figure 2.18b) to reach the similar gain is much higher than InGaAsP because injected carriers have to fill the indirect L valleys and to compensate the free carrier absorption loss due to extrinsic n-type doping. When Ge is doped to different levels, the gain drops with temperature. The required injection rate and thus effective injected carrier density is lower to reach the same materials gain around room temperature for higher n-type doping, which is due to the electron band filling from the L valleys to the Γ valley. We get the slopes dg/dT from each gain curve around room temperature as a

parameter to measure the temperature dependence of the net materials gain. The results are $-8.46 \text{ cm}^{-1}\text{K}^{-1}$ for n-Ge doped to $1 \times 10^{19} \text{ cm}^{-3}$, $-4.10 \text{ cm}^{-1}\text{K}^{-1}$ for n-Ge doped to $5 \times 10^{19} \text{ cm}^{-3}$, $-10.2 \text{ cm}^{-1}\text{K}^{-1}$ for n-Ge doped to $7 \times 10^{19} \text{ cm}^{-3}$ and $-5.5 \text{ cm}^{-1}\text{K}^{-1}$ for InGaAsP. The smaller slope means that gain changes less with temperature. When n-type doping is $7 \times 10^{19} \text{ cm}^{-3}$ in Ge, Fermi level of electron almost reaches the bottom of the Γ valley and Ge is a pseudo-direct band gap material. Therefore, materials gain reduces rapidly with temperature. When n-type doping concentration is mid- 10^{19} cm^{-3} in Ge, the indirect L valleys are filled mostly by the extrinsic doping and thermalization from the L valleys to the Γ valley can counteract partially the reduction of the peak density of states at higher temperature. However, the effective injected carrier density reduction with temperature due to non-radiative recombination still dominates and therefore, the materials gain drops with temperature for Ge doped to mid- 10^{19} cm^{-3} . If n-type doping concentration is $1 \times 10^{19} \text{ cm}^{-3}$ in Ge, the indirect L valleys have very few filled electrons and thus the contribution of thermalization to increase the gain is small. From the above discussion, we can conclude that n-Ge doped to mid- 10^{19} cm^{-3} has best gain coefficient stability with temperature but not significantly different compared to other doping concentrations. N-Ge doped to mid- 10^{19} cm^{-3} also has a slightly better gain stability than InGaAsP.

2.4 Threshold Current Density Prediction

Equation 1.12 $I_{th} = \frac{qV}{\eta_i \tau} (N_{tr} + \frac{\alpha_i + \alpha_m}{\Gamma a})$ gives a general expression to calculate the threshold current for any laser device. With regard to Ge, the carrier lifetime τ is related to the non-radiative recombination, transparency carrier density N_{tr} and differential gain a are related to the optical gain calculation and internal quantum efficiency η_i , absorption loss α_i , mirror loss α_m ,

active region volume V , active region confinement factor Γ are all related to the device designs. Here we choose some typical and reasonable values for the device design parameters. We assume an ideal diode with shunt resistance so that $\eta_i = 1$, absorption loss from cladding layer is 100 cm^{-1} , mirror loss is 8 cm^{-1} and the Ge waveguide has $1 \text{ }\mu\text{m}$ width, 250 nm height and $300 \text{ }\mu\text{m}$ length. We plot the threshold current density in Figure 2.20 with various doping concentrations. The emission wavelengths are chosen to be at the peak gain position for each doping concentration. Generally, the threshold current reduces with doping because n-type doping helps to fill the L valleys and decreases the required injected carrier density to reach transparency. At the doping level of $1 \times 10^{19} \text{ cm}^{-3}$, the calculated threshold current density at 300K is $\sim 30 \text{ kA/cm}^2$. The value is comparable with the threshold current of our optically pumped Ge laser which demonstrated the lasing at 30 kW/cm^2 pump power [58], which can be roughly translated to 25 kA/cm^2 in electrical current density.

In Figure 2.21, we plot the laser threshold current densities with temperature ranging from 200K to 450K for Ge doped to different levels. The general trend is that threshold current arises with temperature. There are two main factors contributing to the increase. One reason is that the non-radiative recombination rate is faster at higher temperature, which reduces the minority carrier lifetime. The other reason is because of the wider carrier distribution above the band edges, lowering the density of states at higher temperature. The thermalization process where electrons at the L valleys can be thermalized to the Γ valley at elevated temperature plays a role to slow down the threshold current increasing trend with temperature.

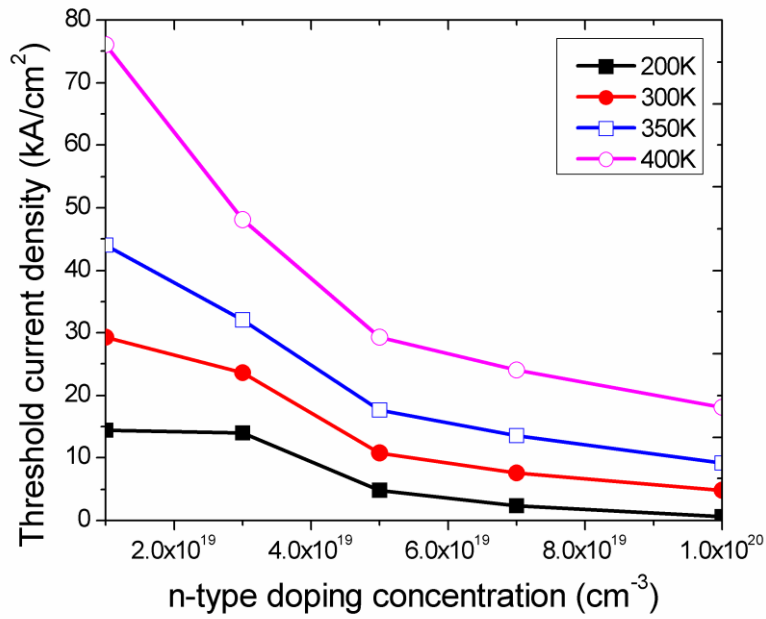


Figure 2.19 Theoretical estimation of the threshold current density for Ge with different n-type doping levels.

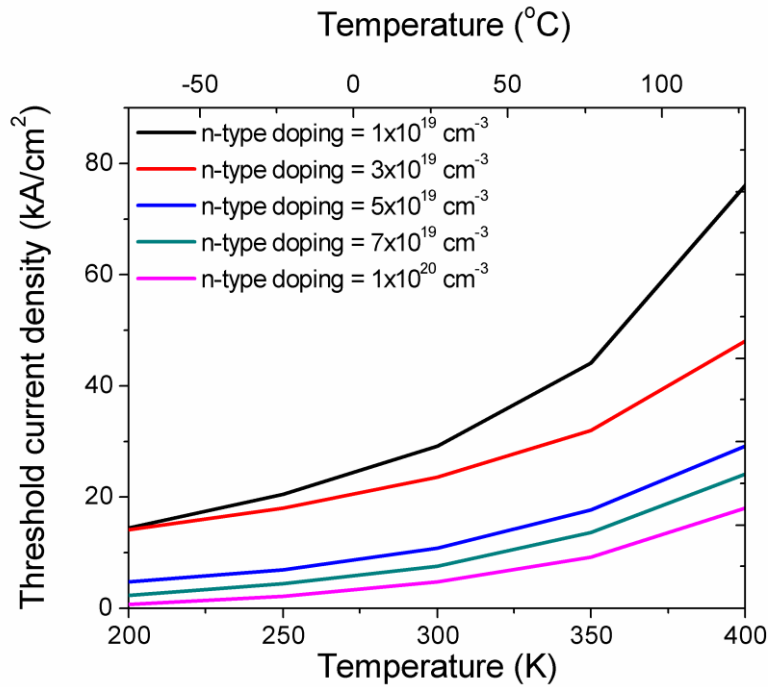


Figure 2.20 Laser threshold current densities with temperature ranging from 200 K to 450 K for Ge doped to different levels.

The overall temperature dependence can be quantified with the characteristic temperature T_0 , which is a commonly used parameter to measure the threshold current degradation speed with temperature in the equation of $J_{th} = J_0 e^{T/T_0}$ [110]. A large T_0 indicates that lasers are more temperature stable. Table 2.2 shows the extracted T_0 from Figure 2.21 for Ge lasers with different doping concentrations. The most temperature stable Ge laser has the doping concentration of $3 \times 10^{19} \text{ cm}^{-3}$. The slope of threshold current increase with temperature is close to flat around room temperature. The result is a trade-off between the electron thermalization from the L valleys to the Γ valley, non-radiative recombination and density of states reduction in all valleys. Compared to the common InP based lasers, which have a characteristic temperature of 50K~70K [110] around room temperature, Ge lasers have a better temperature stability performance with regard to the threshold current. For instance, the threshold current for the Ge laser doped to $3 \times 10^{19} \text{ cm}^{-3}$ has a two times higher characteristic temperature than III-V. The characteristic temperature T_0 for Ge laser devices with other doping concentrations are mostly higher than the InP based lasers except for the high doping concentrations, such as $1 \times 10^{20} \text{ cm}^{-3}$. When Ge is doped to above $7 \times 10^{19} \text{ cm}^{-3}$, the Ge laser will behave the same as the direct III-V laser, including the characteristic temperature. Although bulk Ge laser is predicted to have a high threshold current density, the temperature stability is better than the bulk III-V laser when Ge is doped to mid- 10^{19} cm^{-3} . This is one of the advantages to use the Ge laser as the light source for Si photonics. Depending on the device requirements, higher doping is beneficial for low threshold current and mid- 10^{19} cm^{-3} might be better for temperature stability.

Table 2.2 Characteristic temperature T_0 extracted from the calculated threshold current curves for Ge

Doping concentration (cm^{-3})	1×10^{19}	3×10^{19}	5×10^{19}	7×10^{19}	1×10^{20}
T_0 (K) @300K	101	152	103	87	72

Chapter Summary

In Section 2.1 and Section 2.2, based on the new knowledge on heavy n-type doping to Ge electronic band structure and free carrier absorption, we re-evaluate the optical gain modeling in Ge. The modified model successfully explains the broad lasing spectrum from 1520nm to 1670nm that we observed from our experiments because of the band gap narrowing effect. The predicted net materials gain can reach $\sim 1000 \text{ cm}^{-1}$ at the injection level of mid- 10^{19} cm^{-3} . The gain peak position shifts to shorter wavelength with higher injection. Since lasing happens when gain equals to optical loss, a device with a high optical loss requires a high materials gain. Therefore, the most possible lasing peak position will be at the shorter wavelength on the gain spectrum. The understanding of so called “gain clamping” explains the multiple emission wavelengths we observed in our electrically pumped Ge laser. Additionally, if Ge has a high tensile stain such as 1.8% or 2.5%, the gain bandwidth can extend to 2 μm or 3 μm , enabling the potential for Ge lasers in mid-IR sensing and imaging applications.

In Section 2.3 and Section 2.4, we study the PL with temperature in n-Ge. We conclude that the non-radiative recombination in our Ge is so significant that we need to consider it to explain the PL peak intensity drop with high temperature. A detailed PL calculation is presented with an emphasis of the SRH recombination mechanism with temperature and doping. Based on

the understanding and previous calculated gain spectrum, we can predict a theoretical threshold current density of $\sim 10 \text{ kA/cm}^2$ for Ge laser devices doped to mid- 10^{19} cm^{-3} at room temperature. The higher doping concentration in Ge can reduce the threshold current while moving the emission to longer wavelengths. The threshold current in Ge has a better temperature stability, especially when Ge is doped to $3 \times 10^{19} \text{ cm}^{-3}$, resulted from a trade-off between electron thermalization and non-radiative recombination. This will be one of the advantages of using the Ge laser compared to the III-V laser. Auger recombination for the heavily n-type doped Ge needs more understanding to be able to predict the threshold current density accurately.

Chapter 3

Ge Epitaxial Growth on Si and Planarization

In this chapter, we present the Ge epitaxial growth on Si substrate by ultra-high vacuum chemical vapor deposition (UHVCVD). A typical two-step growth method with a low temperature (LT) buffer and a high temperature (HT) high quality single crystal Ge is used. We use Ge trench growth in silicon oxide (SiO_2) trenches to achieve Ge sidewall passivation. Process development to get vertical oxide sidewalls in order to get good trench filling during growth is discussed. We also study the corner filling during the growth and T-shape trench growth is used to improve filling quality. Additionally, a Ge non-buffer growth method is discussed regarding to the trench width. Finally, chemical mechanical polishing (CMP) of Ge is presented in detail and a controllable and selectively CMP process is developed for Ge waveguides in oxide trenches.

3.1 Ge Epitaxy using UHVCVD

UHVCVD is one of the typical epitaxial growth tools for Si, Ge and also $\text{Si}_x\text{Ge}_{1-x}$ [111, 112]. The tool supplies one or more volatile precursors such as GeH_4 into a hot wall chamber. The precursors can decompose on the wafer surface under certain temperature through pyrolysis reaction. The non-volatile decomposed products such as Ge can grow on the wafer surface at certain growth rate while the volatile decomposed products such as H_2 desorb from the wafer surface.

The tool we use to grow our epitaxial Ge on Si is a Sirius 300 UHVCVD manufactured by Unaxis. It is a hot wall system, which means that the tube, the wafer carrier boat, and wafers are under the same high temperature during growth. The base pressure of the tube in idle mode is always around 1×10^{-8} mbar. At this high vacuum level, the contaminants can be kept at a very low level, especially water vapor and O_2 gas. Our UHVCVD is also equipped with a residual gas analyzer (RGA), a small mass spectrometer typically designed for process control and contamination monitoring. Table 3.1 shows a list of possible contamination chemical molecules and their partial pressure when the tube is in idle mode. All the contaminants show a low partial pressure in the tube while water vapor shows an order of magnitude higher pressure than the other contaminants. The major contaminant is water vapor and therefore, a high temperature bake and tube coating are very important maintenance steps to keep UHVCVD functioning.

Table 3.1 Partial pressure of contamination chemical molecules for UHVCVD tube in idle mode

Chemical molecules	H_2	O_2	H_2O	N_2
Partial pressure (Torr)	2.1×10^{-9}	1.0×10^{-9}	2.0×10^{-8}	1.6×10^{-9}

Besides of the excellent low impurity contamination, ultra high vacuum can help to prepare an oxygen free and hydrogen passivated Si wafer surface in assistance with a hydrofluoric (HF) acid dip and a high temperature (780 °C) hydrogen bake. Surface preparation is extremely important for epitaxial single crystal growth.

3.1.1 Two-step Ge Epitaxial Growth on Si

Ge has a lattice constant of 5.658 Å and Si has a lattice constant of 5.431 Å. This 4.2% lattice mismatch causes in the formation of misfit dislocation at the Si/Ge interface and threading dislocation inside Ge. If the hetero-epitaxial Ge is directly grown on the blanket Si substrate, islands will form when the Ge film exceeds the critical thickness. One way to grow high quality single crystalline Ge on Si is through a graded SiGe buffer which has a compositionally grading at high growth temperatures, such that the strain level in the structure is never high [113].

Our method is to use a two-step growth approach with LT Ge buffer and HT single crystalline Ge [26]. The Si wafer is first cleaned by a standard RCA cleaning step with an additional step of 30s ~ 60s 50:1 (H₂O:HF) HF dip. The HF dip as the last step of cleaning is essential to passivate the Si wafer surface with hydrogen and remove the native oxide. We then can place the Si wafer into the UHVCVD chamber within two hours after the RCA clean. The first step of growth is to bake the Si wafer in H₂ gas at 780 °C to further remove oxygen from the wafer surface and passivate with hydrogen. The second step is to cool the chamber down to a low temperature of 360 °C and flow GeH₄ as a precursor gas for LT Ge deposition through a pyrolysis reaction:



Normally a 40 nm ~ 60 nm Ge buffer is grown on Si wafer to prevent Ge islanding. When the epitaxial Ge thickness is larger than the critical thickness, the Ge film tends to release the increasing strain energy with thickness. However, the temperature is low enough so that the Ge atoms do not have adequate kinetic energy to move around to form islands. Therefore, the strain energy is released by misfit dislocations inside the buffer layer. Figure 3.1 is a plan view TEM image showing the misfit dislocations in the Ge buffer with a density above $1 \times 10^9 \text{ cm}^{-2}$. Once the buffer layer is thick enough and the strain energy is fully relaxed plastically by misfit dislocations, the temperature is normally raised to 650 °C ~ 780 °C for the Ge homo-epitaxial growth on the buffer layer. During Ge growth, the tube pressure is around several mTorr. The Ge growth rate on the Si (100) surface is about 6 ~ 10 nm/min depending on growth temperature and pressure.

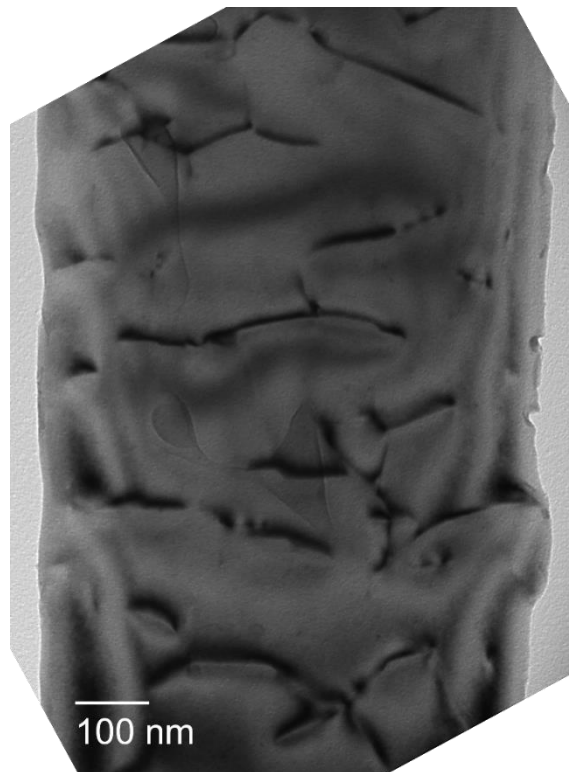


Figure 3.1 Plan view TEM image of misfit dislocations in the Ge buffer

In the as-grown blanket Ge film, the threading dislocation density is usually in the order of $10^8 \sim 10^9 \text{ cm}^{-2}$. Threading dislocations are often observed in lattice mismatched epilayers. The dislocation half-loops nucleated at the interface can propagate on (111) planes inclined to the interface, leaving a 60° misfit dislocation segment at the interface and two arms at the end extending up through the layer. However, these threading dislocations can act as defect centers for non-radiative recombination which will degrade the optical and electrical properties of Ge. They can also contribute to the leakage current as a shunt path, which has been clearly observed in Ge photodetectors [114]. Therefore, Ge films are normally annealed at a higher temperature such as 850°C to reduce threading dislocation density (TDD) for intrinsic Ge growth or cyclic annealing can be applied to get a better TDD reduction effect [26]. After annealing, TDD can be reduced to $\sim 2 \times 10^7 \text{ cm}^{-2}$ for $1 \mu\text{m}$ thick blanket Ge films and close to $1 \times 10^6 \text{ cm}^{-2}$ for $10 \mu\text{m} \times 10 \mu\text{m}$ Ge mesa structures due to size effects. However, the high temperature annealing will cause additional dopant loss for doped Ge films. The out-diffusion problem and doping method to achieve both high doping and low TDD will be discussed in the following paragraph.

The additional important benefit from the Ge high temperature anneal is that tensile strain can be induced into the Ge film. When the temperature is cooled down to room temperature, both the Ge film and the Si substrate will shrink. However, Ge shrinks more than Si due to a larger thermal expansion coefficient, so in-plane tensile strain is accumulated in the Ge layer upon cooling. This bi-axial tensile strain can be calculated by using the following expression:

$$\epsilon = \int_{T_0}^{T_1} (\alpha_{Ge} - \alpha_{Si}) dT \quad (3.2)$$

where T_0 and T_1 are room temperature and growth or annealing temperature, respectively. $\alpha_{Ge} = 5.9 \times 10^{-6} / \text{K}$ is the thermal expansion coefficient of Ge at room temperature. $\alpha_{Si} = 2.6 \times 10^{-6} / \text{K}$ is the thermal expansion coefficient of Si at room temperature. The tensile strain in blanket

Ge films is 0.2% ~ 0.25% at growth or annealing temperatures of 650 °C ~ 850 °C [115]. This amount of tensile strain will shrink the direct band gap of Ge to ~0.76 eV with an emission wavelength around 1600 nm at room temperature, confirmed by photoluminescence as shown before. This wavelength is ideal for making a Ge laser for Si photonics used in telecommunication applications.

3.1.2 Ge Selective Growth

Since Ge grows selectively only on Si, not on SiO₂, we can define the oxide window first and then grow Ge in the oxide trench. Selective epitaxial growth of Ge on Si is beneficial for several reasons. First is the flexibility to grow Ge in a defined area instead of the deposition of Ge on the entire wafers. The second is the lower threading dislocation density after annealing for Ge with smaller size. The threading dislocation reduction is due to annihilation through dislocation gliding and termination at the oxide/Ge interfaces. The third is the Ge sidewall passivation. An alternative way to pattern Ge is dry etching. However, the dry etching results in dangling bonds on the Ge sidewalls which need to be passivated. Instead, the selective grown Ge has a natural grown sidewall inside of oxide trench and therefore eliminates the problems induced by dry etch. Previous work on Ge PDs shows a reduction of dark current owing to the selective epitaxial growth [30, 116]. Therefore, we also use selective grown Ge waveguide on Si to fabricate laser devices.

3.1.2.1 Process development for Vertical Oxide Sidewall

For the growth wafer preparation, we first deposit or thermally grow a thin layer of oxide (200 nm ~ 500 nm) on a Si wafer. The deposited oxide by plasma enhanced chemical vapor deposition (PECVD) has to be annealed at high temperature such as 1000 °C to remove hydrogen for the following Ge growth. Then photolithography is applied to define the growth patterns and then dry etch the oxide using reactive ion etching (RIE) until leaving about 10 nm oxide at the bottom. The 10 nm oxide left is to prevent plasma damage to the Si surface which will interrupt the following Ge growth. Buffered oxide etch (BOE) is used to etch the remaining ~10 nm oxide. The combination of dry etch and wet etch results in a vertical oxide sidewall without damage to the Si surface. After that, oxygen plasma and piranha ($\text{H}_2\text{SO}_4:\text{H}_2\text{O}_2 = 3:1$) are used to remove the photoresist.

The vertical oxide sidewall is very important for trench filling. As discussed in Ref [117], if the oxide sidewall angle is less than 82.5° , the trench filling process is determined by the facet with the slowest growth, the (111) facet. If the oxide sidewall angle is larger than 82.5° , the trench filling process is then determined by the faster growing (311) facet. Therefore, a vertical sidewall helps to reduce the required growth time for trench filling.

We therefore developed both suitable photolithography and oxide etch processes to achieve vertical oxide sidewalls. A vertical photoresist sidewall is the prerequisite for a vertical oxide sidewall since the photoresist is the mask for the oxide etch. The following steps are the typical photolithography process we use:

- (1) Spin coat ~ 1 μm thick MEGAPOSIT SPR 700 as the positive photoresist on the oxide surface
- (2) Softbake at 90 °C for 1 min

- (3) Expose wafers using Nikon NSR2005i9 with an optimized exposure time and focus. The conditions work best for us are exposure time of 195 ms and focus of 0.5.
- (4) Post-exposure bake at 115 °C for 30s
- (5) Use MICROPOSIT MF-CD26 as the developer to clear the pattern
- (6) Hard bake at 120 °C for 30s

Beside finding the right exposure condition, another key process step for photoresist is the hard bake temperature. High temperature will cause the photoresist to reflow, resulting in a sloped sidewall. Figure 3.2 shows an example of the photoresist reflow with a hard bake temperature of 130 °C. Notice that the narrow photoresist strip has a higher sidewall angle of 71.8° than the large area of photoresist. Therefore, it will be more difficult to achieve vertical oxide sidewalls for larger spaced Ge waveguides.

We then use a lower temperature of 120 °C for the hard bake. The sidewall angle of the narrow photoresist strips is improved to 84.4° and the sidewall angle of wide photoresist strips is improved to 73°. Since the bake temperature cannot be too low as it will degrade the etch resistance of the photoresist, we use a shorter bake time of 30s instead of 1min.

After the photolithography is done, the wafer is transferred to an Applied Materials AME 5000 RIE chamber for oxide dry etching. A recipe of 18 sccm CHF₃, 36 sccm CF₄, 100 sccm Ar, 200 W power and 100 mTorr pressure is used. With this etch recipe, we can get an ~84.6° oxide angle for larger spaced trenches and almost 90° oxide angle for trenches spaced by 1 μm oxide, as shown in Figure 3.3. The successful development of photolithography and dry etching makes oxide patterned structures ready for growth.

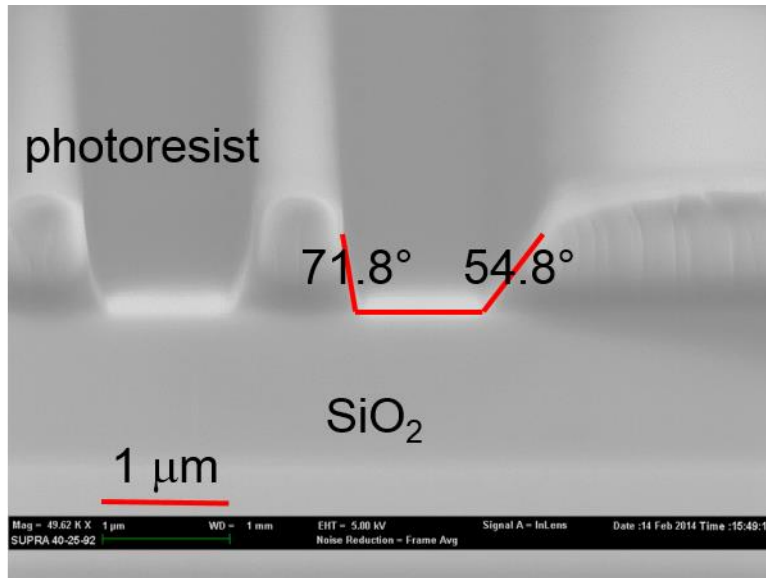
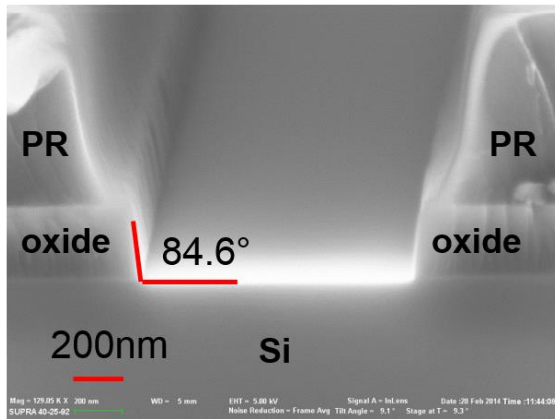


Figure 3.2 SEM image of the positive photoresist after hard baking at 130 °C for 1 min

(a) Device waveguides



(b) packed waveguides

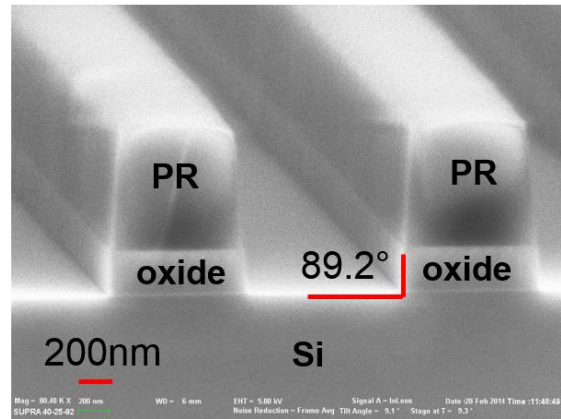


Figure 3.3 SEM images of oxide sidewall angles after dry etch for (a) device waveguides and (b) packed waveguides

3.1.2.2 Ge Trench Growth

When Ge grows in an oxide trench on a Si (100) surface with the trench aligned to the $\langle 011 \rangle$ directions, three growth facets have to mainly be considered, (111), (311) and (100) facets. As discussed previously, a (111) facet will appear if the sidewall angle is smaller than 82.5° while being suppressed if sidewall angle is larger than 82.5° . Figure 3.4 shows an example of selective grown Ge in a $\sim 1 \mu\text{m}$ wide oxide trench with a growth temperature of 650°C and growth pressure of 12 mTorr. Based on the Wulff construction [118], we can get growth rates of 2.4 nm/min for (100) facets, 1.18 nm/min for (311) facets and 0.7 nm/min for (111) facets. To fabricate a Ge device with uniform carrier injection, Ge over-growth with following chemical mechanical polishing (CMP) is required. In Figure 3.5, we present two surface morphologies for over-grown Ge: (a) is when Ge just fills the oxide trench with a roof-top structure and (b) is when Ge has over-grown significantly with a mushroom-like structure.

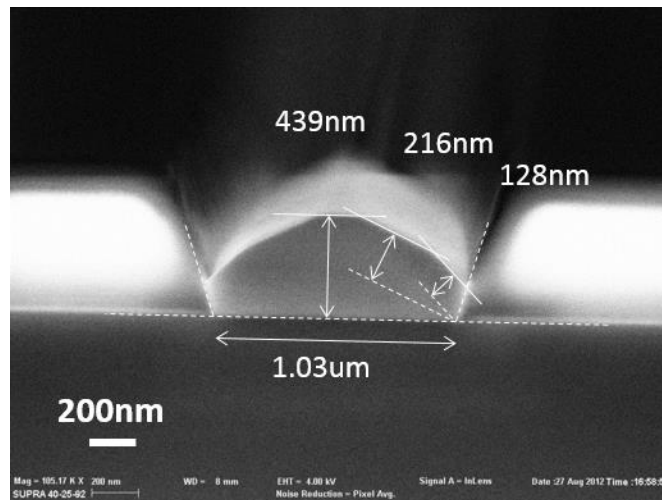


Figure 3.4 Cross sectional SEM image of a Ge waveguide selectively grown on Si

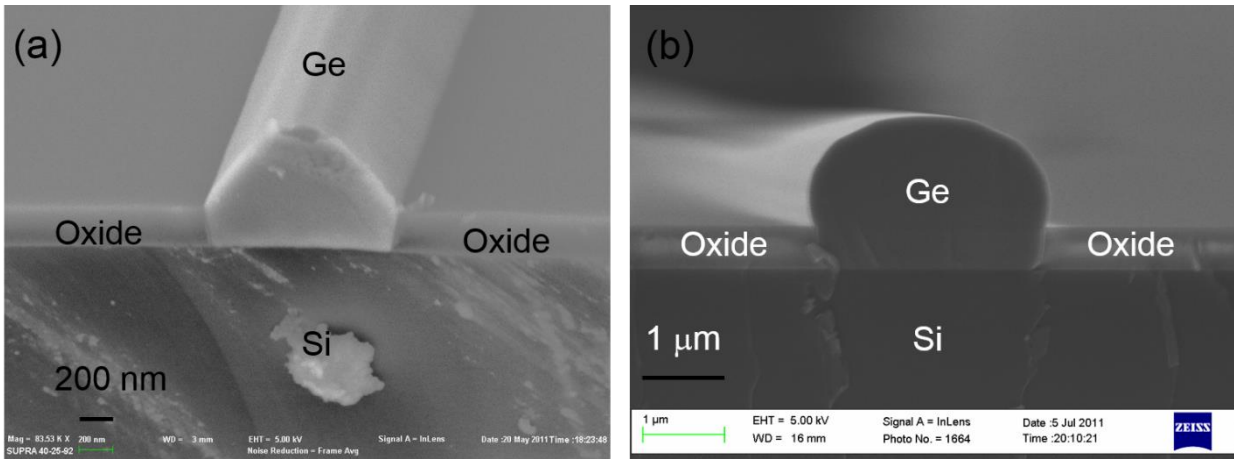


Figure 3.5 Cross sectional SEM images for over-grown Ge (a) roof-top structure (b) mushroom-like structure

Furthermore, we investigate the interface between the oxide sidewall and Ge by cross section transmission electron microscopy (TEM). The thermal expansion coefficient of Ge is $5.9 \times 10^{-6} / \text{K}$ and the value of SiO_2 is $5.6 \times 10^{-7} / \text{K}$. When the structure is cooled down from high temperature to room temperature, there might be a gap or crack between the oxide and the Ge if there is no good bonding since Ge has almost one order of larger thermal expansion coefficient than oxide. We can clearly see threading dislocations extending from the Ge/Si interface to the surface from Figure 3.6(a) because the film is an as-grown film without additional annealing. In the enlarged Figure 3.6(b), we can observe the Ge/Si interface more closely that there exists a thin layer of Ge buffer full of dislocations. When we zoom into the Ge/oxide interface in Figure 3.6(c), it is also obvious that Ge and oxide has a very good contact without any gaps or cracks even when the scale bar of the image is as small as 5 nm. Therefore, we can conclude that trench grown Ge has a natural oxide passivation at the sidewall from the microscopy view and it will eliminate the leakage current path through the sidewalls. Furthermore, since Ge has a larger thermal expansion coefficient than oxide, Ge surrounded by oxide may have higher tensile strain

compared to a Ge thin film on Si. This is only a hypothesis which needs further experiments for confirmation.

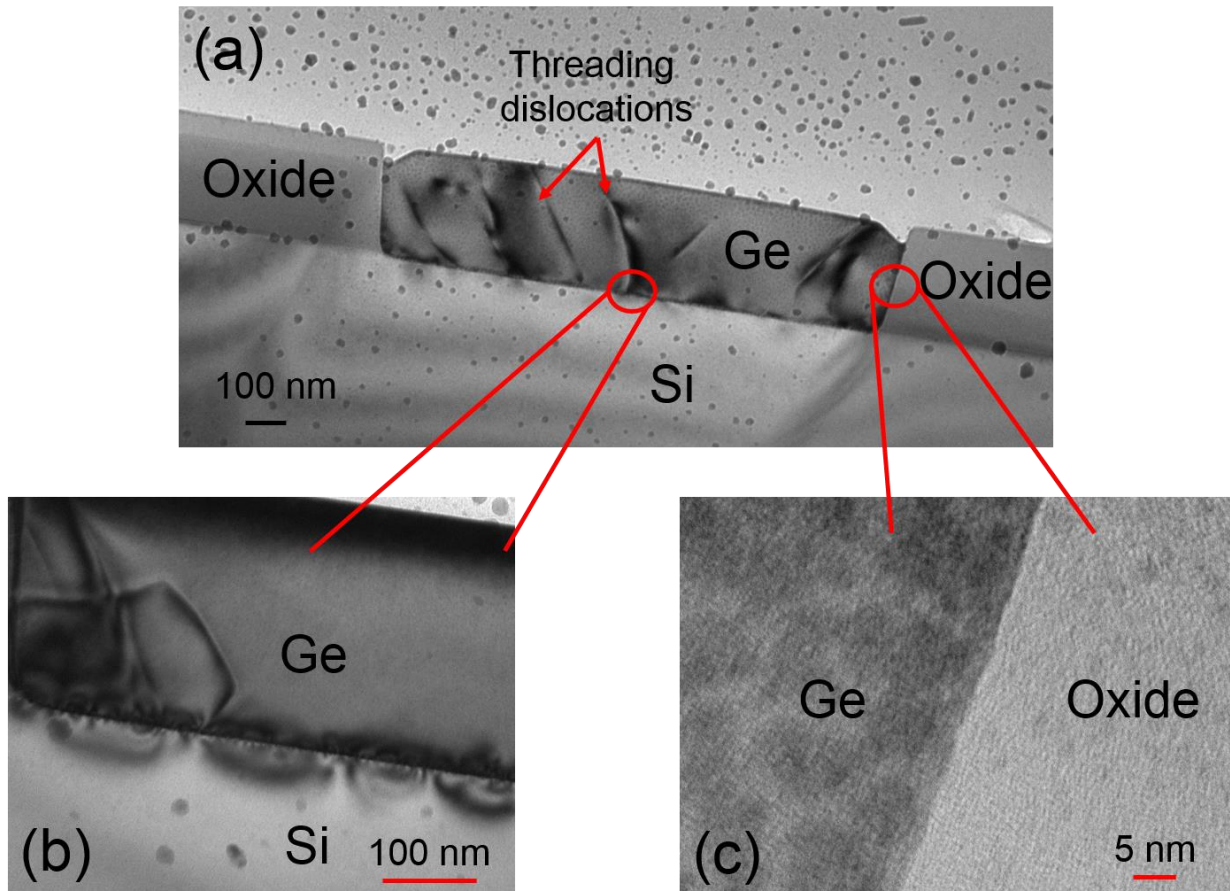


Figure 3.6 Cross sectional TEM images for Ge waveguide grown in oxide trench (a) overview image (b) enlarged image of Ge/Si interface (c) enlarged image of Ge/oxide interface

3.1.2.3 Ge Growth at Corners

Ge growth at the waveguide end also attracts our attention because the waveguide end is acting as one mirror with Ge/oxide interface for the Fabry-Perot cavity laser or as a coupling connection between the Ge active region and the silicon waveguide in an external cavity Ge laser.

The external cavity laser design will be discussed in detail in the following chapter. The growth problem comes from the rounded corners after photolithography as show in Figure 3.7. While we are developing vertical oxide sidewall for Ge trench filling in Section 3.1.2.1, we purposely over-exposure the photoresist and therefore, the sharper features such as corners in a pattern are the first to be attacked during development, resulting in rounded corners. Similarly, if the corners are under-exposed, the corners will receive slightly less light than the center of the pattern and then will not be clear during the development process. The under-exposure will also result in rounded corners. It is very difficult to get rid of the rounded corners through a simple photolithography process development.

The Ge growth rate in the rounded corners is reduced due to the facet growth from three directions. From Figure 3.8, we observe multiple facets at the end of the Ge waveguides. Optical simulation results show a reduction of $\sim 5\%$ for the Ge/oxide interface reflectivity with the rounded corner effect. Additionally, it might be very difficult for Ge to completely fill the corner if a further chemical mechanical polishing (CMP) step is required.

To solve the rounded corner problem, we purposely design a T shape opening at the waveguide end with $1\ \mu\text{m}$ width. The reason is to create a vertical and flat Ge/oxide interface by the method of pushing rounded corners away from optical mode center. Figure 3.9 shows the Ge growth in the T-shape waveguide end with a successful corner filling. We need a further CMP which will be discussed in detail later to planarize the over-grown Ge.

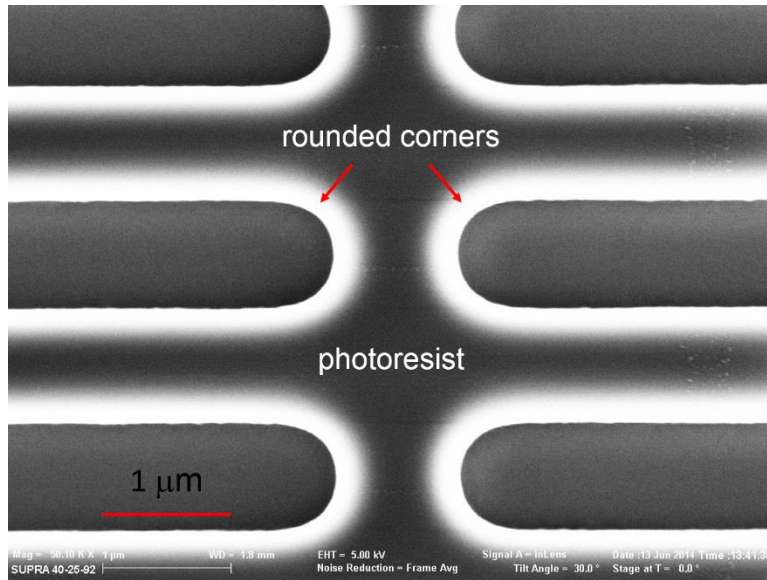


Figure 3.7 Photoresist after exposure and development showing rounded corners at the resist ends

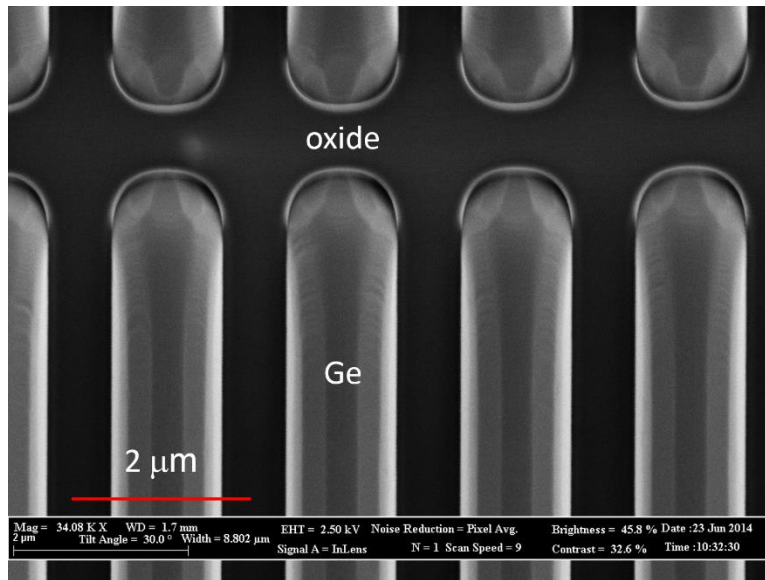


Figure 3.8 Selective Ge growth in rounded corners

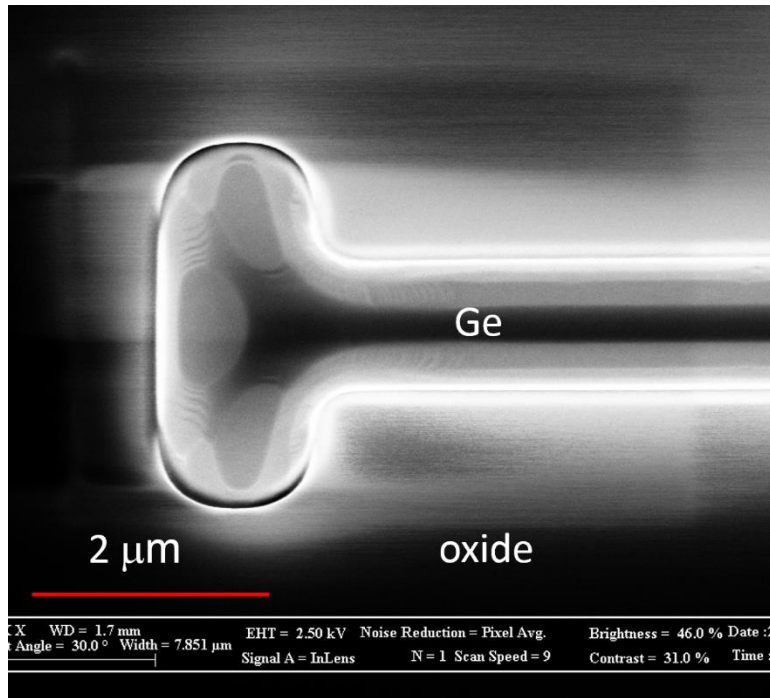


Figure 3.9 Ge selective growth in a T-shape corner

3.1.3 Ge Bufferless Growth

A 40 nm – 60 nm Ge buffer is commonly used to accommodate the 4.2% lattice mismatch between Ge and Si for an epitaxial Ge growth on a Si substrate. However, as stated by Camacho et al. [119], the buffer layer can act as both a dopant sink for highly n-type doping and recombination centers for injected carriers due to its high dislocation density. Single crystalline epi-Ge on Si without buffer is highly desirable. Our previous results show that Ge is able to grow epitaxially on Si without buffer with the assistance of phosphorus as surfactant and a small trench opening for growth. The threading dislocation density in bufferless grown Ge is as high as $6 \times 10^8 \text{ cm}^{-2}$ without high temperature anneal. In this paragraph, we will study the trench opening effect more closely and also we will examine the threading dislocation density in the annealed Ge with bufferless growth to see if it is suitable for photonic devices.

We start with a blanket Si wafer and grow 300 nm oxide by thermal oxidation. A dry oxide etch with the recipe described previously is used to create different oxide trench openings from 500 nm to 10 μm followed by a short buffered oxide etch. The oxide patterned wafer is then cleaned by Piranha and RCA as the cleaning preparation for growth. A final 30 s diluted HF ($\text{HF}:\text{H}_2\text{O} = 1:50$) etch is important to passivate the Si surface with hydrogen. We use the UHVCVD tool mentioned previously for the bufferless growth. The detailed growth recipe is as follows:

- (1) Bake the wafer with 5.2 sccm H_2 at 780 $^\circ\text{C}$ to create an oxygen free Si surface;
- (2) Cool the chamber temperature to 650 $^\circ\text{C}$. Flow 3.8 sccm GeH_4 and 12 sccm PH_3 with a pressure of 10~20 mTorr. Ge is grown selectively on Si without buffer;
- (3) Raise the chamber temperature to 850 $^\circ\text{C}$ and anneal the as-grown Ge for 40 min.

Figure 3.10 shows SEM cross sections for Ge waveguides with different widths by bufferless growth. It is very clear that when the Ge width is equal to or smaller than 2250 nm, Ge shows a faceted growth of (100) and (311) indicating single crystal growth. However, the faceted surfaces are not as smooth as for selectively grown Ge with buffer in Figure 3.5. When the Ge waveguide width is 5250 nm, the (100) facet is not very obvious while the (311) facets are visible. When the waveguide is 10250 nm wide, wavy features appear on the (100) facet indicating island growth while the (311) facets are still existing. We can conclude from the growth trend that a smaller oxide trench opening prevents island formation and the island size is probably between 5 to 10 μm at the growth temperature of 650 $^\circ\text{C}$. We also check the bufferless growth for the waveguide along the direction of 45 $^\circ$ to the wafer flat (Figure 3.11). It also shows a single crystalline faceted growth.

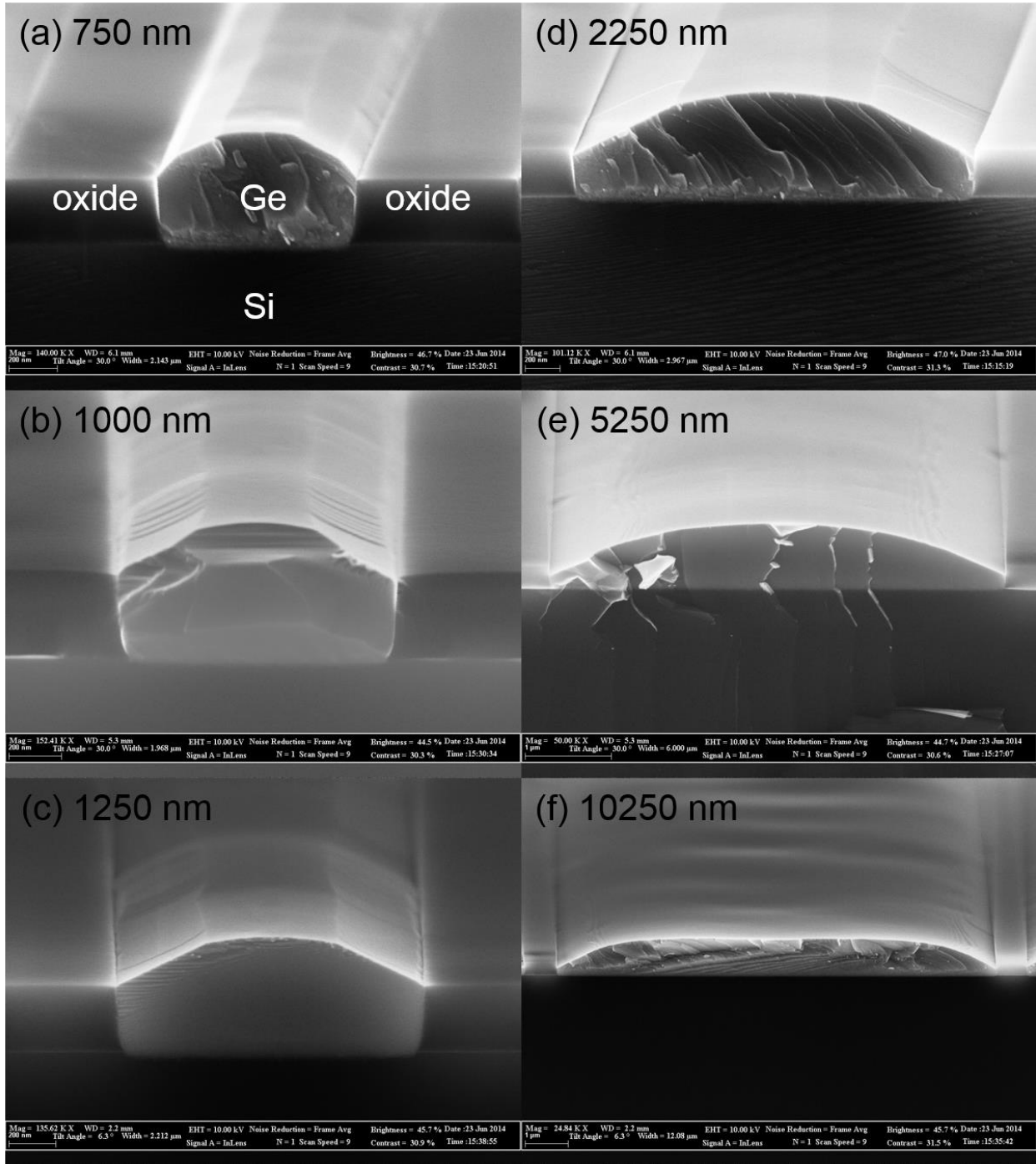


Figure 3.10 SEM of Ge by bufferless growth in different oxide trench widths of 750 nm, 1000 nm, 1250 nm, 2250 nm, 5250 nm and 10250 nm

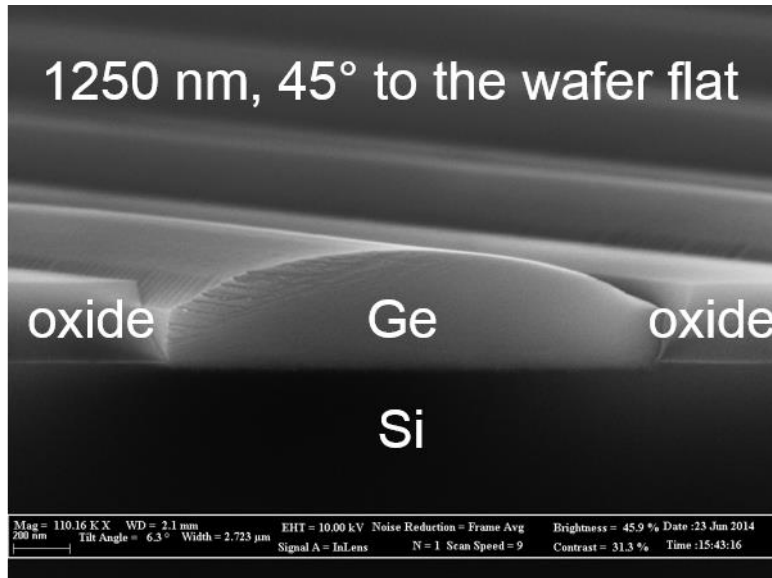


Figure 3.11 SEM of Ge by bufferless growth with 1250 nm oxide trench width and the waveguide is along the direction of 45° to the $[110]$ wafer flat

Figure 3.12 compares the Ge/Si interfaces for the buffered growth (Figure 3.12a) and the bufferless growth (Figure 3.12b). Both of the Ge waveguides have been annealed at 850°C for 40 min after the Ge growth. In the buffered growth Ge, we can observe a ~ 60 nm buffer layer full of defects such as dislocations, stacking faults and twins, with at most one 54.74° threading dislocation extending to the Ge film. In the bufferless growth Ge, we observe dislocations at the Ge/Si interface but not a layer of defects as in the buffered growth. This indicates that the bufferless growth can eliminate the dislocated buffer layer. However, we always observe two or more threading dislocations extending to the Ge film and some of the dislocations are not on the (111) plane. Without a buffer layer to confine most of the threading dislocations and to release the strain energy, the misfit dislocations at the Si/Ge interface might lead to the formation of threading dislocations in the bufferless Ge more easily. From the multiple cross section TEM images of the buffered and bufferless grown Ge, we conclude that the threading dislocation

density is about three times higher in the bufferless grown Ge compared to the buffered grown Ge.

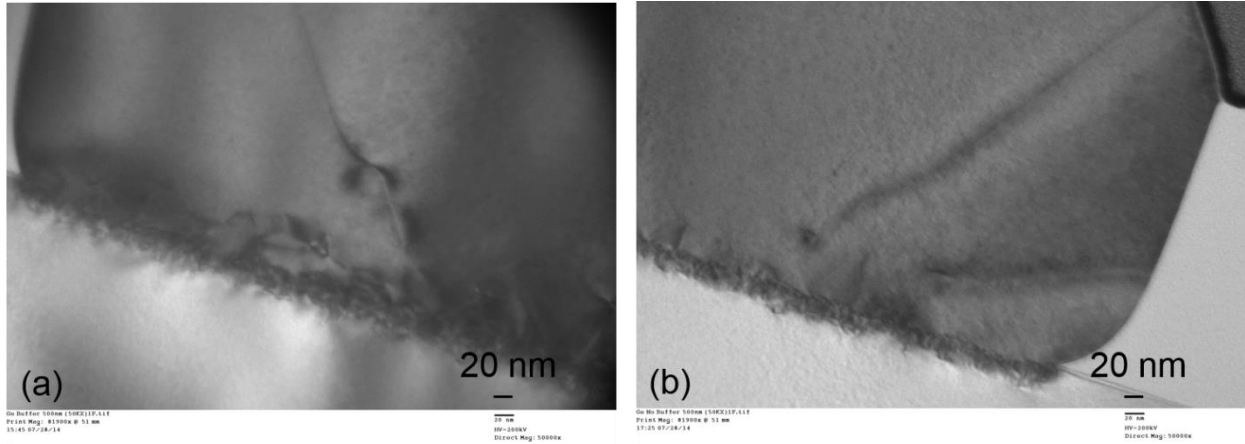


Figure 3.12 Cross sectional TEM images of 500 nm wide Ge waveguides (a) buffered growth (b) bufferless growth

3.2 Chemical Mechanical Polishing of Ge

During the selective epitaxial growth process, Ge facets are formed because of the different growth rates for different crystal planes as discussed previously [120]. Planarization of the Ge waveguides is important for further processing steps. Specifically in Ge laser devices, delta-doped layers are used as a dopant source and the layers have to be removed after dopant diffusion to prevent optical losses [121].

A common method for Ge planarization is chemical mechanical polishing (CMP) [122]. Hydrick et al. [123] found that 0.16% of H_2O_2 added to a conventional silica CMP slurry can polish Ge and SiO_2 simultaneously to achieve minimal dishing of Ge. Peddeti et al. [124] pointed out that the Ge dissolution rate (DR) has to be close to 0 nm/min to avoid dishing. The use of

low pH slurry is preferred because the Ge DR increases with pH value. A Ge CMP mechanism is proposed based on the observation that H_2O_2 oxidizes Ge into GeO_2 which is easier to dissolve in a higher pH solution [124]. The removal rate ratio of Ge to SiO_2 in a mixture slurry of fumed silica and 0.5 wt.% H_2O_2 at pH=2 is close to 1:1 and this slurry gives a reasonable good dishing control of ~15 nm [125]. The dishing is also lower than that from the slurry proposed by Matovu et al. [126] with the same patterned wafer used for the H_2O_2 based slurry reported in Ref. [125]. All previous work on Ge CMP focused on Ge shallow trench isolation structures with a high pattern density with 170 nm wide Ge and 230 nm wide oxide structures. For photonic applications, Ge is usually in a waveguide configuration with the width in the μm range, and the Ge waveguides have to be separated from each other at least several μm to avoid mode overlap and cross talk. Furthermore, the CMP selectivity of Ge to oxide is also crucial to prevent exposing devices or structures below the oxide. Pattern density is known to greatly affect the CMP rate and dishing in metal CMP. Therefore, we studied Ge CMP with various pattern densities using commercial CMP slurries diluted by DI water and mixed with H_2O_2 . The CMP details, performance and pattern density impact are described in the following.

3.2.1 Experiments Details

Epitaxial Ge was selectively grown in oxide trenches on a Si (100) wafer by UHVCVD, as described previously. The patterned wafers had trenches etched into thermally-grown 300nm-thick SiO_2 to expose the underlying Si. These trenches were all $1\mu\text{m}$ wide and spaced between $1\mu\text{m}$ and $280\mu\text{m}$ apart. Ge was overgrown to 300 nm to 1000 nm above the oxide surface. The 6 inch wafers were polished on a GNP POLI-400L polisher. The process conditions for polishing

were: applied pressure of 1 psi, slurry flow rate of 75 ml/min and a carrier/platen rotational speed of 87/93 rpm on an IC 1000 pad. The CMP process consisted of 10 seconds ramp-up, a polishing step with varying polishing times and a 10 second ramp-down and rinse step with in-situ pad conditioning. The pad was conditioned for 300s before each polishing. The CMP slurry consisted of commercial CMP slurries from Cabot Microelectronic Corp., W2000 and G1000, 0 to 1 wt. % H₂O₂ and DI water. The slurry pH value was around 3 for all CMP experiments.

A high resolution SEM (Zeiss Supra-40) was used to inspect the top view and cross section of the wafer before and after polishing. Figure 3.13 shows an example Ge waveguide with an overgrowth of 330 nm before CMP. Due to faceting of Ge during growth and oxide sidewall angles $<82.5^\circ$, the oxide trenches are not completely filled exhibiting grooves at the sidewalls. An atomic force microscope (AFM, Veeco Dimension 3100) was used to precisely measure the step height before and after polishing. Root mean square (RMS) roughness was also analyzed from the AFM graphs with a general measurement area of $0.5\mu\text{m} \times 2\mu\text{m}$. A UV-1280 spectroscopic ellipsometer was used to monitor the oxide loss before and after polishing.

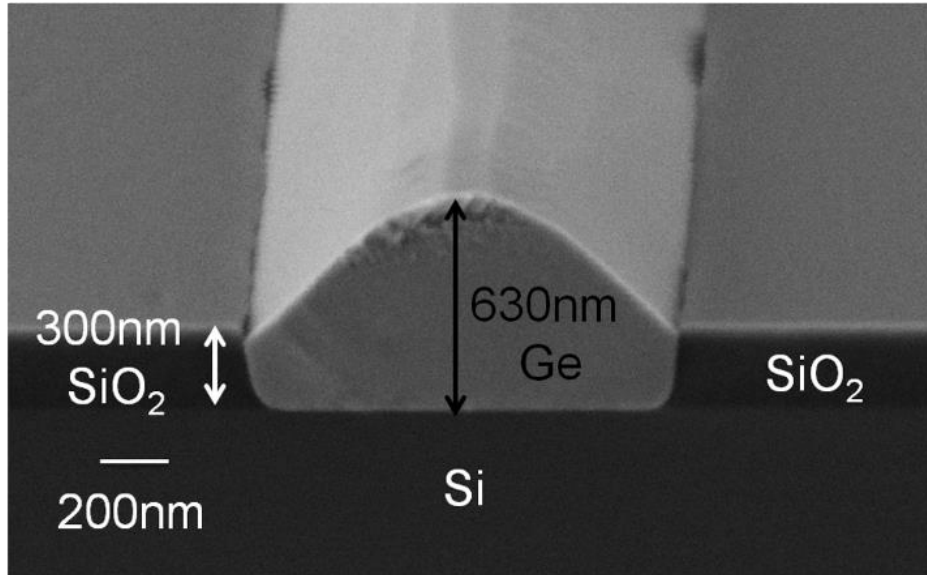


Figure 3.13 SEM cross section of a 1 μm wide Ge waveguide grown in the oxide trench on Si substrate

3.2.2 Ge Removal Rate with Slurry Composition

Since the thickness of the Ge overgrowth is between 300 nm and 1000 nm, a reasonable Ge removal rate has to be selected such that the polishing time can be well controlled in order to avoid over-polishing. We vary the abrasive concentration by diluting with DI water and H_2O_2 to adjust the Ge CMP rate. For this part of the study we used the slurry W2000, provided by Cabot Microelectronics. Table 3.2 summarizes the removal rate for 1 μm Ge waveguides separated by 1 μm oxide when varying the dilution ratio and H_2O_2 concentration. The slurry mixture with 1wt. % H_2O_2 and 1:1 DI water dilution (W2000-A) results in a removal rate of 380 nm/min within 45s polishing time which is too fast for reliable CMP time control to avoid over-polishing. The CMP removal rate is still as high as 370 nm/min within 90s polishing time with a lower H_2O_2 concentration of 0.5 wt. % (W2000-B). We then find that the CMP removal rate effectively

decreases to 190 nm/min within 60s polishing time with 1:3 DI water dilution (W2000-C) which corresponds to a lower abrasive concentration while the pH value increases from 2.8 to 3.1. In Table 3.2, we also present the slurry G1000 mixture with 1 wt. % H₂O₂ and 1:1 DI water dilution with a Ge dissolution rate of a ten orders of magnitude lower than the W2000 based slurry. We will discuss the G1000 slurry in detail later to minimize the Ge dishing during over-polishing.

Table 3.2 CMP removal rate for 1 μm Ge waveguides separated by 1 μm oxide, Ge dissolution rate and oxide removal rate with different slurry compositions

	Commercial slurry	DI water dilution	H ₂ O ₂ concentration (wt.%)	Ge removal rate (nm/min)	Dissolution rate (nm/min)	Oxide removal rate (nm/min)
W2000-A	W2000	1:1	1.0	384 \pm 16	34 \pm 2	1.6 \pm 2.8
W2000-B	W2000	1:1	0.5	370 \pm 11	25 \pm 2	0.5 \pm 2.0
W2000-C	W2000	1:3	1.0	188 \pm 14	25 \pm 2	0.6 \pm 1.6
G1000	G1000	1:1	1.0	164 \pm 15	2.5 \pm 2	1.7 \pm 1.7

We studied the Ge dissolution rate in slurries with adjusted pH value by measuring the Ge thickness before and after chemical etching. The pH value is adjusted by adding ammonium hydroxide or a pH buffer solution. As shown in Figure 3.14, for slurry W2000-C, the Ge dissolution rate is about 25 nm/min for a slurry pH of 3 to 6.5. The chemical etch time is 6min, 2min, 1min, 45s, 30s for pH = 3.1, 6.5, 9, 10, 11.5, respectively. The Ge dissolution in CMP slurries is a linear process confirmed by the dissolution test with varying etching time. The slurry

pH is adjusted by adding ammonium hydroxide or a buffer solution. A cross section SEM is taken to determine the Ge film thickness before and after etching in the slurries with various pH values. The error is calculated by the error propagation rule with the estimated ± 5 nm variation of film thickness and ± 2 s variation of etch time. The dissolution rate is more than ten times larger when the slurry pH is above 9. The high dissolution rate in the CMP slurry will result in increased Ge removal during over-polishing. Therefore, we choose to use the slurry with 1 wt.% H_2O_2 , 1:3 DI water dilution and a pH value of ~ 3 to achieve a relatively slow removal rate for better CMP time control and a low dissolution rate to avoid severe dishing and Ge erosion.

An oxide wafer was polished under the same CMP conditions and the oxide removal rate, monitored by ellipsometry, is minimal. As shown in Table 3.1, all three W2000 based slurries shows oxide removal rate of smaller than 2 nm/min. Therefore, the slurry we use for Ge CMP has a high selectivity to oxide to avoid oxide erosion.

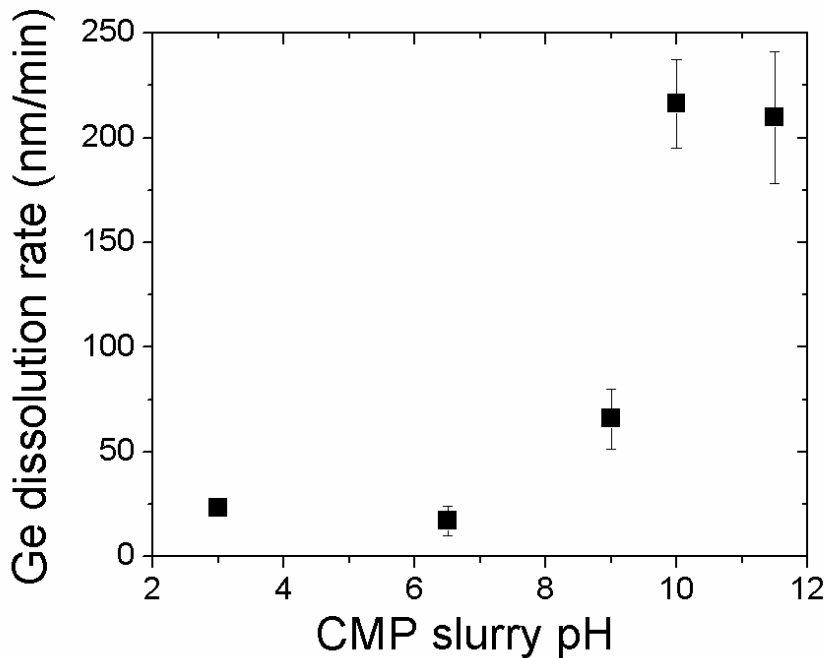


Figure 3.14 Ge dissolution rate change with slurry pH values using W2000-C

3.2.3 Ge Removal Rate with Pattern Density

We have fabricated $1\mu\text{m}$ wide Ge waveguides with different oxide spacing, resulting in varying pattern densities. Figure 3.15 shows the removal rate variation with pattern density for CMP slurries W2000-B and W2000-C, listed in Table 3.2. All Ge waveguides are $1\mu\text{m}$ wide with a length of 5 mm. The removal rate is calculated by the step height difference from AFM before and after polishing. The Ge removal rate of W2000-B is higher than of W2000-C due to the higher abrasive concentration. Both slurries show the same trend indicating that the removal rate decreases as the pattern density increases.

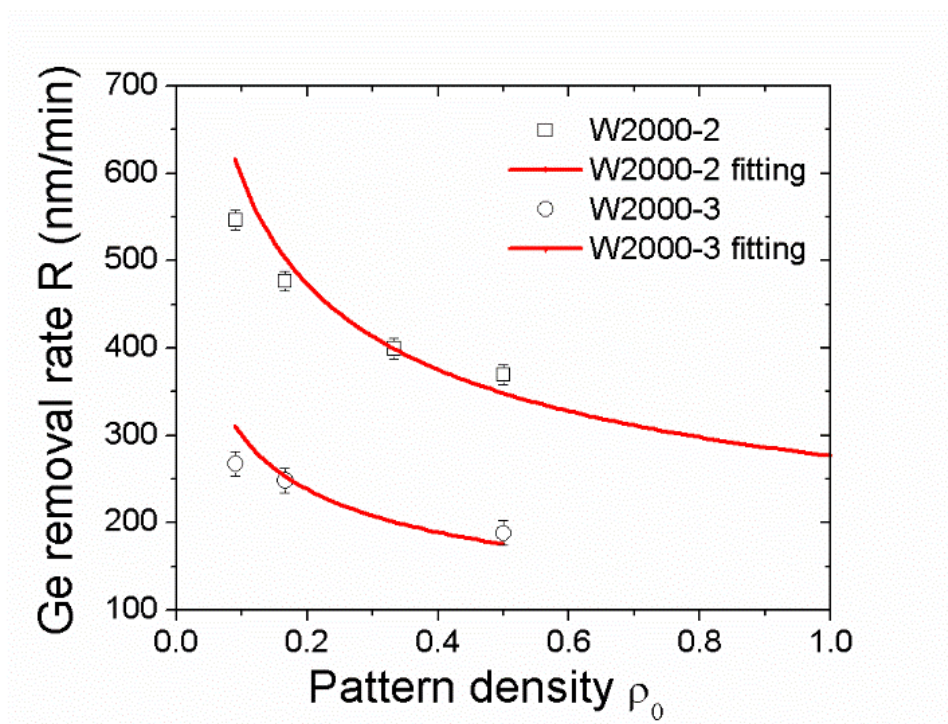
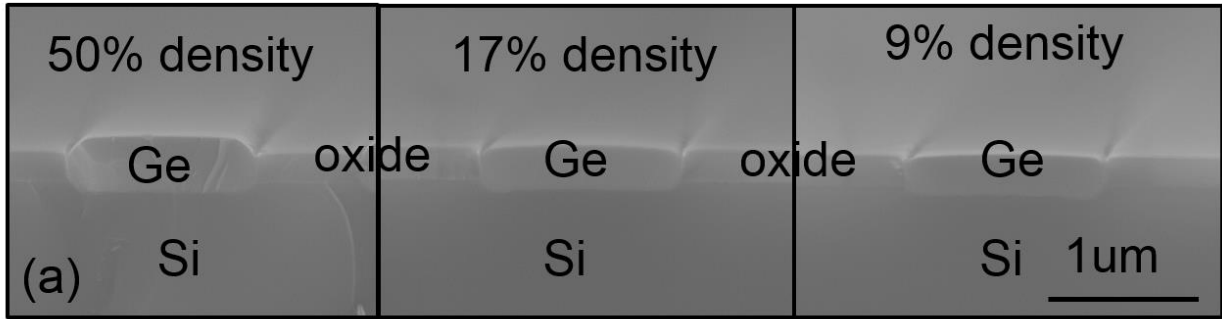


Figure 3.15 Ge removal rate variation with pattern density for CMP Slurry W2000-B and W2000-C. Solid lines are simulation results

As pattern density increases, the effective contact area between pad and wafer increases and therefore the effective local pressure decreases, resulting in a removal rate reduction. The above explanation can be generally represented by Preston's equation, $R = k_p p v$, where k_p is the "Preston coefficient", R is the material removal rate, p is pressure and v is the velocity of the platen relative to the wafer carrier. However, previous research also shows that the removal rate with pressure may follow a power law [127]. Cross section SEM images (Figure 3.16a) and the corresponding step height profiles (Figure 3.16b) measured by AFM confirm the removal rate trend with pattern density as shown for pattern densities of 50%, 17%, and 9% from the same wafer. The cross section SEM images show a very flat and uniform surface across the waveguide with less than 20nm deep grooves at the Ge/oxide interface due to the $<82.5^\circ$ oxide sidewall angle mentioned earlier.



(b)

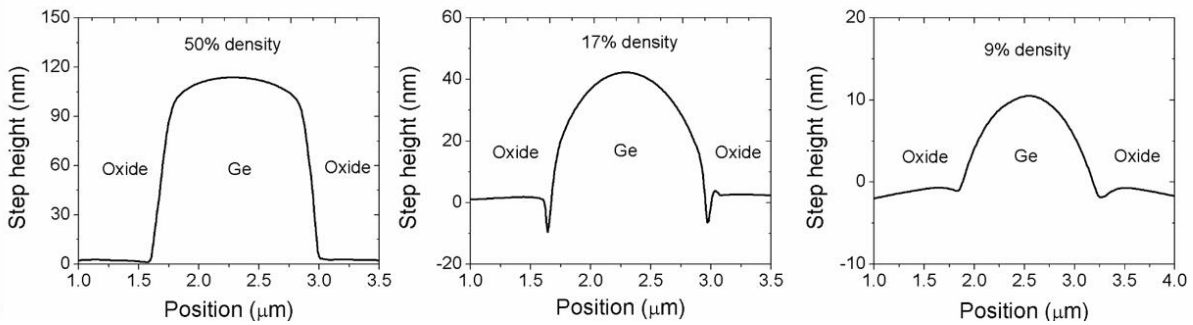


Figure 3.16 (a) Cross sectional SEM graphs for Ge waveguides with various pattern densities after CMP for 80s using slurry W2000-C. (b) The corresponding step height profiles for each pattern density measured by AFM

As we see in Figure 3.13, due to the protrusion shape of the over-grown Ge, the contact area between the platen and wafer increases with CMP time which means the effective pressure and Ge removal rate will also change with time. In order to predict the final Ge thickness and effective Ge removal rate in a patterned wafer, we used a model proposed by Stine et al. [128] with the additional considerations that the removal rate is proportional to the square root of pressure and pattern density changes with polishing time based on our specific waveguides shape. Since the slurry W2000-C has a low abrasive concentration, the assumption of a square root relationship between the removal rate and pressure is reasonable. The Ge removal rate can be formulated as follows:

$$\frac{dz}{dt} = k_p \sqrt{\rho} v = -\frac{K}{\sqrt{\rho(x,y,z)}}, \quad (3.3)$$

where K is the blanket polishing rate and $\rho(x, y, z)$ is the effective pattern density as a function of time. The above equation can be solved by assuming the pattern density linearly increases with polishing time as follows:

$$\rho(x, y, z) = \rho_0 \left(1 - \frac{z}{z_0}\right), \quad z > 0 \quad (3.4)$$

where $\rho_0 = a/(a + b)$ is the pattern density, a is the waveguide width ($1 \mu\text{m}$), b is the oxide spacing, z_0 is the imaginary Ge height assuming that the overgrown Ge has a triangular shape and z_1 is the overgrown Ge height before polishing (Figure 3.17). Then the final Ge thickness z and effective Ge remove removal rate R have the following expressions:

$$z = z_0 - z_0 \left(\frac{3Kt}{2z_0\sqrt{\rho_0}} + \left(1 - \frac{z_1}{z_0}\right)^2 \right)^{\frac{2}{3}} \quad (3.5)$$

$$R = \frac{z_1 - z_0}{t} + \frac{z_0}{t} \left(\frac{3Kt}{2z_0\sqrt{\rho_0}} + \left(1 - \frac{z_1}{z_0}\right)^2 \right)^{\frac{2}{3}} \quad (3.6)$$

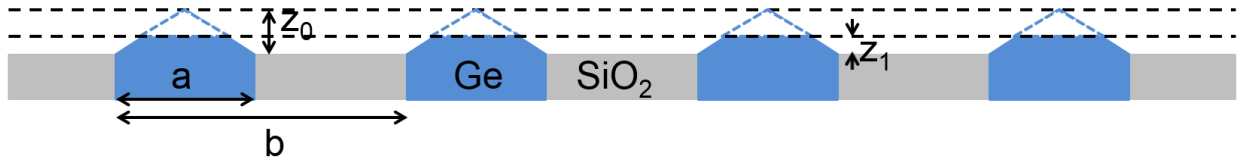


Figure 3.17 Schematic graph of the Ge selective growth geometries before CMP for simulation

The simulation results are presented in Figure 3.15 with a blanket polishing rate $K = 115$ nm/min for slurry W2000-B and 60 nm/min as the fitting parameters for slurry W2000-C. We also assume overgrown Ge has a triangular shape and thus $z_1 = z_0$. Since this model always assumes facet growth, it is not applicable for blanket Ge films. This explains why the Ge

removal rate at a pattern density of 1 in Figure 3.15 is larger than the removal rate of a blanket film, a value that we use as a constant in the Equation 3.3.

3.2.4 Waveguide Characterization after CMP

Considering the possible mode overlap with high pattern density in optoelectronic applications, we choose to achieve the planarization of 1 μm wide Ge waveguides with a 10 μm oxide spacing. The Ge removal rate is ~ 267 nm/min using W2000-C as described in Figure 3.15. Figure 3.18a shows the 2D profiles after polishing with 1 wt. % H_2O_2 and 1:3 DI water dilution at $\text{pH} = 3.1$ for 60s and 80s starting with the profile “before CMP”. The first 60s polishing is used to estimate the Ge removal rate under this CMP condition and the next 20s polishing using the same wafer planarizes the Ge waveguides with 10 μm oxide spacing based on the estimated removal rate. After an additional 20s polishing, the Ge is nearly planar with the oxide, extending only ~ 10 nm above the oxide and not showing any dishing. The step height variation is in an acceptable range for further fabrication. The polished Ge waveguides are inspected using SEM in top view (Figure 3.18b) and cross section (Figure 3.18c). No waveguides or parts of waveguides were unintentionally removed during the CMP process. We rarely observe scratch defects on the waveguide surface. The waveguide edge looks rough from the top view due to the roughness of the oxide sidewalls during dry etching, indicating that the roughness is not caused by edge degradation due to CMP. The grooves at the edge of Ge waveguide (Figure 3.18c) are due to incomplete Ge trench filling after growth. Figure 3.18d shows an AFM image of the Ge waveguide. The RMS roughness of the surface after 80s polishing is ~ 0.2 nm which is very desirable. Using W2000-C for polishing, we can achieve a flat surface with small roughness and

minimal scratch defects owing to the relatively slow Ge removal rate and thus good CMP time control for Ge waveguides with high pattern density. The slurry also works for blanket films, delivering a surface roughness around 0.1nm.

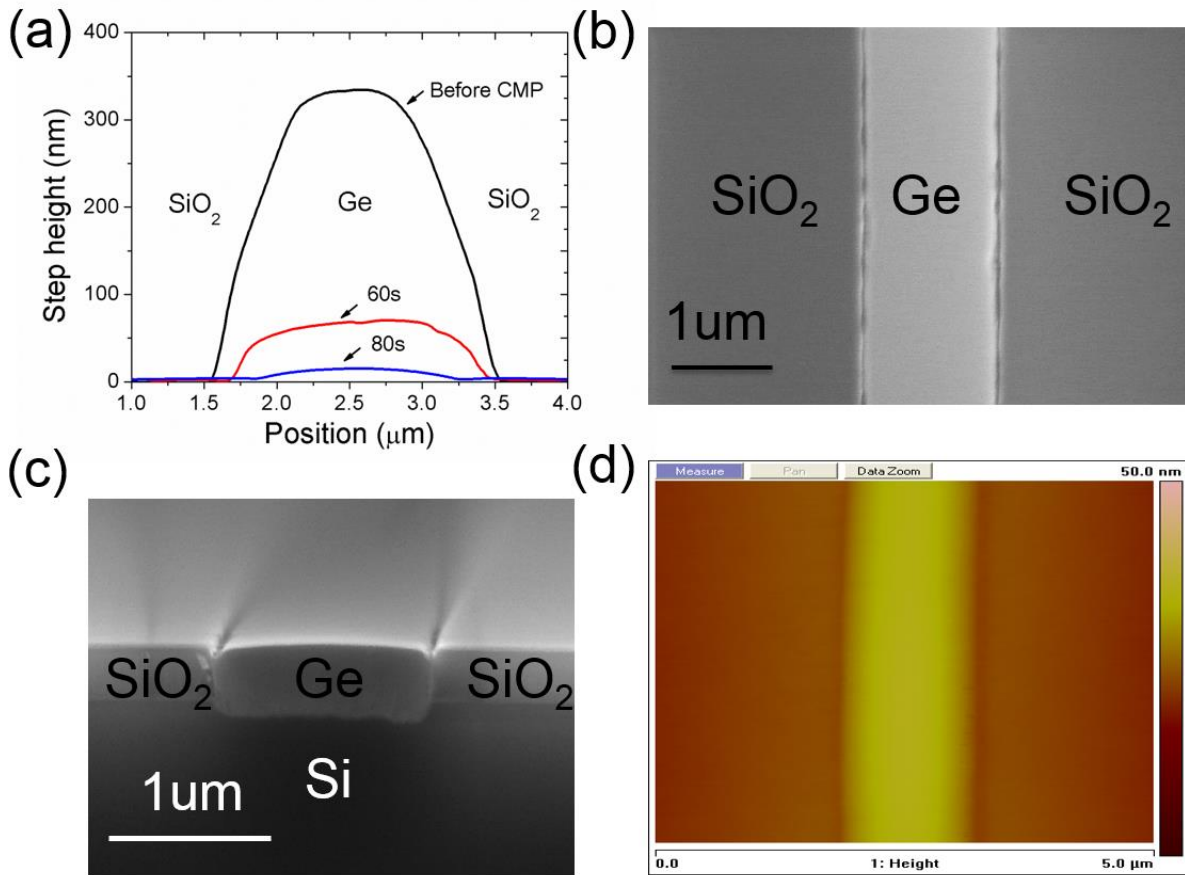


Figure 3.18 (a) 2D profile of a 1 μm wide waveguide spaced by 10 μm oxide before CMP, after CMP for 60s and 80s using slurry W2000-C. (b) Top view SEM image of the waveguide. (c) Cross sectional SEM image of the waveguide. (d) AFM image of the waveguide

3.2.5 CMP for Ge Waveguides with Extremely Low Pattern Density

Using CMP slurry W2000's composition optimization and process control, we have shown the planarization of Ge waveguides with 10 μm oxide spacing in Figure 3.18. The slower CMP removal rate with smaller oxide spacing indicates that the CMP process will also be controllable for those waveguides. However, device waveguides, separated by 280 μm oxide, suffer severe dishing during over-polishing. In Figure 19(a), the device waveguide shows 25nm dishing after 60s CMP using W2000-C and 45nm dishing after an additional 20s polishing for the same wafer. We attribute this behavior to the fast CMP removal rate and high Ge dissolution rate of 25 nm/min for W2000-C. We therefore evaluated another commercial slurry, G1000 from Cabot Microelectronics, with 1:1 DI water dilution and 1 wt% H_2O_2 added using another wafer without any CMP history. The Ge dissolution rate for this slurry is only about 2.5 nm/min due to some unknown additive chemicals to prevent dissolution. The CMP removal rate is 270 nm/min for the Ge device waveguides. As shown in Figure 19(b), the Ge waveguide still extends 17 nm above the oxide after 90s CMP and the dishing is only 10 nm after an additional 60s over-polishing for the same wafer. The RMS roughness of Ge waveguides after CMP is $\sim 0.3\text{nm}$ confirmed by AFM measurements. Furthermore, the G1000 slurry also exhibits a slower CMP removal rate for denser waveguides. We observed a removal rate of 219 nm/min for 1 μm waveguides spaced by 10 μm , following the previously described pattern density effect.

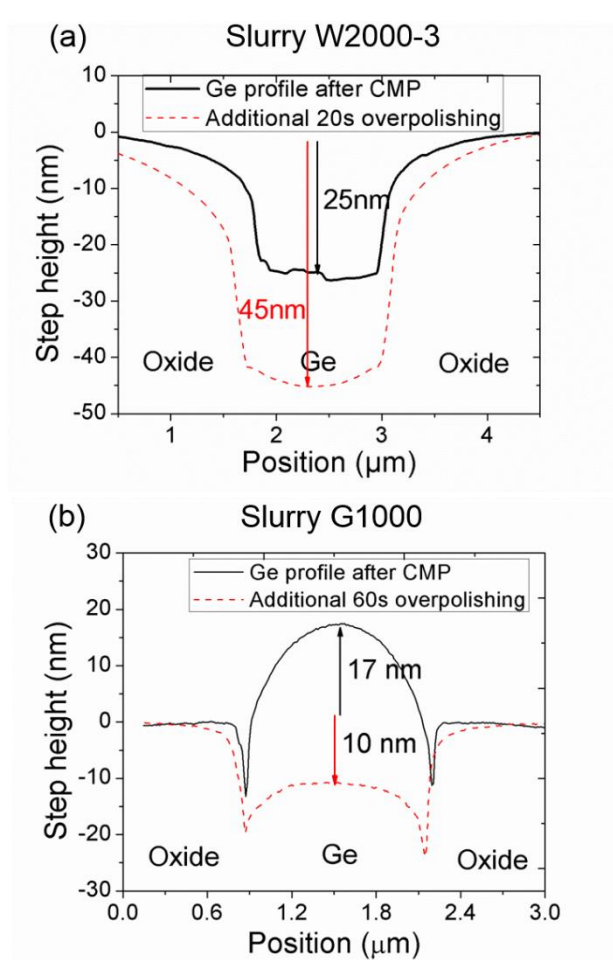


Figure 3.19 (a) 2D profile of Ge waveguides separated by 280 μm oxide measured by AFM after CMP for 60s and after an additional 20s over-polishing using W2000-C. (b) Ge waveguide height profile measured by AFM after CMP for 90s and after an additional 60s over-polishing using G1000

Therefore, we can use W2000 based slurry as a rough polish step with quicker speed if the over-grown Ge is very thick and then use G1000 based slurry as a fine finishing polish step to avoid Ge dishing in the oxide trench.

Chapter Summary

In Chapter 3, we provided a detailed process development for the formation of vertical oxide sidewalls, Ge selective growth and trench filling and finally a controllable CMP process with minimum dishing for the over-grown Ge. These steps are key steps for making the Ge laser with good performance. For the Ge selective growth, the vertical oxide sidewall can suppress the Ge (111) facet growth and enable the complete trench filling. We optimize the photolithography and oxide etch steps and show a detailed process recipe to achieve vertical oxide sidewall. When Ge grows at the oxide corners, it is difficult for Ge to fill a corner because of the rounded oxide corner. We design a T-shape oxide corner and the growth shows good trench filling. Using the T-shape corner, we can improve the reflectivity of the Ge/oxide interface as one end of mirror for a Fabry-Perot laser cavity. We investigate the Ge bufferless growth with the trench widths from 750 nm to $\sim 10 \mu\text{m}$ and find we can achieve faceted growth indicating single crystallinity without a low temperature buffer for trench openings smaller than $\sim 2 \mu\text{m}$. With this growth method, we can possibly eliminate the buffer layer which is an n-type dopant sink and also contains non-radiative recombination centers while still maintaining single crystalline Ge. A further study on the threading dislocations in the non-buffer grown Ge is required to make sure the non-buffer Ge can have threading dislocations as low as $\sim 1 \times 10^6 \text{ cm}^{-2}$ for the active material.

In addition, we also present a CMP process development for Ge waveguides over-grown in oxide trenches. We learn some important lessons: (1) the CMP removal rate of Ge can be adjusted by DI water dilution; (2) the CMP removal rate is pattern density related and therefore, dummy patterns are required for a uniform CMP across a wafer; (3) the chemical dissolution rate is directly related to the Ge dishing, therefore, we need to choose the slurry with a lowest dissolution rate; (4) for Ge, the acidic solution can suppress the Ge dissolution in the slurry. With

the above knowledge, we are able to selectively planarize Ge waveguides in oxide trenches with minimal dishing. If we can find a good way for the Ge CMP endpoint detection, it will be better to control the CMP automatically.

Chapter 4

N-type Doping and Dopant Diffusion in Ge

In both Chapter 1 and Chapter 2, we show the importance to achieve mid- 10^{19} cm^{-3} or even higher doping concentration in epitaxial Ge films on Si substrate. In this chapter, we will discuss the dopant introduction and dopant behavior in Ge in details starting with two different ways to incorporate dopants without excess damages to crystal lattice. They are *in situ* doping and extrinsic dopant source with drive-in process. In the second part of this chapter, we will discuss the dopant diffusion and out-diffusion behavior in Ge experimentally and theoretically. Finally, we investigate threading dislocations in n-Ge and analyze the possible reasons for the high threading dislocations in the n-Ge waveguide.

4.1 Ge n-type Doping

We limit our doping methods discussed here to gas phase doping because it will not add any damage to the crystal lattice such as vacancies and dislocations. Phosphorus (P), Arsenic (As) and Antimony (Sb) are the three main n-type dopants for Ge. Two critical criteria to evaluate these three dopants are solid solubility in thermal equilibrium and gas phase reaction to incorporate dopants into Ge.

The solid solubility is the highest concentration that dopants can dissolve in another material without forming a separate phase under thermal equilibrium. It is the fundamental limit of the highest concentration dopants can achieve in thermal equilibrium. Figure 4.1 shows the solid solubilities of P, As and Sb in Ge from literature. For Sb, the highest doping concentration is $\sim 1.2 \times 10^{19} \text{ cm}^{-3}$ at 800 °C [129], which is lower than the theoretically required doping level of mid- 10^{19} cm^{-3} to achieve high gain and low threshold current. For As, the highest doping concentration is close to $8 \times 10^{19} \text{ cm}^{-3}$ at 800 °C [129]. Both of the above doping levels were measured by Hall Effect measurement and thus the dopants are electrically activated. For P, the solid solubility is not very consistent from literatures. Barin et al. [130] shows the P solid solubility can go up to $1.5 \times 10^{20} \text{ cm}^{-3}$ at around 550 °C. However, Fistul et al. [131] shows that the highest solid solubility of P is only $\sim 7 \times 10^{19} \text{ cm}^{-3}$ at 800 °C and Zakhorov [132] also experimentally confirms a solubility result at 650 °C following Fistul's line. The solid solubility of P from Fistul is measured by Hall Effect and the solid solubility from Barin is measured from micro-hardness. Considering that the n-type dopants contributing for emission should be electrically active, we think Fistul's solid solubility should be more suitable. Furthermore, it is also confirmed by other researchers that Fistul's result is more reliable and more accepted [133].

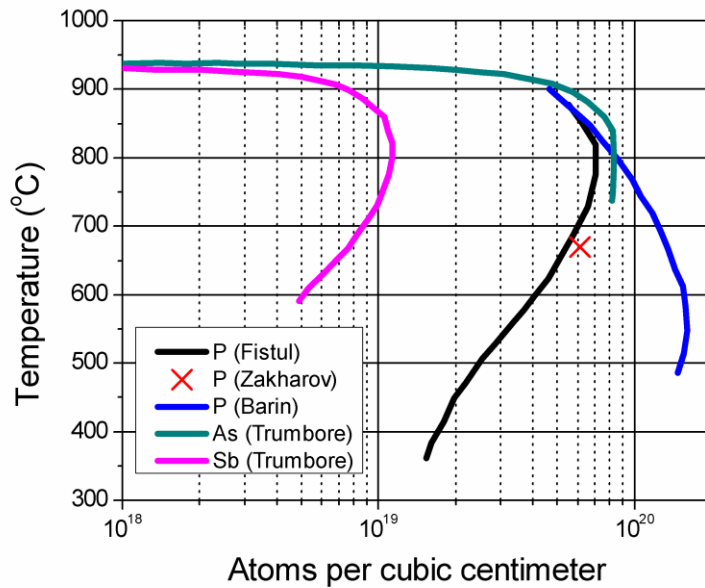


Figure 4.1 Solid solubility of P, As and Sb in Ge

Therefore, both P and As have the potential to be able to dope Ge to $7\sim 8 \times 10^{19} \text{ cm}^{-3}$ with complete electrical activation. Since gas phase reaction is used for doping Ge in the CVD tool, we need to investigate the gas phase reaction of PH_3 and AsH_3 , which are the common precursors for P and As, in detail. We neglect an Sb precursor because the solid solubility of Sb is too low for Ge lasing.

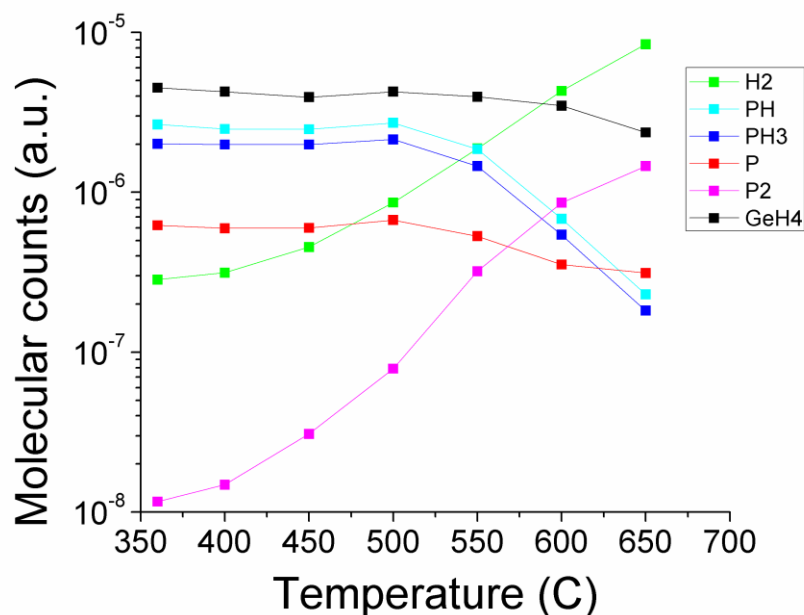


Figure 4.2 Molecular counts of PH_x and GeH_4 species under different tube temperatures

To study the PH_3 dissociation with temperature, we flow 12 sccm PH_3 into the UHV chamber and use a residual gas analyzer (RGA) to monitor the relative fraction of molecular counts. The tube pressure is ~ 10 mTorr. As shown in Figure 4.2, the major P related species are PH_3 , PH and a small amount of P when tube temperature is at 350 °C. PH_3 and PH are thermally stable up to 500 °C and then the concentrations start to drop through decomposition. P in the tube also remains almost constant until 500 °C but the drop with temperature is slower compared to PH_3 and PH. However, the P_2 concentration is continuously increasing with temperature, especially after 500 °C. From the plot, we can conclude that PH_x starts to decompose around 500 °C in the gas phase. P_2 instead of single P atoms is the product and also more stable in the gas phase. We also flow 3.8 sccm GeH_4 into the tube at the same time and the RGA shows GeH_4 does not decompose until ~ 600 °C.

We have to notice that the dissociation results of PH_x shown above are for the gas phase, not on the Ge surface. While PH_3 is exposed to the Ge (100) surface, PH_3 can adsorb to the Ge surface even at room temperature. The fragmentation, the P configuration with the Ge surface, and the desorption have to be studied differently while considering the Ge surface energy states. Tsi et al. [134] used high-resolution core-level photoemission spectroscopy to study the thermal reactions of phosphine on the Ge surface and found the following dissociation steps for PH_3 :

- (1) Initially, phosphine molecularly adsorbs on the Ge (100) surface at room temperature
- (2) The surface PH_3 gradually converts into PH_2 during annealing and at ~ 350 °C, the decomposition is complete while much of the adsorbed PH_3 desorbs into vacuum.
- (3) The PH_2 converts into P atoms when annealing at > 350 °C and the product H_2 desorbs from the Ge surface.
- (4) P atoms on Ge have multiple different bonding configurations when annealed between $400 \sim 520$ °C.

Bruckner [135] found that a P-terminated Ge (100) surface is stable in the temperature range of $300 \sim 430$ °C and the P desorption from a Ge (100) surface begins at 430 °C and completes at 450 °C. However, an As-terminated Ge (100) surface is more stable and As will not start to desorb until annealed at temperature higher than 650 °C. Usually the coverage of dopant atoms on the surface of Ge will slow down and even disrupt the epitaxial Ge growth because the number of available sites for Ge deposition is less. Experiments have shown that As can segregate at the Ge surface and change the surface morphology while the $\text{AsH}_3/\text{GeH}_4$ flow ratio is in the range of $2 \times 10^{-4} \sim 8 \times 10^{-4}$ and deposition temperature is in the range of 450 °C ~ 500 °C [136].

Therefore, we use PH_3 as the dopant precursor since the P-terminated Ge surface is less stable than the As-terminated Ge surface, indicating that we can grow Ge at a lower temperature without the disruptive growth due to surface termination by dopants.

4.1.1 n-Ge with *in situ* Doping

Using UHVCVD, Sun [76] demonstrated *in situ* doping of Ge, flowing a gas mixture of PH_3 and GeH_4 into the chamber at a given tube temperature and pressure. In this case, P doping occurs together with Ge growth. Sun found that the growth rate of *in situ* doped Ge is lower than the growth rate of intrinsic Ge at the temperature below ~ 600 °C and the as-grown Ge surface is rough. This observation is very similar to Ref. [136] which shows a reduced growth rate while flowing an $\text{AsH}_3/\text{GeH}_4$ mixture gas to dope Ge during Ge growth. The slower growth rate indicates that P possibly segregates at the Ge surface when the tube temperature is lower than 600 °C. Therefore, we need to grow Ge above 600 °C to get a specular surface.

Furthermore, Sun studied the active doping concentration in Ge with different growth parameters. He found that the active doping concentration does not change with PH_3/GeH_4 gas ratio, growth rate, and H_2 pressure. However, it changes with the growth temperature in a way as shown in Figure 4.3 and exhibits a maximum active doping concentration for *in situ* doping process.

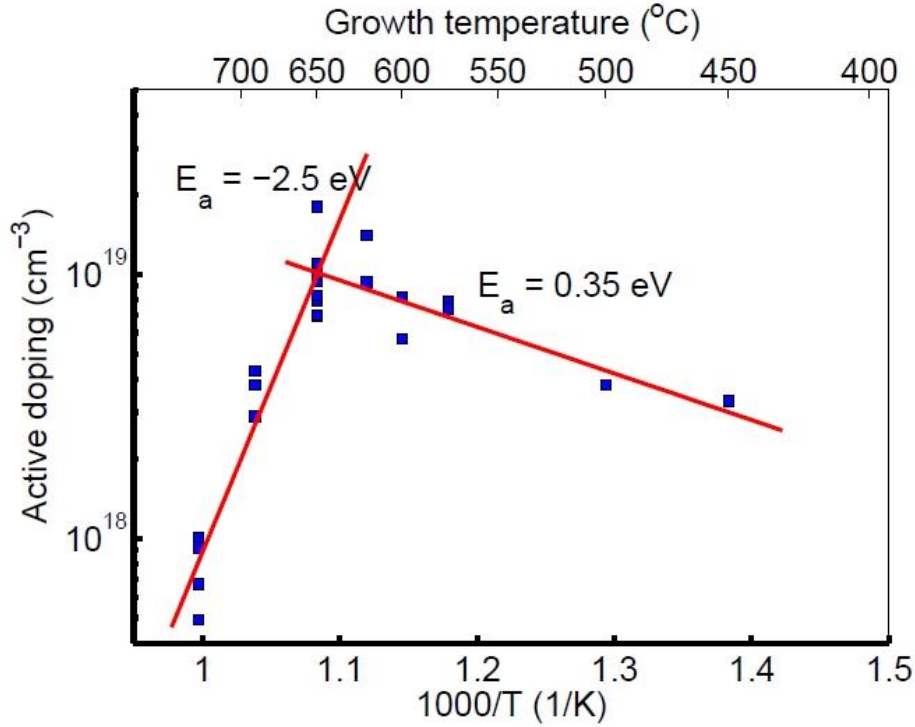


Figure 4.3 Arrhenius plot of *in situ* phosphorus doping concentration in Ge epitaxial films [76]

The precursor gases are 3.8 sccm GeH₄ and 12 sccm PH₃ at a tube pressure of 10 mTorr. At temperatures lower than 600 °C, the active doping concentration is lower because of P segregation and inactive P atoms in Ge. When temperature is higher, P desorption from the Ge surface dominates and thus the active doping concentration drops dramatically with rising growth temperature. However, the highest achievable active doping concentration of $1 \times 10^{19} \text{ cm}^{-3}$ only gives an optical gain of 50 cm^{-1} in Ge [137]. It is not very realistic to make an electrically pumped laser since gain has to overcome losses such as the cladding loss and mirror loss. Therefore, a new doping method has to be employed to achieve an active doping concentration of mid- 10^{19} cm^{-3} in Ge films.

4.1.2 n-Ge with Dopant Source

As discussed in Section 4.1, there is another way to dope Ge by saturating the Ge surface with PH_3 gas and thus 1 monolayer of P or less can form on the Ge surface. This method is called “delta doping” and it has been studied widely in Si and III-V films [138-140] and recently in Ge films [96, 141-143]. The method is to saturate the Ge surface with PH_3 gas and deposit a P monolayer on the Ge surface due to the low dissociation temperature of PH_3 and then encapsulate the P delta layer with Ge to achieve high P concentration in Ge.

Using UHVCVD, we develop a process recipe to create P delta layers encapsulated with the intrinsic Ge at the temperature of 360 °C ~ 450 °C. Before the delta doping layers, we grow a standard two-step *in situ* Ge thin film on the Si substrate. The detailed process steps are as followings:

- (1) Grow a 40 ~ 60 nm Ge buffer with 10 sccm GeH_4 at 360 °C;
- (2) Grow an *in situ* doped Ge layer with 3.8 sccm GeH_4 and 12 sccm PH_3 at 600 ~ 650 °C with the growth pressure around 10 mTorr;
- (3) Lower the tube temperature to 360 °C ~ 450 °C while flowing 12 sccm PH_3 to mitigate P out-diffusion;
- (4) Flow 12 sccm PH_3 for 5 ~ 10 min to saturate the Ge surface with PH_3 and its dissociated species;
- (5) Flow 10 sccm GeH_4 for 5 ~ 10 min to encapsulate the P delta layer with intrinsic Ge;
- (6) Repeat step 4 and 5 multiple times to create multiple delta layers;

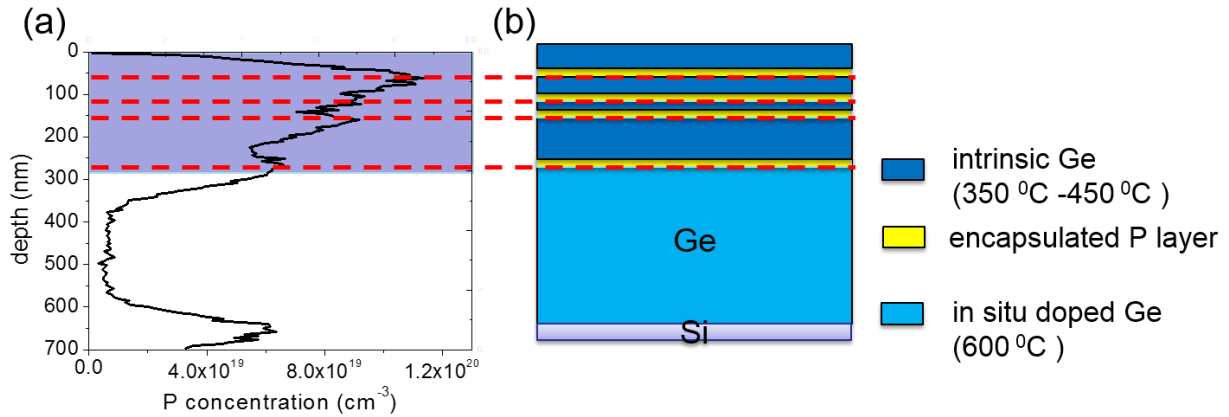


Figure 4.4 (a) P depth profile of Ge with delta-doped layer by SIMS (b) schematic drawing of Ge films with multiple delta-doped layers on Si substrate

Secondary ion mass spectroscopy (SIMS) measurements are performed on the as-grown sample to determine the phosphorous depth profile (Figure 4.4a). The high phosphorous concentration up to 10^{20} cm^{-3} within the depth of $\sim 300 \text{ nm}$ shows a successful encapsulation of P atoms in delta layers. Because the deposition temperature of the intrinsic Ge is at $400 \text{ }^\circ\text{C}$, P diffusion occurs and thus the P concentration peaks at the delta-doped positions are not very distinct. It is also possible that the residual PH_3 gas in the tube dopes the intrinsic Ge because we start to flow GeH_4 gas immediately after stopping the PH_3 flow. P also diffuses into the in-situ doped Ge layer from the delta layers, which can be clearly seen in Figure 4.4(a). The knock-on artifact, i. e., ions pushing P further into the underlying layer during the SIMS process, can be ruled out since this is effective within $10\sim 20\text{nm}$ only [139]. The arising P concentration at the interface of the Ge buffer and Si substrate is due to P accumulation in the un-doped Ge buffer layer due to the high defect density.

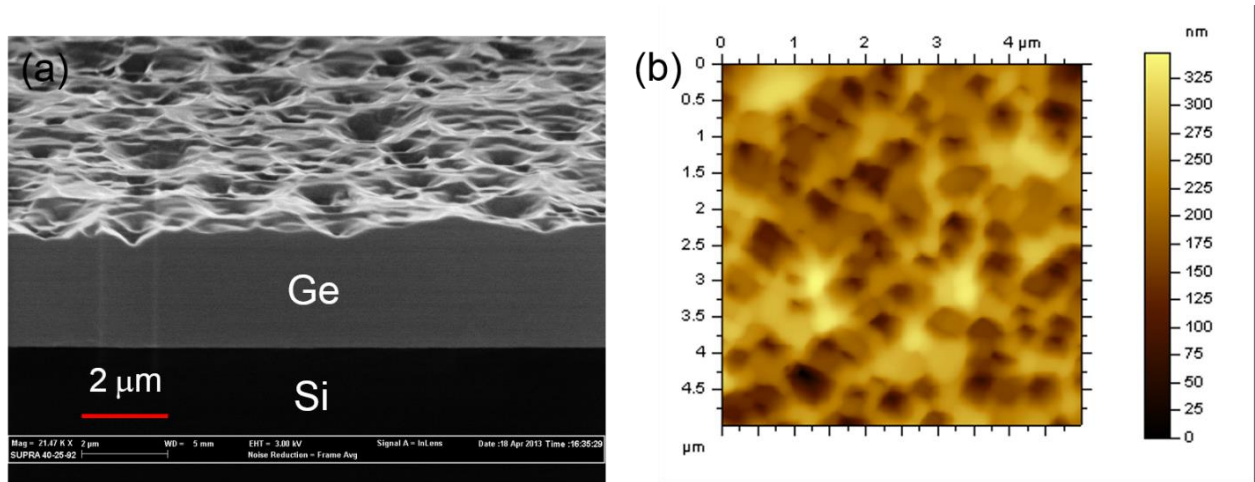


Figure 4.5 (a) SEM image (b) AFM image of the as-grown delta-doped blanket Ge film

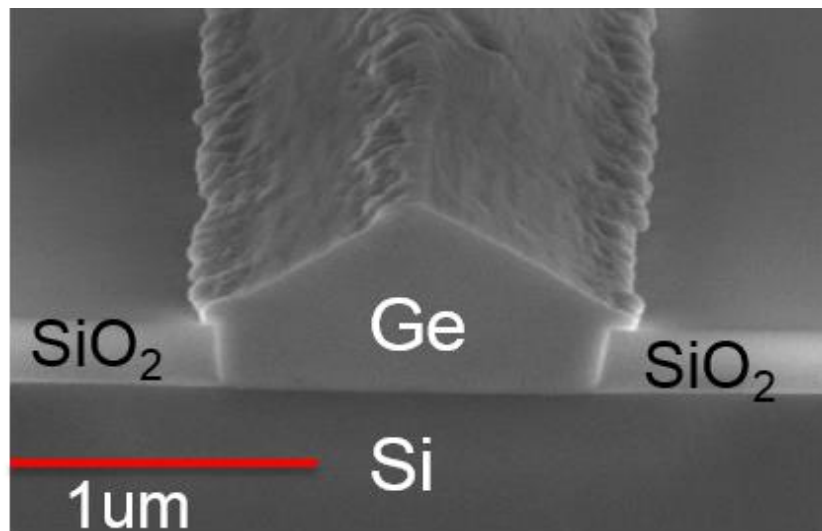


Figure 4.6 Cross sectional SEM image of a Ge waveguide with delta-doped layers

We then use SEM and atomic force microscopy (AFM) to characterize the as-grown Ge films and waveguides. From both Figure 4.5 and Figure 4.6, we observe a rough Ge surface after the delta-doped layers. The measured RMS of roughness by AFM is ~ 50 nm. We know that the *in situ* Ge has a specular surface for the blanket film and a faceted waveguide when grown in

oxide trenches. Therefore, the degradation of the crystal quality of Ge is due to the delta doped layers. One possible reason is that the P delta-layer forms a monolayer of P on the Ge surface and thus disrupts the epitaxial Ge growth. Another reason is that we find the intrinsic Ge grown at 450 °C does not show a specular surface if the growth pressure is too high.

4.1.3 Dopant Drive-in Process through Annealing

The encapsulation of P delta layers in Ge is successful. We measured up to $1 \times 10^{20} \text{ cm}^{-3}$ P concentration with four delta layers within the thickness of 300 nm. However, Ge with delta-doped layers shows a poor crystalline quality with high surface roughness. It is obvious that the heavily doped Ge layer is not suitable for the active gain material due to defects. We therefore utilize this heavily doped layer as a dopant source to diffuse P from delta-doped layers into the *in situ* Ge layer underneath through rapid thermal annealing (RTA). We deposit a 100nm thick SiO₂ on the Ge film as a cap layer to prevent out-diffusion during annealing. Furthermore, we find that the active carrier concentration is $1.5 \times 10^{19} \text{ cm}^{-3}$, measured by Hall Effect, for the as-grown Ge sample with delta-doped layers. Compared to the average P concentration of $4.4 \times 10^{19} \text{ cm}^{-3}$ from the SIMS profile, we can conclude that the P is not completely electrically activated. Hence, annealing is required to activate the P, which also causes P diffusion into the in-situ doped Ge layer to achieve a higher doping concentration with single crystalline quality.

RTA at various conditions is performed on the as-grown samples and SIMS and Hall Effect measurements are carried out (Table 4.1 and Figure 4.7). The standard measurement error for the Hall Effect measurement setup is $\pm 10\%$. The comparable data between the average P concentration from SIMS and the active carrier concentration from Hall Effect measurements

show that the P dopants are completely activated after annealing. During annealing, dopant loss by out-diffusion is observed, which can be concluded from the decrease of average P concentration with longer annealing times. Driven by the concentration gradient, P diffuses deeper into the Ge layer from the source with longer annealing time. High carrier concentration and an even distribution profile are the criteria to determine the best annealing condition. We conclude that RTA at 600 °C for 3min is a good annealing condition for dopant diffusion for the Ge sample shown in Figure 4.4a. In this case, an evenly distributed carrier concentration of $2.5 \times 10^{19} \text{ cm}^{-3}$ is achieved in the single crystalline Ge.

Table 4.1 Average phosphorous concentration from SIMS measurements and activated carrier concentration from Hall Effect measurements

RTA		Average P concentration	Activated carrier
Temperature (°C)	Time (s)	by SIMS (cm^{-3})	concentration by Hall (cm^{-3})
600	30	3.3×10^{19}	$(2.9 \pm 0.3) \times 10^{19}$
	60	3.0×10^{19}	$(2.6 \pm 0.3) \times 10^{19}$
	180	2.5×10^{19}	$(2.8 \pm 0.3) \times 10^{19}$
700	60	2.5×10^{19}	$(2.6 \pm 0.3) \times 10^{19}$

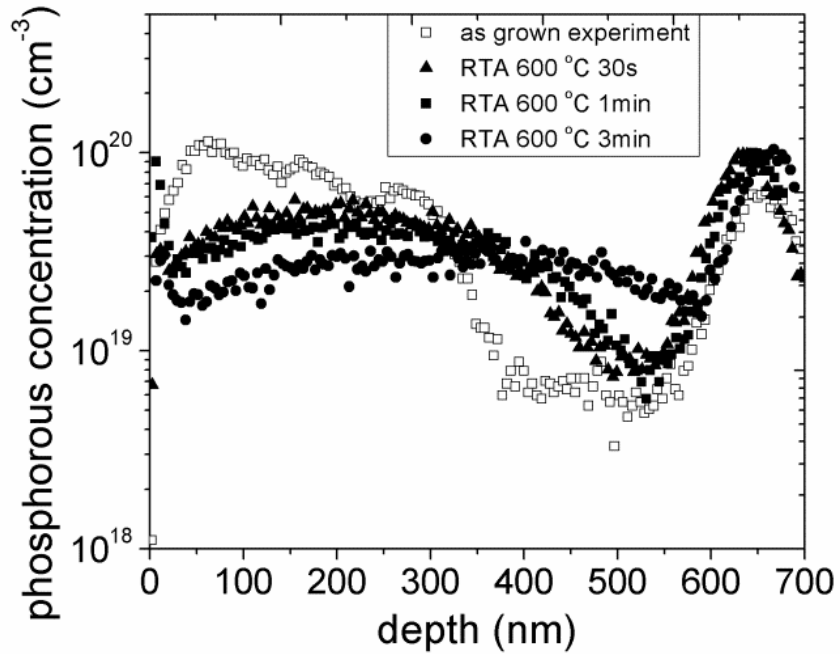


Figure 4.7 SIMS depth profiles of Phosphorus in Ge for an as-grown sample (open squares) and after RTA at 600 °C for 30s (full triangles), 1min (full squares), and 3min (full circles)

Furthermore, we studied the sources of dopant loss during annealing. The as-grown *in situ* doped Ge should have a uniform doping concentration of $1 \times 10^{19} \text{ cm}^{-3}$ through the entire thickness. We leave the as-grown film in the UHVCVD chamber at 650 °C for 5 min and measure the P depth profile by SIMS, as shown in Figure 4.8. The P concentration peaks at the Ge surface $x=0$ and there is a clear P concentration drop near the surface. This observation indicates that P tends to out-diffuse from the bulk to the surface and segregate at the surface. Additionally, there is another P peak around 550 nm where the Ge buffer is located. Since the Ge buffer is undoped and full of defects, we believe that it acts as a dopant sink during the high temperature anneal.

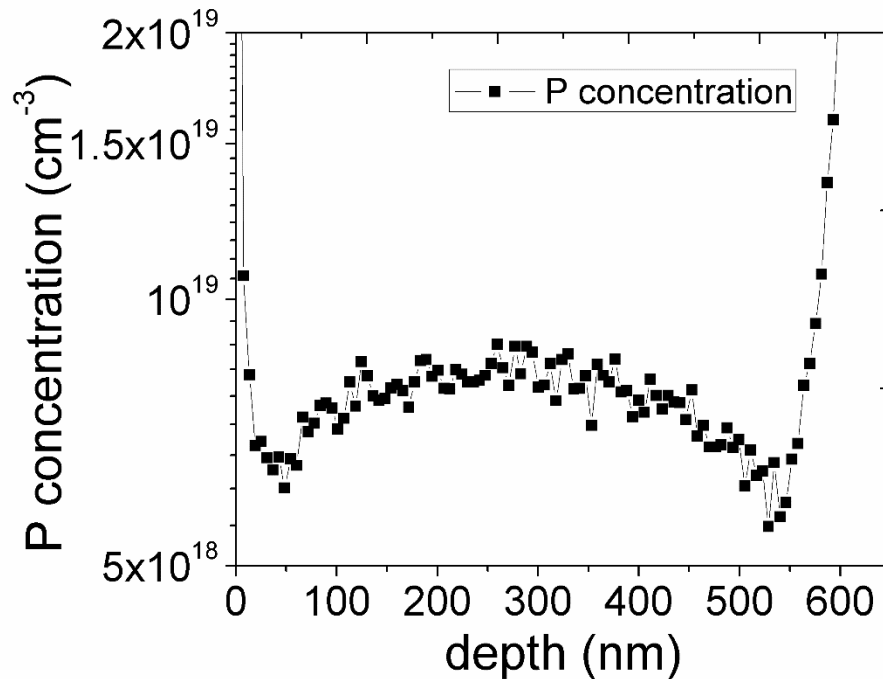


Figure 4.8 P depth profile of the *in situ* doped Ge after annealing at 650 °C for 5 min measured by SIMS

We test amorphous Si (a-Si) as another cap layer to prevent out-diffusion. We find that an a-Si cap works better compared to an oxide cap layer. We deposit 100 nm oxide and 100 nm a-Si on delta-doped Ge using plasma enhanced chemical vapor deposition (PECVD). After annealing the samples with the oxide cap and a-Si cap, we strip away the capping layers and measure the active doping concentration by Hall Effect. From Table 4.2, we can see that the doping concentration in Ge with the a-Si cap layer is higher than the sample with the oxide cap under the same annealing condition. Additionally, there is no further dopant loss with longer annealing time or higher annealing temperature with the a-Si cap layer. However, Ding’s study on different capping layers to prevent As out-diffusion from Ge concludes a comparable capping effect of

oxide and a-Si while Si₃N₄ works best to keep As from out-diffusion [74]. Therefore, we use silicon nitride as the cap layer in future to test the possibility to mitigate the out-diffusion.

Table 4.2 Active P doping concentration in Ge films under various annealing conditions with the oxide cap and amorphous Si cap

RTA parameters	SiO ₂ cap	a-Si cap
600 °C, 10s	$1.54 \times 10^{19} \text{ cm}^{-3}$	$1.91 \times 10^{19} \text{ cm}^{-3}$
600 °C, 60s	$1.86 \times 10^{19} \text{ cm}^{-3}$	$2.06 \times 10^{19} \text{ cm}^{-3}$
700 °C, 10s	$1.58 \times 10^{19} \text{ cm}^{-3}$	
700 °C, 30s		$2.11 \times 10^{19} \text{ cm}^{-3}$
700 °C, 60s		$2.07 \times 10^{19} \text{ cm}^{-3}$
750 °C, 10s		$2.16 \times 10^{19} \text{ cm}^{-3}$
800 °C, 10s		$2.03 \times 10^{19} \text{ cm}^{-3}$

4.2 Dopant Diffusion Behavior in Ge

Theoretical calculations predict that the vacancy formation energy in Ge (2eV) is significantly lower than that in Si (3.5eV) which implies that vacancies play a more important role in Ge than in Si [144]. Previous results by Werner et al. [145] demonstrate that Ge self-diffuses by a vacancy mechanism in which vacancies act as acceptors and all n-type dopants (P, As, and Sb) have higher diffusivity in Ge than Ge itself [146]. This fact reveals that an attractive interaction between n-type dopants and vacancies helps the formation of dopant-vacancy pairs (DV⁻). In the

following, we present a model using the vacancy mechanism for the phosphorous diffusion in Ge. The charge state of the vacancy is assumed to be doubly negative which is consistent with other assumptions of the phosphorous diffusion mechanism [147]. The extrinsic diffusivity $D_{(DV)^-}$ is quadratic carrier concentration dependent and can be expressed as follows:

$$D_n = D_{(DV)^-} = D_0 \left(\frac{n}{n_i} \right)^2, \quad (4.1)$$

where D_0 is the intrinsic diffusivity, n is the equilibrium carrier concentration in the Ge, and n_i is the intrinsic carrier concentration in tensile strained Ge at the diffusion temperature. Due to the reduction in the band gap and the splitting of the valence bands, the intrinsic carrier concentration in tensile strained Ge is given by [148]:

$$n_i = \sqrt{N_c (N_{lh} + N_{hh} \exp(\frac{-\Delta E}{kT})) \exp(-\frac{E_g}{2kT})}, \quad (4.2)$$

where N_c is the effective density of states of electrons in the conduction band, N_{lh} is the effective density of states of light holes in the valence band, N_{hh} is the effective density of states of heavy hole in the valence band, and ΔE is the splitting energy of light and heavy holes at the Γ valley. The basic Fick's second law is used to model the diffusion:

$$\frac{\partial n(x)}{\partial t} = \frac{\partial}{\partial x} (D_{(DV)^-}(n) \frac{\partial n}{\partial x}), \quad (4.3)$$

The boundary condition across the Ge/SiO₂ interface is characterized by the surface loss flux in the following expression [149]:

$$\Phi = -f_p (n_{P(Ge)} - n_{P(SiO_2)}), \quad (4.4)$$

where f_p is the loss rate, $n_{P(Ge)}$ is the phosphorous concentration on the surface of Ge, and $n_{P(SiO_2)}$ is the phosphorous concentration on the surface of SiO₂. For the short experimental RTA times, we assume f_p is constant.

Since Ge is grown on Si using a 60nm undoped Ge buffer, we have to consider the buffer layer with a high dislocation density as a sink for phosphorous diffusing into this layer. A pile-up model is described by Fahey [149] and Normand [150] based on the McNabb and Foster model. This model is used by Tsouroutas et al. [151] to simulate the phosphorous pile-up phenomenon close to the Ge surface during the diffusion. Using a similar approach, Fick's second law has to be modified [151]:

$$\frac{\partial n(x,t)}{\partial t} + P(x) \frac{\partial \Phi(x,t)}{\partial t} = \frac{\partial}{\partial x} (D_{(DV)^-}(n) \frac{\partial n(x,t)}{\partial x}), \quad (4.5)$$

$$\frac{\partial \Phi(x,t)}{\partial t} = kn(x,t)(1 - \Phi(x,t)). \quad (4.6)$$

where $P(x,t)$ is the concentration of the traps related to dislocations and $\Phi(x,t)$ is the fraction of traps that is occupied with dopants at time t. Equation 4.6 holds that the trapping is permanent and k is a measure of the trapping rate. Since the diffusion coefficient is carrier concentration dependent in the extrinsic diffusion region, a simple erf function, which assumes a constant diffusivity, is not applicable for the modeling. The simulations of phosphorous diffusion in Ge were performed using the finite difference time domain (FDTD) method.

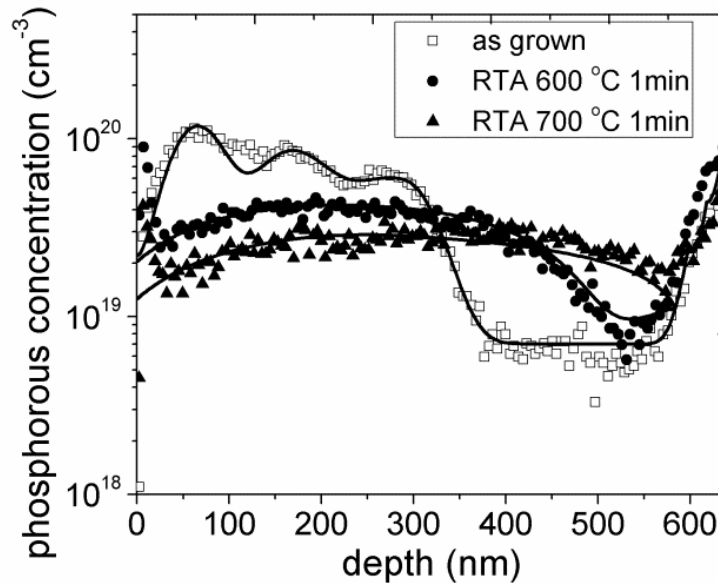


Figure 4.9 SIMS depth profiles of P in Ge for an as-grown sample (open squares) and after RTA at 600 °C (full circles) and 700 °C (full triangles) for 1min. The solid lines are the simulation results.

A box-shaped profile of dopant distribution normally appears in bulk Ge with increasing doping level [147], however, in thin Ge films the profiles (Figure 4.9) tend to have an even distribution of dopants. The good fit between simulation and experiment shows that the dopant diffusion coefficient $D_{(DV)}$ increases quadratically with the carrier concentration n in the extrinsic diffusion region. To study the doping effect on the phosphorous diffusion, we prepared Ge samples with different background doping levels. As shown in Figure 4.10, two as grown films have the same delta doped layers as the diffusion source but one film (full squares) has an intrinsic Ge layer with phosphorous concentration below $2 \times 10^{17} \text{ cm}^{-3}$ and the other film (full circles) has an in-situ doped Ge layer with phosphorous concentration of $\sim 1 \times 10^{19} \text{ cm}^{-3}$. Under the same thermal treatment, it is obvious that phosphorous in in-situ doped Ge (open circles)

diffuses faster than that in intrinsic Ge (open squares). Considering that the diffusion source and boundary conditions are the same, we conclude that the enhanced diffusion is due to the background doping level.

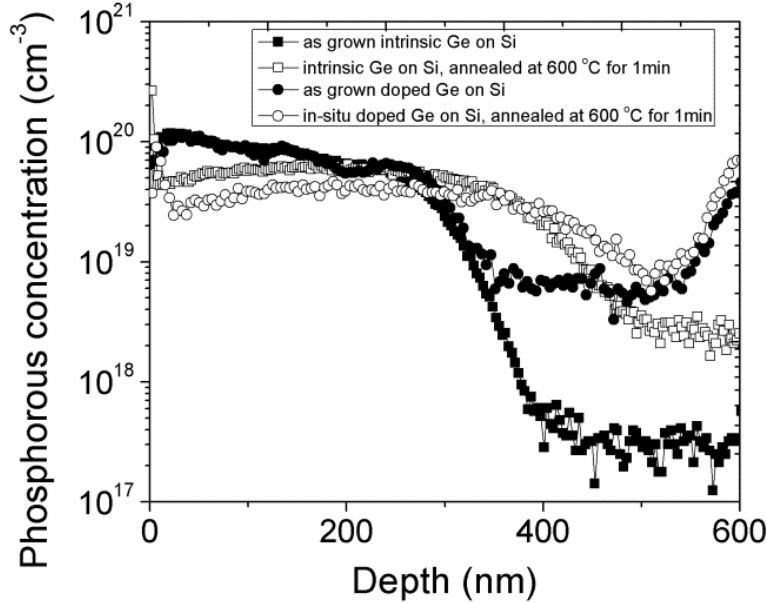


Figure 4.10 SIMS depth profiles of P from different Ge-on-Si films. P in intrinsic Ge with delta doped layers on top as-grown (full squares) and annealed at 600 °C for 1min (open squares). P in *in situ* doped Ge with delta doped layers on top as-grown (full circles) and annealed at 600 °C for 1min (open circles).

The intrinsic diffusion coefficients are illustrated in Figure 4.11, deduced from the best fit for annealing temperatures of 600 °C, 650 °C, and 700 °C against the diffusivity extracted for the same temperature range from recent publications of other groups. As shown in Figure 4.11, the intrinsic diffusivities from our experiments have comparable values to the results from other groups. Generally, the diffusivity versus temperature shows an Arrhenius behavior and hence, we use $D = D_0^* e^{-E_a/kT}$ to fit the three data points. The activation energy is $E_a = 1.98eV$ and the pre-

exponential coefficient is $D_0^* = 2.2 \times 10^{-4} \text{ cm}^2 / \text{s}$, similar to the literature values. The intrinsic carrier concentration in tensile strained Ge is $2.09 \times 10^{17} \text{ cm}^{-3}$ at $600 \text{ }^\circ\text{C}$ and $3.88 \times 10^{17} \text{ cm}^{-3}$ at $700 \text{ }^\circ\text{C}$. Due to the in-situ doping during growth, the carrier concentration in the Ge layer before annealing is increased to $1 \times 10^{19} \text{ cm}^{-3}$. Therefore, the extrinsic diffusivities in the in-situ doped Ge region, shown as the open squares in Figure 4.11, are about 2 orders of magnitude higher than the diffusivities in intrinsic Ge.

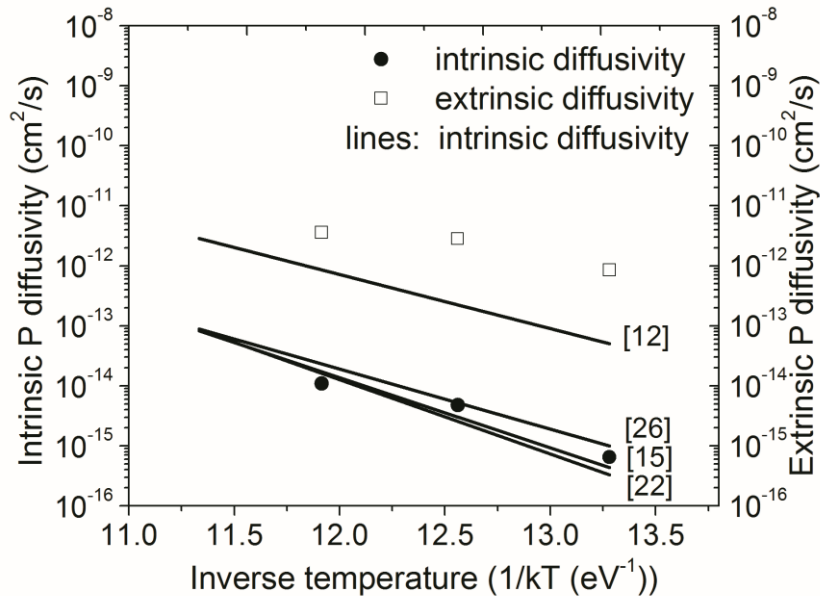


Figure 4.11 Full circles represent the intrinsic diffusivity of phosphorous in Ge from this work. Open squares represent the extrinsic diffusivity of phosphorous in Ge from this work. Intrinsic diffusivities from other groups [147, 151-153] for temperature ranging from $600 \text{ }^\circ\text{C}$ to $750 \text{ }^\circ\text{C}$ are plotted by lines as comparisons

In conclusion, we show that we can achieve a uniform phosphorous distribution with the concentrations above $3 \times 10^{19} \text{ cm}^{-3}$ by utilizing phosphorous delta-doped layers created in a

UHVCVD growth process as a dopant reservoir and then annealing. The dopant enhanced in-diffusion defeats the net loss by out-diffusion from the Ge surface and the pileup at Ge/Si interface. This concentration is significantly higher than can be achieved in a CVD growth process while preserving high quality Ge thin films that can be used as gain medium for CMOS compatible Ge lasers. We also investigate the background doping effect on the phosphorous diffusion in Ge. Phosphorous diffusion is enhanced by a factor of 100 when background doping is $1 \times 10^{19} \text{ cm}^{-3}$ in Ge. We build an FDTD model to simulate phosphorous diffusion which fits the depth profile measured by SIMS very well; we find that the diffusivity varies quadratic with carrier concentration.

4.3 Threading Dislocation in n-Ge

A threading dislocation originates from the lattice mismatch between Ge and Si. A typical as-grown intrinsic epi-Ge on Si film has a threading dislocation density (TDD) in the order of $10^8 \sim 10^9 \text{ cm}^{-2}$ using a two-step growth process. Using high temperature or cyclic anneal, threading dislocation density can be reduced to $\sim 10^7 \text{ cm}^{-2}$ in the $1 \mu\text{m}$ thick blanket intrinsic Ge due to threading dislocation glide and annihilation [26]. The threading dislocation performance in the intrinsic Ge is well understood. The importance to have a low TDD in Ge is that threading dislocations can act as non-radiative recombination centers for the injected minority carriers and then reduce the minority carrier lifetime in the material. As mentioned in Chapter 2, the SRH recombination lifetime is $\tau_{p,300K} = \frac{1}{\sigma_p v_p N_k N_{dislocation}} = 10 \text{ ns}$ when the threading dislocation density is $1 \times 10^8 \text{ cm}^{-2}$ and the number of the charged kink sites is $1.3 \times 10^6 / \text{cm}$ with n-type doping of $1 \times 10^{19} \text{ cm}^{-3}$. The non-radiative recombination lifetime is comparable with the direct band

radiative lifetime. A high threading dislocation density in an optical gain medium is usually one of the reasons for high lasing threshold [51]. In GaAs based semiconductor lasers, research showed the TDD greater than 10^6 cm^{-2} can reduce the minority carrier lifetime enough to prohibit laser operation [154]. Therefore, we think that threading dislocation density is also a very important material parameter for Ge laser devices. A low TDD in Ge will help to improve the optical performance of Ge laser.

In our recently demonstrated electrically pumped Ge laser devices, we used n-Ge doped to $4.5 \times 10^{19} \text{ cm}^{-3}$ by the delta-doping method followed by the CMP as described in the previous chapters. The active Ge material was grown on Si at $650 \text{ }^\circ\text{C}$ with *in situ* doping and then received a thermal treatment at $750 \text{ }^\circ\text{C}$ for 1 min for dopant drive-in process. The Ge was selectively grown in $1 \text{ }\mu\text{m}$ wide oxide trenches with a length of $\sim 5 \text{ mm}$. We used plan-view transmission electron microscopy (PVTEM) to examine the threading dislocation density in this kind of n-type doped Ge waveguides. The TEM sample was prepared using a combination of mechanical grinding and ion milling. The sample was first glued onto the polishing holder with the Si substrate facing outside. It was mechanically polished down to a thickness of approximately $10 \text{ }\mu\text{m}$. The sample was then ion milled using a Fischione ion milling system from the backside of the Si substrate until the specimen was perforated in the center.

Figure 4.12 shows an average TDD of $1.9 \times 10^9 \text{ cm}^{-2}$ in a 300 nm thick and $1 \text{ }\mu\text{m}$ wide Ge waveguide by PVTEM. The dislocation line is not straight but shows a zigzag contrast due to the interference of the electron beams through the TEM sample. This waveguide represents the typical Ge material used for the Ge laser. Based on the discussion in Chapter 2, the non-radiative recombination lifetime will be 0.2 ns and the estimated threshold current density will be $\sim 200 \text{ kA/cm}^2$ for the Ge waveguide with a TDD of $1.9 \times 10^9 \text{ cm}^{-2}$ and a doping concentration of

$4.5 \times 10^{19} \text{ cm}^{-3}$. The high TDD and the Ge dishing after CMP are two reasons for the measured high lasing threshold current density of 300 kA/cm^2 in our electrically pumped lasers. In order to understand the formation of the high threading dislocation density, we evaluate the following four possible reasons carefully: (1) annealing conditions; (2) the thin Ge material; (3) Si/Ge inter-diffusion at the Si/Ge interface; (4) the narrow Ge waveguide.

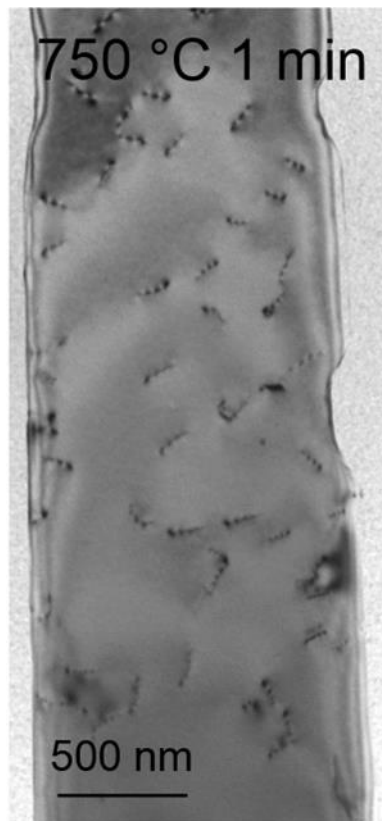


Figure 4.12 Plan-view TEM showing uniform threading dislocations in n-type Ge annealed by rapid thermal annealing at 750 °C for 1 min. (TEM courtesy of Tim Milakovich)

4.3.1 Effect of Annealing Temperature

From Ref [155], we know that annealing at temperatures higher than 750 °C is necessary to effectively reduce threading dislocations in Ge. The required high temperature is because that

TDs at high temperatures have increased probability of overcoming the Peierls–Nabarro potential with the aid of thermal fluctuation. Therefore, the TDs in the Ge laser material may not have the high enough thermal energy to move because the thermal treatment is only 750 °C RTA for 1 min. We then selectively grow the 1 μm wide Ge waveguide with *in situ* doping and anneal it at 850 °C for 40 min. However, the high temperature anneal will cause dopant out-diffusion from n-Ge as described before. Figure 4.13 is the PVTEM of the Ge waveguide by annealing at 850 °C for 40 min with the thickness of 350 nm showing an average TDD of $(1.4 \pm 0.4) \times 10^9 \text{ cm}^{-2}$. The same order of magnitude of the TDD in Ge waveguides annealed at 750 °C for 1 min and 850 °C for 40 min indicates that the higher temperature annealing may not help the TDs reduction in the narrow and thin Ge waveguides. The annealing experiments on the intrinsic Ge films show that cyclic anneal or even higher temperature anneal such as 900 °C can reduce the TDD more effectively. It is worth to repeating the similar annealing conditions on our n-type doped Ge waveguides. However, the observation that 850 °C annealing makes no difference on the TDD makes us to explore other possible reasons for this high TDD in the n-type doped Ge waveguides.



Figure 4.13 Plan-view TEM showing uniform threading dislocations in a 1 μm wide and 350 nm thick n-type Ge waveguide by annealing at 850 °C for 40 min. (TEM courtesy of Tim Milakovich)

4.3.2 Effect of the Ge Layer Thickness

The thermal strain energy increases with the Ge epi-layer thickness. The interaction energy between neighboring TDs also increases with the Ge epi-layer thickness. Therefore, threading dislocations in thicker Ge films have a higher driving force to overcome barriers for dislocation motion. In intrinsic Ge films, the TDD can reduce from $1 \times 10^8 \text{ cm}^{-2}$ at the thickness of 600 nm to $2 \times 10^7 \text{ cm}^{-2}$ at the thickness of 1.2 μm [155]. When the intrinsic Ge is 350 nm thickness, the TDD is about $3 \times 10^8 \text{ cm}^{-2}$. To examine the thickness effect to the TDs in n-type doped Ge film, we grow a 1 μm thick *in situ* doped blanket Ge film and anneal it at 850 °C for 40 min. Hall Effect measurements showed an active dopant concentration drop from $1 \times 10^{19} \text{ cm}^{-3}$ to $3 \times 10^{18} \text{ cm}^{-3}$. The

etch-pit-density (EPD) method is another common method to evaluate the TDD in intrinsic Ge films. To generate etch pits, chemicals generally used are a mixture of CH₃COOH (67 ml), HNO₃ (20 ml), HF (10 ml) and I₂ (30 mg). The etch time is only 5s to avoid etching too much of Ge films.

However, when we apply the EPD etchant solution to the doped Ge film, we cannot do the EPD counting although we observe a rougher surface and a thinner Ge film. The EPD etchant might be not selective to etch the dislocated Ge and the heavily doped Ge. We then use PVTEM to check the TDD in the doped and annealed Ge film (Figure 4.14). The TEM sample of Ge-on-Si film shows a wedge shape. When the electron beam is applied on the TEM sample from the Ge top, we can observe that the threading dislocation density increases from the thin Ge film to the thick Ge film including Ge buffer, as shown from the pictures from right to left, respectively. In the 1 μm thick n-type doped Ge film, we observe an average TDD of 9×10⁷ cm⁻². When the film is thinner, the threading dislocation density increases. We plot the two data points from our work in Figure 4.15 together with the TDD dependence with thickness in Ref. [156], which also gives an equation to estimate on the threading dislocation density in blanket Ge films after annealing:

$$\rho_{eq} \cong \left[\frac{4\pi(1-\nu)E_a}{\mu b^3 L(1-\nu \cos^2 \theta)} \right]^2 \quad (4.7)$$

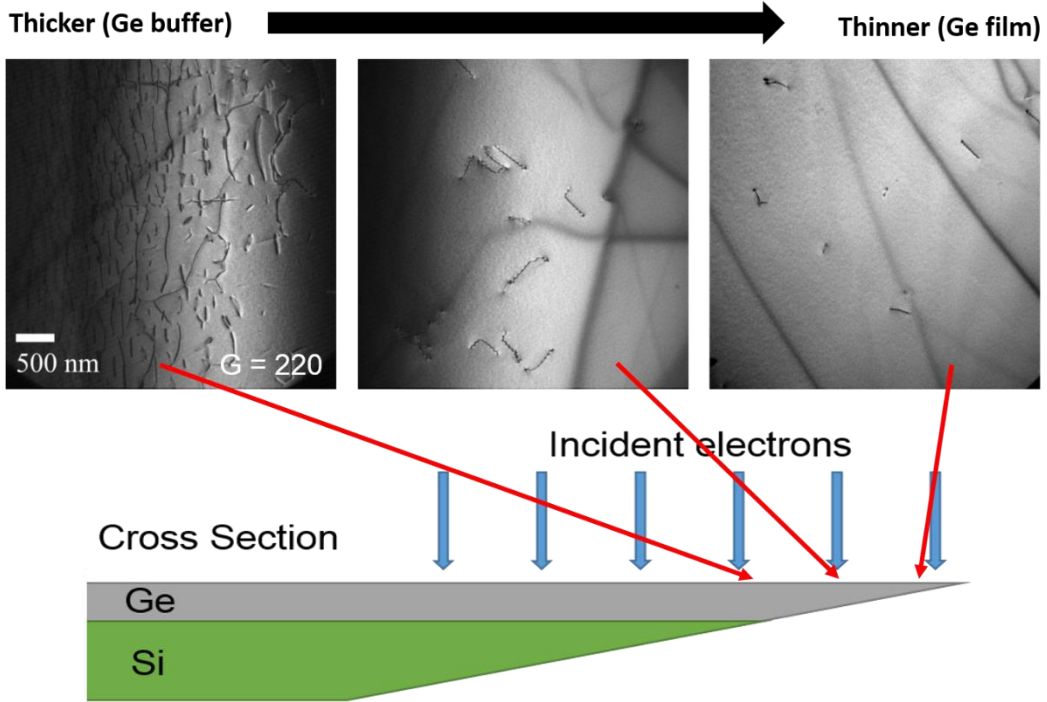


Figure 4.14 PVTEM showing the threading dislocations in Ge from thicker buffer to the top of Ge film (TEM courtesy of Tim Milakovich)

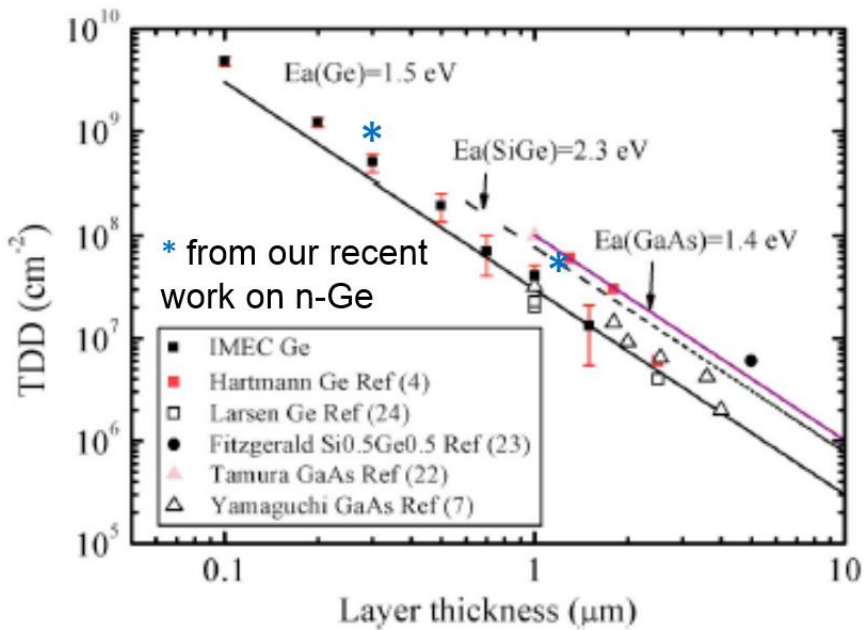


Figure 4.15 TDD from our Ge films (stars) compared to the TDD from the Ref. [156]

In Equation 4.7, $\nu = 0.273$ is the Poisson ratio of Ge, $\mu = 67.0$ GPa is the Shear modulus of Ge, $b = 4.0 \text{ \AA}$ is the Burgers vector length, $\theta = 60^\circ$ is the angle between the Burgers vector and the dislocation line direction, L is the threading dislocation length assumed to be the film thickness. E_a is the activation energy for threading dislocations to glide and annihilate. In Ref. [157], the gliding activation energies are 1.57 eV, 1.75eV and 1.2 eV for intrinsic Ge, Ga doped Ge and As doped Ge, respectively. The dislocation glide velocity increases with n-type doping when the doping concentration is greater than 10^{18} cm^{-3} . The reduced gliding activation energy due to n-type doping is related to the charged dislocation sites. Using the lower activation energy due to n-type doping in Ref. [155], we should expect lower TDDs in our n-Ge films compared to the intrinsic Ge with the same thickness. However, as depicted in Figure 4.15, the TDDs measured in the n-Ge films after high temperature anneal are higher.

The discrepancy indicates two possible reasons. One is that the annealing condition at 850 °C for 40 min is not enough for dislocation glide to reach the thermal equilibrium condition as mentioned in Section 4.3.1. Another is that the dislocation line is charged due to heavy n-type doping and thus dislocation annihilation energy is increased by the Coulombic repulsion potential. Further investigation is required to verify the two assumptions.

Additionally, we learn that the Ge film thickness is critical for the threading dislocation density. A thicker Ge film will have a lower TDD with the same growth condition.

4.3.3 Effect of Si/Ge Inter-diffusion

Si/Ge inter-diffusion is observed particularly the upward diffusion of Si into the deposited Ge when the Ge-on-Si film is annealed at high temperature such as 900 °C [158]. The diffusion of Si in Ge is also known as vacancy assisted [159]. From our analysis of P diffusion in Ge, we learn

that the n-type doping in Ge increases the vacancy concentration and therefore enhance the P diffusion in Ge. Therefore, the enhanced diffusion of Si into Ge is also possible due to the heavy n-type doping in Ge although further experimental confirmation is necessary. The effect of Si/Ge inter-diffusion to threading dislocation density is that the alloying Ge with Si shows a monotonous drop of dislocation velocity in Ge. In $\text{Si}_{0.5}\text{Ge}_{0.5}$, the glide activation energy increases to 2.3 eV [160]. It is possible that the alloying at the Ge/Si interface caused by enhanced Si/Ge inter-diffusion due to n-type doping under high temperature anneal, will retard the dislocation glide by increasing the gliding activation energy and therefore increase the threading dislocation density.

4.3.4 Effect of the Trench Width

In the selective grown Ge mesa structure, the TDD can reduce from $2 \times 10^7 \text{ cm}^{-2}$ with 100 μm wide mesa to $2 \times 10^6 \text{ cm}^{-2}$ with 10 μm wide mesa because that threading dislocations can glide and terminate at the Ge/oxide interface. However, the TDD in the 1 μm wide Ge waveguide shows no difference compared to the blanket Ge film while taking the thickness into consideration. In addition, we also observe a TDD above 10^8 cm^{-3} in the 500 nm and 2 μm wide Ge waveguides without a clear observation of the TDD reduction with the width of Ge waveguide with buffer (Figure 4.16). Therefore, we can conclude that the size effect does not apply on the thin, n-type Ge waveguides with the high temperature anneal. One possible reason is that the strain energy is too small due to the thickness so that the threading dislocations can only glide for a very limited distance in one anneal cycle. Cyclic anneal might be the solution to keep the dislocations glide to the Ge/oxide sidewalls. Since the cross sectional TEM only images

Figure 4.16 Cross sectional TEM of the buffered grown Ge waveguide (a) 500 nm wide with 25KX magnification (b) 2 μm wide with 10KX magnification (c) 2 μm wide with 25KX magnification after annealing at 850 $^{\circ}\text{C}$ for 40 min.

To make the Ge laser with a low threshold current, we require both high n-type doping and low threading dislocation density. One possible way is that we grow the intrinsic Ge on Si and anneal the film to reduce the threading dislocation density first and then we put the delta-doped Ge layer as the dopant diffusion source. Using this doping method, we can have the low TDD in Ge. However, the dopant drive-in speed will be slower because we cannot take the advantage of dopant enhanced diffusion. The possible drawback of this doping method is that we may get an n-type doping concentration of low mid- 10^{19} cm^{-3} in Ge and thus increase the threshold current density of the laser. However, the temperature dependent simulation of the threshold current indicates that the mid- 10^{19} cm^{-3} doping level is good for the temperature stability of the laser.

Chapter Summary

In this chapter, we cover three main topics related to n-type dopant in Ge. The first topic is about how to introduce n-type doping concentration of mid- 10^{19} cm^{-3} in Ge without extra defects. From the previous work, we know that the *in situ* doping concentration is limited to $1 \times 10^{19} \text{ cm}^{-3}$ in Ge by UHVCVD. We employ a non-equilibrium doping method called “delta doping” to encapsulate the monolayer of P atoms inside Ge and the P concentration can reach more than $1 \times 10^{20} \text{ cm}^{-3}$ in the delta-doped layers, confirmed by the SIMS measurements. We then use RTA to diffuse the dopant from this dopant source to the underlying *in situ* doped Ge layer. With control of the delta layer thickness and the *in situ* Ge thickness, we can flexibly achieve the

active n-type doping concentration of $(1\sim 5) \times 10^{19} \text{ cm}^{-3}$. This high doping concentration enables efficient electron injection and direct band optical transition and thus an electrically pumped Ge laser can be achieved.

The second topic is about the understanding of the P dopant diffusion behavior in Ge. The diffusion of P in Ge is mediated by a negatively charged defect, which is related to the vacancy. This insight has been studied and well accepted by previous reports. We use the vacancy assisted diffusion to simulate our P diffusion curves and confirm the validity of the assumption. We find that the *in situ* doping facilitates a faster drive-in process due to dopant enhanced diffusion. The extracted extrinsic diffusivities in the *in situ* Ge layer are about two orders of magnitude higher than the intrinsic diffusivities.

The third topic is to study and reduce the threading dislocation density in the blanket n-Ge films as well as waveguides. From the PVTEM, we find that the TDD in the Ge waveguides which were demonstrated for Ge lasing is as high as $1 \times 10^9 \text{ cm}^{-2}$. The high TDD might be one of the reasons why the Ge laser device have a high threshold current density of 300 kA/cm^2 . Based on the knowledge that high temperature annealing can reduce the TDD and the smaller trench size will also help the TDD reduction, we examine the TDD in the blanket n-Ge film and narrower n-Ge waveguides after high temperature anneal at $850 \text{ }^\circ\text{C}$ for 40 min. We find that the TDD in the $1 \text{ }\mu\text{m}$ thick n-Ge blanket film is $\sim 1 \times 10^8 \text{ cm}^{-2}$ and the TDD in the 350 nm thick, $1 \text{ }\mu\text{m}$ wide n-Ge waveguide is $\sim 1 \times 10^9 \text{ cm}^{-2}$. The high TDD in annealed Ge can be attributed to either reduced glide stress or reduced annihilation. The reduced glide stress is possibly because of the lower tensile stress in the narrower waveguides. So far the cross sectional TEM results on the 500 nm and $2 \text{ }\mu\text{m}$ wide Ge waveguides do not show an obvious difference in the TDD. Further PVTEM on waveguides with varying widths might be required to confirm the results. The

reduced annihilation might be due to the thinner Ge layer or lower annealing temperatures or less annealing cycles. The Si/Ge inter-diffusion might also be the reason causing a higher gliding activation energy. To fully understand the cause of the high TDD in thin Ge waveguides, we need to analyze each possible reason carefully.

Chapter 5

Ge External Cavity Laser Design on SOI

In this chapter, we present a comprehensive Ge external cavity laser design of a Si/Ge/Si heterojunction structure based on an SOI platform. The motivations of the design are to: (1) reduce the threshold current and increase the differential quantum efficiency of an electrically pumped Ge laser; (2) achieve single mode emission; (3) integrate the Ge laser with Si waveguides. There are several special material parameters related to the Ge laser so that the laser design has to be carefully addressed. It is important to design an optimum Si cladding layer thickness and Ge active region thickness to mitigate optical modal loss because both the Si claddings and Ge layer are heavily doped. We need to reconsider the current injection method because the active Ge region is heavily doped with a thin Si layer as the n-type cladding on the

SOI substrate. In addition, since Ge is a high refractive index material, the coupling between Ge and Si waveguides also requires a careful evaluation. In the following paragraphs, we will discuss the above problems in detail and provide some design rules to achieve the design motivations listed before.

5.1 Internal Optical Loss

From Equation 1.12 for the theoretical threshold current and Equation 1.14 for the theoretical differential quantum efficiency, we notice that internal optical loss α_i is a very important device parameter. A low α_i is required to reduce the threshold current and increase the differential quantum efficiency and therefore, the laser device can have a better power efficiency.

The internal optical loss α_i includes free carrier absorption (FCA) loss from cladding layers n-Si and p-Si in the Ge laser device, and free carrier absorption loss from the active Ge layer. The equation to calculate the internal optical loss is as follows:

$$\alpha_i = \Gamma_{Ge}\alpha_{Ge} + \Gamma_{n-Si}\alpha_{n-Si} + \Gamma_{p-Si}\alpha_{p-Si} \quad (5.1)$$

where Γ_{Ge} is the confinement factor representing the fraction of optical mode confined in the active Ge region and Γ_{n-Si} , Γ_{p-Si} are confinement factors for optical mode in the n-Si cladding and the p-Si cladding respectively. If the optical mode extends to the metal layers on top of the Si cladding, we then have to also include the absorption loss from the metal to calculate the total internal optical loss. We use FIMMWAVE from Photon Design to simulate the total internal optical loss from all layers at the wavelength of 1.7 μm in this chapter.

From Sun's previous simulation work, we know that both Si cladding layers have to be heavily doped [76]. He calculated the light emission intensity from the $p^+Si/n^+Ge/n^+Si$ p-n-n

diode versus the doping concentrations in both p-type and n-type Si regions. He found that heavy p-type doping in Si can promote the hole injection level leading to more direct gap radiative recombination. Therefore, the concentration of $1 \times 10^{20} \text{ cm}^{-3}$ in p-Si and $1 \times 10^{19} \text{ cm}^{-3}$ in n-Si were proposed for the Ge p⁺Si/n⁺Ge/n⁺Si p-n-n diode.

The free carrier absorption coefficient of Si is dependent on doping and wavelength as predicted by Soref [37]:

$$\Delta\alpha_{n-si} = 8.5 \times 10^{-18} \Delta n \left(\frac{\lambda (nm)}{1550 nm} \right)^2 \quad (5.2)$$

$$\Delta\alpha_{p-si} = 6 \times 10^{-18} \Delta p \left(\frac{\lambda (nm)}{1550 nm} \right)^2 \quad (5.3)$$

The FCA of n-Si cladding with $1 \times 10^{19} \text{ cm}^{-3}$ doping is 102 cm^{-1} at $1.7 \mu\text{m}$ and the FCA of p-Si cladding with $1 \times 10^{20} \text{ cm}^{-3}$ doping is 722 cm^{-1} at $1.7 \mu\text{m}$. For the FCA in n-Ge, we use Ge with a doping concentration of $5 \times 10^{19} \text{ cm}^{-3}$ as an example. The injected carrier concentration at threshold is about $1.1 \times 10^{19} \text{ cm}^{-3}$ from Section 2.2 at $1.7 \mu\text{m}$. The FCA of n-Ge is then 325 cm^{-1} .

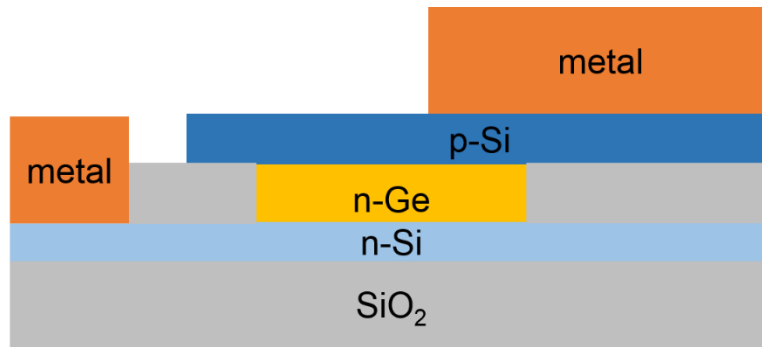


Figure 5.1 A schematic drawing of the cross section of Ge pnn junction

A schematic drawing of the pnn diode cross section is shown in Figure 5.1. The n-Si thickness is 70 nm. We estimate the internal optical loss with varying Ge and Si parameters, such as Ge width and thickness, p-Si thickness and metal position. Table 5.1 shows the results from a 1 μm wide Ge waveguide with 100 nm Ti and 1 μm Al above the Ge. The internal optical loss shows a decreasing trend with thicker Ge due to less mode overlap with Si cladding and metal layers. However, the Ge is limited in thickness because the required injection current increases linearly with the thickness. The internal optical loss also shows a decreasing trend with thicker p-Si cladding because the metal has much higher absorption loss than p-Si. The cross section design with metal directly above the Ge waveguide requires a thick p-Si cladding such as 400 nm and a moderate thick Ge active medium such as 300 nm. The internal optical loss is then 416 cm^{-1} , which is mostly contributed by the FCA from n-Ge.

Since the metal contact is the major loss source for thin Ge and thin p-Si, we estimate the internal optical loss for devices without metals above the Ge waveguide. The results with varying Ge thickness and p-Si thickness are shown in Table 5.2. Similarly, the internal optical loss reduces with increasing Ge thickness but the changes are much smaller compared to the Ge with metal above it. However, the internal optical loss increases with thicker p-Si because the FCA of p-Si is larger than that of n-Ge so less mode overlap with p-Si is favored. The cross section design without metal directly above the Ge waveguide requires a thin p-Si cladding such as 100 nm and a moderate thick Ge active gain medium such as 300 nm. The internal optical loss is then 363 cm^{-1} , which is still mostly due to the FCA from n-Ge but is about 50 cm^{-1} lower than the Ge pnn junction with the metal directly above Ge.

Table 5.1 Internal optical loss of a pnn junction with 1 μm wide Ge and metals directly above Ge

Ge thickness (nm)	p-Si thickness (nm)			
	100	200	300	400
200	2199 cm^{-1}	993 cm^{-1}	648 cm^{-1}	532 cm^{-1}
250	1604 cm^{-1}	767 cm^{-1}	532 cm^{-1}	457 cm^{-1}
300	1237 cm^{-1}	633 cm^{-1}	467 cm^{-1}	416 cm^{-1}
350	999 cm^{-1}	549 cm^{-1}	428 cm^{-1}	394 cm^{-1}

Table 5.2 Internal optical loss of a pnn junction with 1 μm wide Ge and metals not directly above Ge

Ge thickness (nm)	p-Si thickness (nm)			
	100	200	300	400
200	381 cm^{-1}	415 cm^{-1}	433 cm^{-1}	443 cm^{-1}
250	371 cm^{-1}	394 cm^{-1}	406 cm^{-1}	412 cm^{-1}
300	363 cm^{-1}	380 cm^{-1}	388 cm^{-1}	391 cm^{-1}
350	358 cm^{-1}	370 cm^{-1}	375 cm^{-1}	378 cm^{-1}

From the above two tables, we find that the internal optical loss is now mostly contributed by n-Ge because the absorption losses from Si cladding layers and metals have been minimized. We also learn that thinner p-Si cladding layers are preferred for Ge devices without metals directly above the active region. Therefore, we set the thickness of p-Si to 100 nm and

estimate how the internal optical loss changes with varying Ge waveguide widths and thicknesses. Table 5.3 shows the calculation results. We label specifically if the internal optical loss is from TM mode when the fundamental mode of the Ge pnn cross section is TM. All the other internal optical losses are from fundamental TE mode. Generally, a larger Ge active region has a lower internal optical loss because the optical mode extends mostly into the Si cladding layers when the Ge active region shrinks and this leads to higher losses. However, the increased loss is not significant with a narrower Ge waveguide with the width of 500 nm. Instead, a narrower waveguide is beneficial for the uniform current injection into Ge, which will be discussed in the following section. The tradeoff is difficult to quantify theoretically and thus, experimental comparison of the optical performance for Ge laser with different areas is very important and beneficial for the further understanding of the Ge laser performance.

Table 5.3 Internal optical loss of a pnn junction with 500 nm wide Ge and metals not directly above Ge

Ge thickness (nm)	Ge width (nm)			
	300	500	750	1000
200	422 cm ⁻¹	403 cm ⁻¹	388 cm ⁻¹	381 cm ⁻¹
250	442 cm ⁻¹ (TM)	392 cm ⁻¹	377 cm ⁻¹	371 cm ⁻¹
300	417 cm ⁻¹ (TM)	384 cm ⁻¹	369 cm ⁻¹	363 cm ⁻¹
350	399 cm ⁻¹ (TM)	378 cm ⁻¹	363 cm ⁻¹	358 cm ⁻¹

Although we compare several device parameters to mitigate the internal optical loss, the optimized value of 363 cm⁻¹ is still large compared to the several cm⁻¹ loss in typical III-V lasers.

We therefore estimate the effect of the high internal optical loss to the laser threshold current and differential quantum efficiency of the laser.

Equation 1.12 for threshold current is listed here again: $I_{th} = \frac{qV}{\eta_i \tau} (N_{tr} + \frac{\alpha_i + \alpha_m}{\Gamma a})$. We still use n-type doping of $5 \times 10^{19} \text{ cm}^{-3}$ as the example. The transparent carrier concentration N_{tr} for this doping at $1.7 \text{ } \mu\text{m}$ is $1.1 \times 10^{19} \text{ cm}^{-3}$ and the differential gain coefficient a is $1.03 \times 10^{-16} \text{ cm}^2$. The confinement factor in Ge for the structure with p-Si (100 nm)/ n-Ge (300 nm)/n-Si (70 nm) is 0.93. Therefore, the required injected carrier concentration to overcome the internal optical loss is $\frac{\alpha_i}{\Gamma a} = 3.8 \times 10^{18} \text{ cm}^{-3}$, which is about three times lower than the transparent carrier concentration. Therefore, the high internal optical loss will definitely increase the threshold current but is not the dominant factor.

Equation 1.14 for differential quantum efficiency is also listed here again: $\eta_d = \frac{\eta_i \alpha_m}{\alpha_m + \alpha_i}$.

The higher internal optical loss will reduce the power efficiency and also limit the output power.

The equation to calculate mirror loss α_m is:

$$\alpha_m = \frac{1}{2L} \ln\left(\frac{1}{R_1 R_2}\right) \quad (5.4)$$

where L is the cavity length and R_1, R_2 are the front and back mirror reflectivity respectively. With a typical cavity length of $200 \text{ } \mu\text{m}$ and reflectivity of 18.9% from Ge/oxide interface, the mirror loss is estimated to be $\sim 83 \text{ cm}^{-1}$. The differential quantum efficiency is 18.8% with an extreme assumption of 100% internal quantum efficiency η_i , which means that all the current injected into the device contributes into the Ge injection without any possible current leakage path. This low quantum efficiency is mainly due to the high internal optical loss α_i .

Therefore, the internal optical loss after optimization of the Si/Ge/Si heterojunction is still a limiting factor to achieve high power efficiency. A different cross section structure is

required to improve the threshold and power efficiency, such as adding a separated confinement layer like in III-V quantum well laser.

5.2 Current Injection in Ge Laser on SOI

In this section, we use the commercial software Sentaurus to simulate the 2D current density distribution of a Si/Ge/Si hetero-structure by solving the Poisson equation. Sentaurus can simulate numerically the electrical behavior of a semiconductor device. Terminal currents, voltages, and charges are computed based on a set of physical device equations that describes the carrier distribution and conduction mechanisms. A pnn junction is represented in the simulator as a ‘virtual’ device whose physical properties are discretized onto a non-uniform grid (or mesh) of nodes. After defining the simulation structure, we have to select the physical models suitable for our structure and input parameters suitable for Ge. Therefore, we will present the physical models and corresponding materials parameters we use in the current injection simulation in Section 5.2.1. We then discuss the effect of metal contact position on the current injection uniformity in Section 5.2.2.

5.2.1 Physical Models in Sentaurus

1. Recombination Mechanisms

In Section 2.3, we find the necessity to include non-radiative recombination in the photoluminescence simulation to explain the PL intensity reduction at high temperatures. We use Shockley-Read-Hall (SRH) recombination and surface recombination as two major sources of

non-radiative recombination in Ge. In a Ge pnn junction, surface recombination can be neglected because the Ge surface is passivated by the Si cladding layer. We then only consider SRH recombination for Ge device simulation. In Sentaurus Device, Equation 2.6 is implemented with the parameters for Ge based on the extracted parameters from the PL simulation (Table 5.4).

Table 5.4 Ge parameters for SRH recombination

Parameter	Units	Ge (e,h)
τ_{\min}	s	0,0
τ_{\max}	s	5.3×10^{-5} , 5.3×10^{-5}
N_{ref}	cm ⁻³	2×10^{15} , 2×10^{15}
γ		0.8,0.8
T_{coeff}		2.5,2.5
E_{trap}	eV	0,0

2. Carrier Mobility

Since Ge is n-type doped, we need to include the impurity scattering model into the simulation, which means the mobility is a function of doping in Ge. We use a model proposed by Masetti et al. [161] and the Ge parameters are from Hellings et al. [162] who uses Sentaurus for Ge pMOSFET simulation. Table 5.5 lists the Ge parameters used for simulation.

Table 5.5 Ge parameters for doping dependent mobility

parameters	Units	Ge (e,h)
$\mu_{\min 1}$	cm^2/Vs	60, 60
$\mu_{\min 2}$	cm^2/Vs	0, 0
μ_1	cm^2/Vs	20, 40
P_c	cm^{-3}	10^{17} , 9.23×10^{16}
C_r	cm^{-3}	8×10^{16} , 2×10^{17}
C_s	cm^{-3}	3.43×10^{20} , 10^{20}
α		0.55, 0.55
β		2.0, 2.0

3. Other Mechanisms

Additionally, we assume the carrier distribution in conduction and valence bands follows Fermi-Dirac distribution instead of Boltzmann distribution for high n-type doped Ge and Si. Besides, since Si/Ge/Si is a hetero-junction, there are abrupt energy barriers at the interface. We therefore use the thermionic emission over the barrier to simulate the current.

5.2.2 Sentaurus Simulation Results

In the simulation, we use the mechanisms discussed before to simulate the injected carrier distribution in the Ge pnn junction on SOI. We mainly simulate three different kinds of

structures based on the internal optical loss calculation in Section 5.1. They are (a) 1 μm Ge waveguide with metals directly above Ge, (b) 1 μm Ge waveguide without metals directly above Ge and (c) 500 nm Ge waveguide without metals directly above Ge. We examine the contact position in order to get more uniform current injection across the Ge active region. An example of a Sentaurus simulation code is presented in Appendix II.

Structure 1: 1 μm Ge waveguide with a thick p-Si cladding

In this structure, we have a 70 nm thick n-Si cladding with a doping concentration of $1 \times 10^{19} \text{ cm}^{-3}$, a 400 nm thick p-Si cladding with a doping concentration of $1 \times 10^{20} \text{ cm}^{-3}$ and a 300 nm thick n-Ge layer with a doping concentration of $5 \times 10^{19} \text{ cm}^{-3}$. We first simulate the structure with symmetric current injection where metals are contacting p-Si in the center and n-Si at two sides as shown in Figure 5.2. Figure 5.2 depicts the doping concentrations in each layer. Figure 5.3 shows the corresponding current injection distribution in the layers under a 1.5 V applied voltage. Since the bottom n-Si is as thin as 70 nm while the active Ge region is heavily n-type doped, the n-Si is the most resistant part in the current flow paths. The highest current density is in the n-Si layer underneath the oxide. Due to the resistance of n-Si, the current also concentrates at the two lower corners in the Ge region with a current density above 150 kA/cm^2 . Instead, the Ge center has a lower current density of $\sim 30 \text{ kA/cm}^2$, where the optical mode mostly overlaps. The non-uniform current injection will be a problem to achieve a population inversion with uniform gain in the Ge active region and also the two lower corners can be hot spots for over-heating.

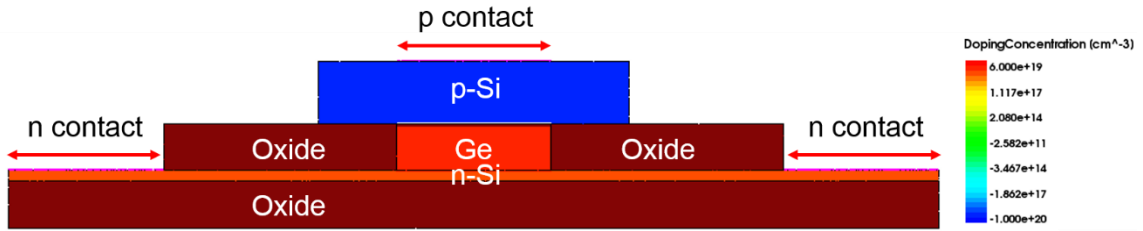


Figure 5.2 Cross section of doping concentration for Ge pnn junction with a symmetric current injection

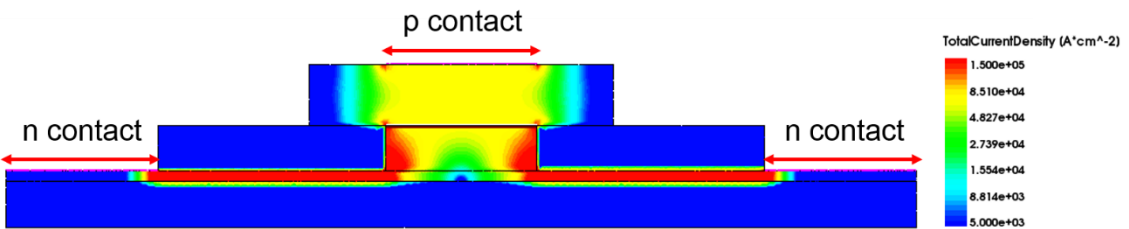


Figure 5.3 Cross section of current injection distribution for Ge pnn junction with a symmetric current injection

We then simulate the diagonal injection with one p contact and one n contact at each side to enforce the current injection path to cross the Ge center. We change the p contact position relative to Ge to evaluate the position effect to the current injection uniformity. In Figure 5.4, we simulate three different metal positions: (a) is where the metal has a full overlap with Ge; (b) is where the metal only has a half overlap with Ge and (c) is where the metal has a quarter overlap with Ge. Similarly, n-Si is the most resistant part and therefore has the highest current density. Comparing the three different metal positions, we can observe a more uniform current distribution inside the active Ge region with the less overlap between the metal and Ge. The other benefit to have metals away from Ge is the reduction of the free carrier loss from metal

layers. Therefore, diagonal current injection helps the current injection uniformity while n-Si is very thin and resistive compared to symmetric injection.

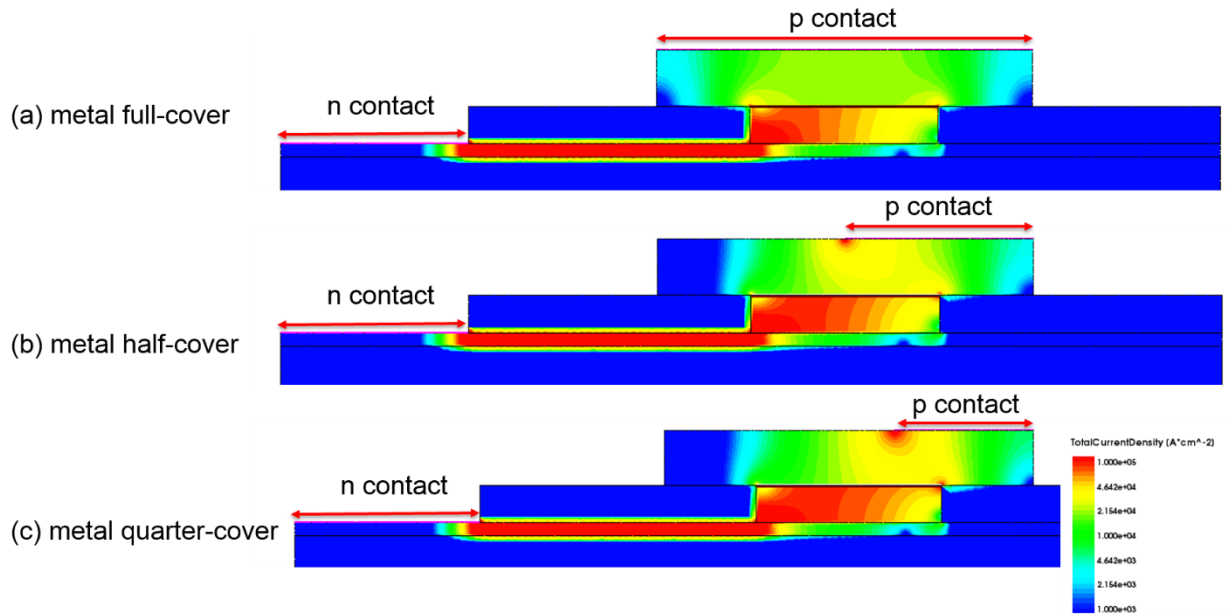


Figure 5.4 Cross section of current injection distribution for Ge pnn junction with a diagonal current injection (a) metal full-cover (b) metal half-cover (c) metal quarter-cover

Structure 2: 1 μm Ge waveguide with a thin p-Si cladding

In Section 5.1, we conclude that the free carrier absorption from metals is the main loss term if the p-Si cladding layer is thin metals are directly above Ge. Therefore, for the Ge waveguide with a thin p-Si cladding, we simulate the structure without metals directly above Ge. The layers for the pnn junction are a 70 nm thick n-Si with a doping concentration of $1 \times 10^{19} \text{ cm}^{-3}$, a 70 nm thick p-Si with a doping concentration of $1 \times 10^{20} \text{ cm}^{-3}$ and a 300 nm thick n-Ge with a doping concentration of $5 \times 10^{19} \text{ cm}^{-3}$ for a 1 μm wide Ge waveguide. The simulation result in Figure 5.5 shows a very uniform injection into the Ge center with two current-concentrated spots at the

diagonal corners. Considering this structure also gives the lowest internal optical loss, we think a thin layer of p-Si with metals away from the Ge waveguide might be the optimum structure for both internal optical loss reduction and current injection uniformity. One of the drawbacks of this structure is that the diode resistance is higher than the previously discussed structures. However, the current density inside Ge can still reach $\sim 30 \text{ kA/cm}^2$ with a 1.2V applied voltage, which is higher than the threshold we predicted.

Structure 3: 500 nm Ge waveguide without metals above Ge

The third structure we simulate is a Ge pnn junction with a single transverse mode. The layers include a 70 nm thick n-Si cladding with a doping concentration of $1 \times 10^{19} \text{ cm}^{-3}$, a 100 nm thick p-Si cladding with a doping concentration of $1 \times 10^{20} \text{ cm}^{-3}$ and a 300 nm thick n-Ge layer with a doping concentration of $5 \times 10^{19} \text{ cm}^{-3}$ for a 500 nm wide Ge waveguide. Similarly as the simulated Structure 2, there is a uniform current distribution in the Ge center and also a current accumulation at the two Ge corners (Figure 5.6). There is also no obvious improvement on the current uniformity with a narrower Ge waveguide, indicating that Ge is not the layer mainly causing the non-uniform current injection.

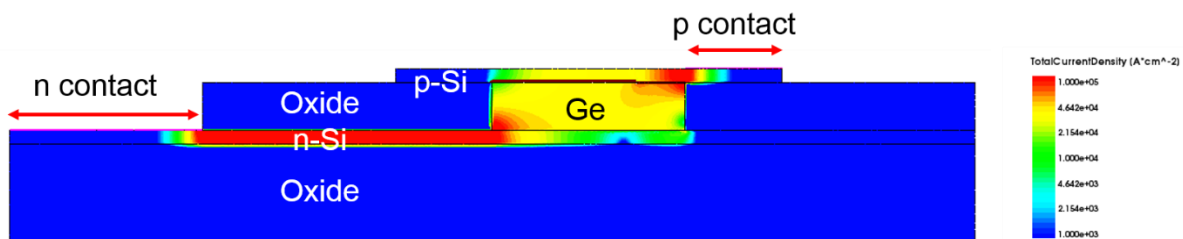


Figure 5.5 Cross section of current injection distribution for Ge pnn junction with a diagonal current injection with a thin p-Si cladding

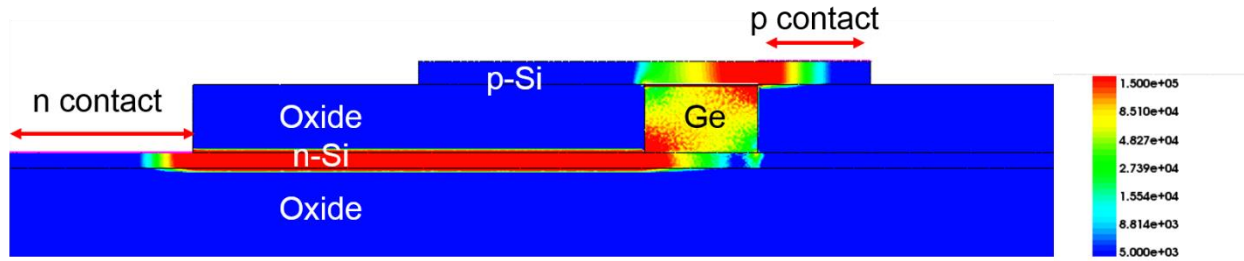


Figure 5.6 Cross section of current injection distribution for a 500 nm wide Ge pnn junction with a diagonal current injection

Structure 4: 1 μm Ge waveguide with a thicker n-Si cladding

From the above three structure simulations, the non-uniform current injection can be mitigated by diagonal current injection and a thinner p-Si cladding. However, all the simulation results show the highest current densities are in the n-Si layer. We then try a thicker n-Si cladding layer to reduce the resistance for current flowing in the n-Si layer. The layers are consisted of a 220 nm thick n-Si cladding with a doping concentration of $1 \times 10^{19} \text{ cm}^{-3}$, a 220 nm thick p-Si cladding with a doping concentration of $1 \times 10^{20} \text{ cm}^{-3}$ and a 200 nm thick n-Ge layer with a doping concentration of $5 \times 10^{19} \text{ cm}^{-3}$ for a 1 μm wide Ge waveguide. Figure 5.7 shows the simulation results with three different metal contact positions. The color maps show that the current densities in Ge and n-Si layer are similar with a thicker n-Si cladding layer. In this case, we achieve a uniform current distribution in both Ge and n-Si, especially in Figure 5.7(c). However, there are a few other challenges with this kind of structure. First is a higher internal optical loss from n-Si and p-Si; the second is the coupling issue between Si and Ge waveguides which will be discussed later and the third is the complexity of processing to fabricate the waveguide coupled devices.

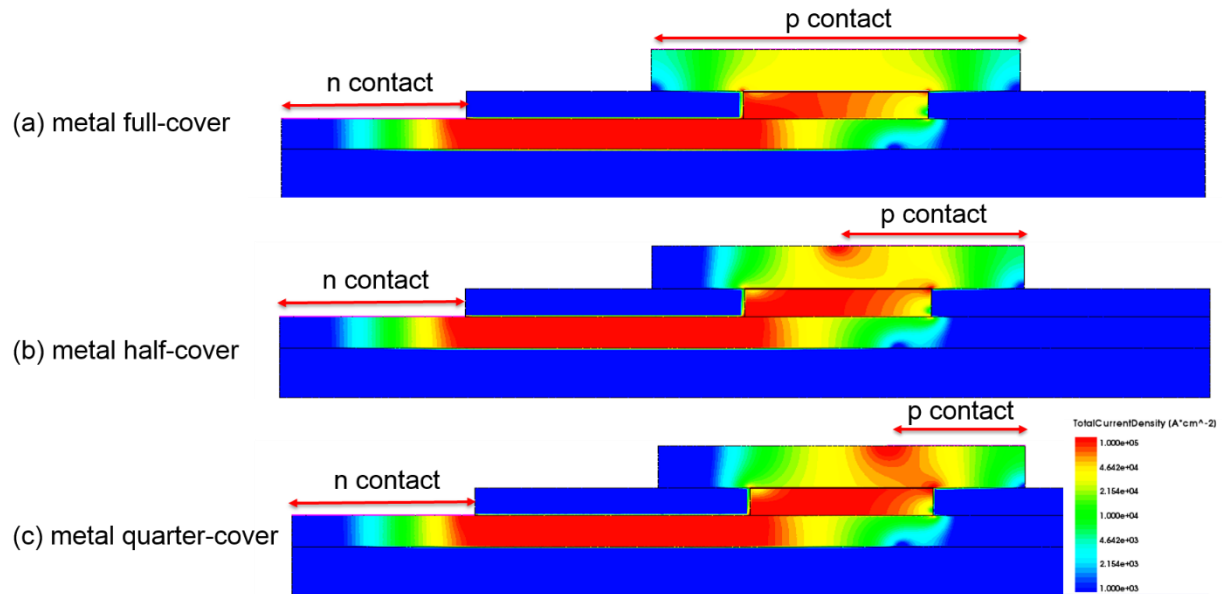


Figure 5.7 Cross section of current injection distribution for Ge pnn junction with a diagonal current injection and a thicker n-Si cladding (a) metal full-cover (b) metal half-cover (c) metal quarter-cover

In conclusion, we find several key layer structures and contact positions designed to achieve low internal optical loss and uniform current injection:

- (1) Thin p-Si cladding layer
- (2) Metal contact away from active Ge
- (3) Diagonal current injection

All the above designs will result in an increased diode resistance and we have to take this into consideration so that the design parameters chosen will not cause a large series resistance. There still remains some problems to solve such as the heating problem using SOI platform, the hot spots at the Ge corners and the high resistance path in the n-Si cladding layer.

5.3 Distributed Bragg Reflector Design and the Corresponding Coupling for Ge Laser on SOI

While current injection and internal optical loss are mainly determined by the electrical properties of the strained Ge material and cladding layers, the lasing mode selection is governed mostly by the optical structures of the device, especially by the mirrors to form a resonant cavity for the Ge gain medium. A Fabry Perot (FP) cavity is the simplest cavity for laser diodes with a reflective mirror on each end. However, the discrete FP laser is not suitable for the integration with other optical components for an optical link. To enable the integration of a Ge laser with other photonic components such as modulators and PDs, the Ge laser has to be fabricated on the SOI platform with the capability to integrate to Si waveguides. In the following section, we will discuss the distributed Bragg reflector (DBR) grating designs to form an external cavity on SOI and the corresponding coupling between Ge and Si waveguides with the focus on mode selection and coupling efficiency. At the end, fabrication process flows will be presented as well as some key processing steps to fabricate a better Ge laser.

5.3.1 Ge DBR Laser Design

A DBR laser can be formed by replacing one or both of the Fabry-Perot mirrors with passive grating reflectors. The grating reflector, also called DBR, is a structure formed by multilayers of alternating materials with varying refractive index or effective refractive index so that the reflections add constructively at some wavelength. The importance of a DBR laser is that we can achieve single axial mode selection with the careful design and a potentially wide tunability, if

the effective index is varied electro-optically or thermal-optically in the different DBR gratings. Figure 5.8 shows a schematic of a Ge DBR laser configuration with two grating mirrors on each side. In this structure, we thin down the Si on SOI substrate for the Ge epitaxial growth and the Ge waveguide is butt-coupled to a single mode Si waveguide. The gratings are formed by etching a periodic structure into the Si waveguide capped by low refractive index material, such as SiO₂ or Si₃N₄. The Ge after selective growth and CMP is slightly higher than the Si waveguide to prevent the possible CMP damage to the Si waveguides and gratings.

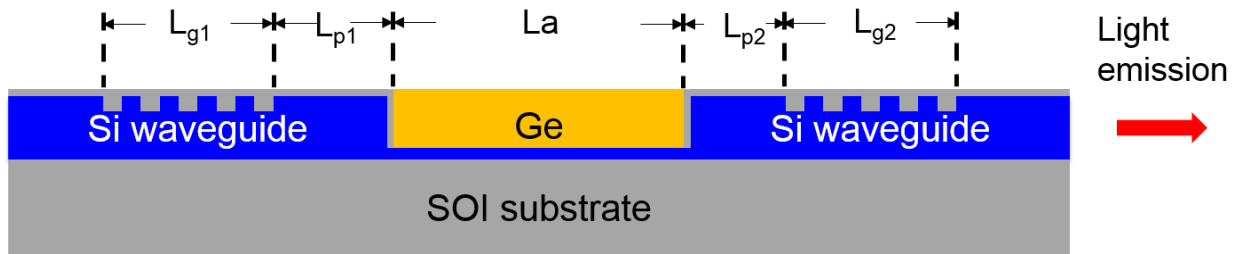


Figure 5.8 Ge DBR laser schematic illustrating various components and the corresponding lengths

There are two key designs for the Ge DBR lasers: (1) the DBR grating designs focuses on the FWHM of the reflectance spectrum and grating reflectivity; (2) the Ge/Si waveguide coupling design focusses on coupling efficiency and reflection at the Ge/Si interface. We will first use Lumerical FDTD simulations to discuss the key parameters for the DBR grating design. The coupling design will be discussed separately in Section 5.3.2.

A typical DBR reflectance spectrum is like $\alpha_m(\lambda)$ in Figure 5.9 with the reflectance peak position at λ_B and the full width half maximum (FWHM) of $\Delta\lambda_{mirror}$. To achieve single mode operation, the FWHM of the DBR reflectance spectrum has to be smaller than two times the

longitudinal mode spacing or free spectral range (FSR), so that only one mode can be reflected and resonated inside the cavity. The FSR can be roughly estimated by Equation 5.5:

$$\Delta\lambda_{mode} = \frac{\lambda_B^2}{2n_{eff}L} \quad (5.5)$$

where λ_B is the Bragg wavelength, n_{eff} is the effective index of the Ge active region and L is the effective cavity length. The mode spacing is around 1.7 nm when the Bragg wavelength is 1.6 μm , the effective index is 3.8 and the effective cavity length is 200 μm . Therefore, the FWHM of the reflectance spectrum from our designed DBR grating has to be smaller than 3.4 nm.

As shown in Figure 5.8, the grating is formed by etching into Si waveguides and then capping with a dielectric layer. The detailed parameters we can vary are the etch depth t , the grating period w and the material for the dielectric cladding layer, while we keep the grating duty cycle to be 1:1. The single mode Si waveguide has a height of 220 nm and a width of 500 nm. The FWHM of the reflectance spectrum is determined by the effective index difference of the grating layers and thus, the etch depth into Si is the dominant device parameter. A shallower etch will result in a smaller effective index change in the Si waveguide. Figure 5.10 plots the reflectance and transmittance spectrums from a Si/SiO₂ DBR gratings with a 25 nm etch depth into Si. The reflectance can reach close to 1 with 120 pairs of gratings and the FWHM is 15 nm. There might be a process uniformity limit with a shallow etch, so it will be very risky to have a even shallower etch than 25 nm.

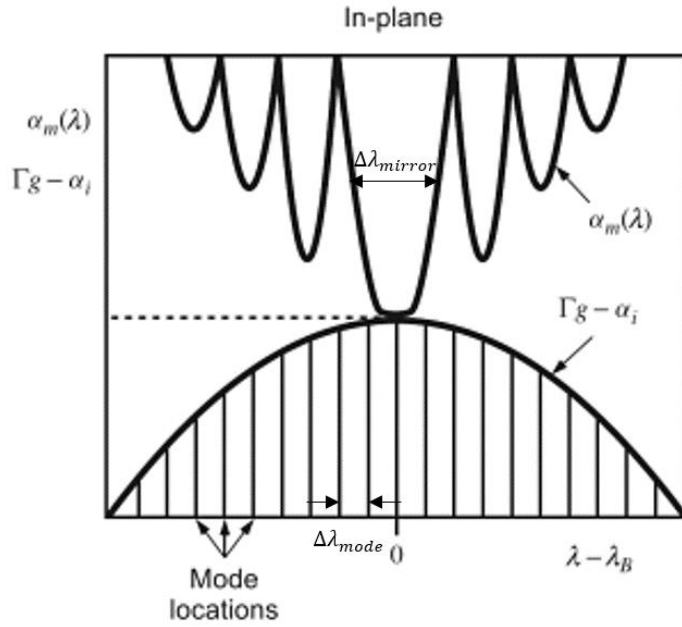


Figure 5.9 Schematic illustration of how a single axial mode is selected in an in-plane DBR laser [85]

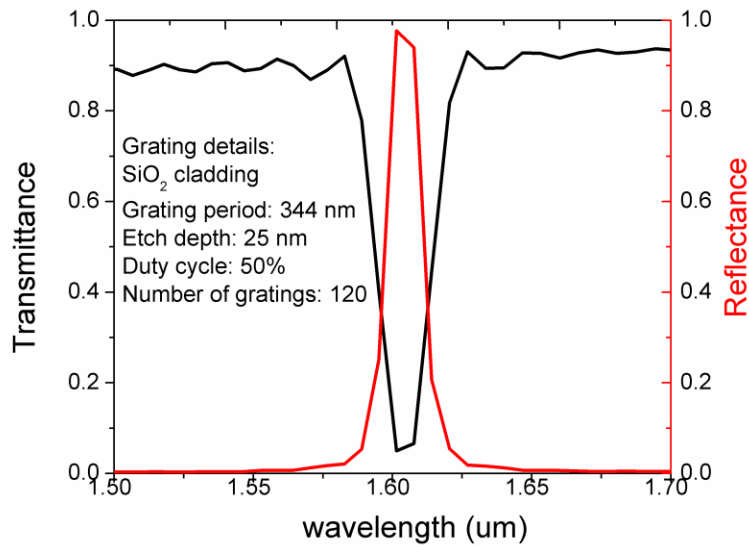


Figure 5.10 Reflectance and transmittance spectrums for a Si/SiO₂ DBR grating with a 25 nm etch depth

We observe a 15 nm FWHM from Figure 5.10 with a reasonably shallow etch into the Si waveguide. Since the spacing between the longitudinal modes in a 200 μm long laser cavity is 1.7 nm, a reflectance spectrum with 15 nm FWHM can support at least 8 longitudinal modes. We then simulate a grating with a 100 nm thick Si_3N_4 film on the Si waveguide and then a 100 nm etch depth into Si_3N_4 with a SiO_2 cladding layer to reduce the effective index difference, as shown in Figure 5.11. Because the majority of mode is still in the Si waveguide, the effective index change by varying the cladding layer on top of the Si waveguide is very small. We can get a 2.5 nm FWHM with the 100 nm thick alternating Si_3N_4 and SiO_2 cladding layers. The Bragg wavelength is 1.6 μm when the grating period is 350 nm with a 50% duty cycle. Due to the limitation of the simulation time and computer memory, we only simulate 400 pairs of gratings and it gives a reflectance of $\sim 20\%$. We expect a higher reflectance with more pairs of such a grating.

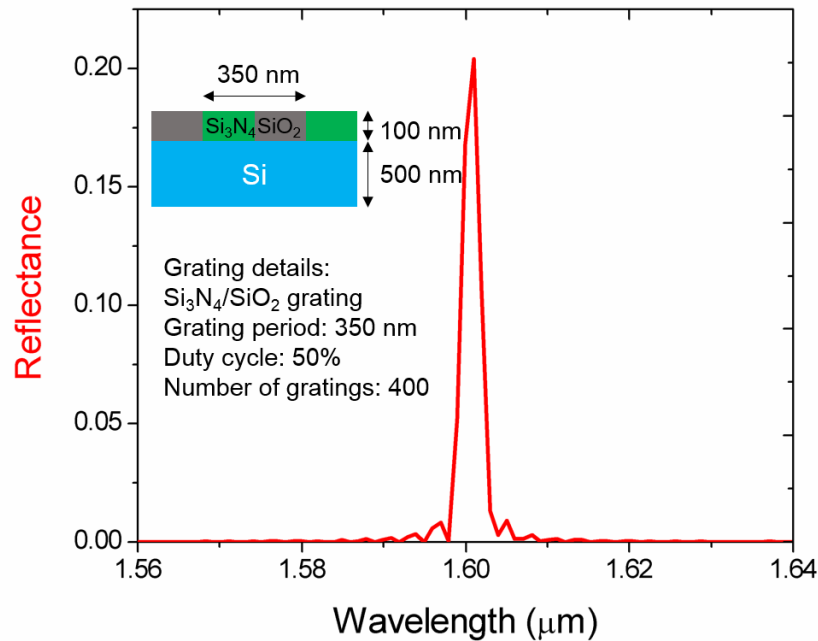


Figure 5.11 Reflectance spectrum for $\text{Si}_3\text{N}_4/\text{SiO}_2$ DBR grating with a 100 nm etch depth

In addition, the number of gratings determines the light transmittance and reflectance. We can then design different pairs for the back mirror and the front mirror in Figure 5.8 so that the reflectance of the back mirror is close to 1 and there is some transmittance of the front mirror for the light emission. The key to achieve the single axial mode operation for a DBR laser is that the FWHM of the grating reflectance spectrum is smaller than two times of the FSR of the resonant cavity. We find that a simple shallow etch on the single mode Si waveguide has a wide FWHM due to the large refractive index of Si material. Instead, using a $\text{Si}_3\text{N}_4/\text{SiO}_2$ DBR grating as shown in Figure 5.11, we can decrease the effective index change and then reach a FWHM of 2.5 nm. We think this kind of grating design can help the Ge DBR laser to realize a single mode operation.

5.3.2 Ge/Si Waveguide Coupling Design

The requirements for the coupling between Ge and Si waveguides are low coupling loss to reduce the threshold current and low reflection to eliminate the formation of a second resonant cavity other than the one previously designed. There are a few challenges regarding to the index mismatch and mode profile mismatch to meet the above two requirements. First, the total thickness of Si/Ge/Si heterojunction is most likely larger than a single mode Si waveguide. Secondly, Ge is a high refractive index material of about 4.2 compared to the refractive index of 3.6 in Si. Thirdly, the width of the Ge active region is also most likely larger than the single mode Si waveguide based on the active region design in Section 5.1. Fourthly, a thin oxide gap between the Ge and Si waveguide in the longitudinal direction is necessary to prevent Ge growth on the Si waveguide sidewall which will result in a disruption of the single crystal epitaxial

growth. We cannot completely eliminate some of the problems but the following designs are trying to mitigate the coupling loss and reflection.

In this design, the key element is that the single mode Si waveguide on SOI is butt-coupled to the Ge active region in order to simplify the fabrication. Figure 5.12 is a schematic view of the off-center coupling, which means the mode center of the active Ge region is not aligned to the mode center of the Si waveguide. We use an FDTD simulation to simulate the mode propagation of the fundamental TE mode in the Ge active region in order to estimate the coupling efficiency from the Ge to the Si waveguide.

First we want to estimate the effect of the oxide gap thickness to the coupling efficiency and reflection. In the simulation, we assume that a fundamental TE mode propagates along the Ge active region to the Si waveguide. The dimension of the Si waveguide is 220 nm high and 500 nm wide. The dimension of the Ge waveguide is 220 nm high and 1 μm wide and Ge is located on a 50 nm thin Si layer as the growth substrate. During the simulation, we locate a power monitor in the Si waveguide to measure the mode transmission which is also directly related to the coupling efficiency and locate another power monitor in the Ge waveguide behind the mode source to measure the mode reflection.

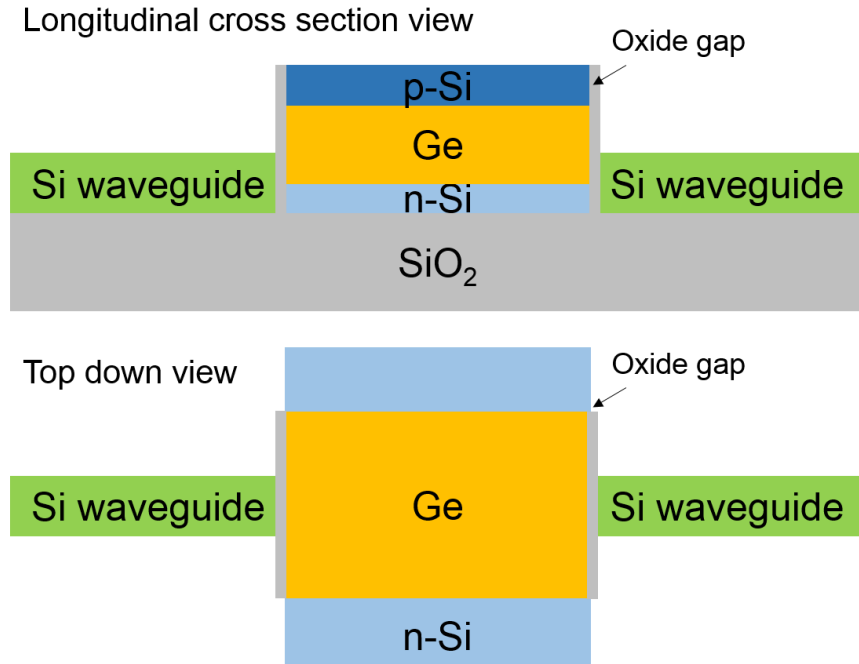


Figure 5.12 Schematics of Ge/Si off-center coupling with both the longitudinal cross section view and top-down view

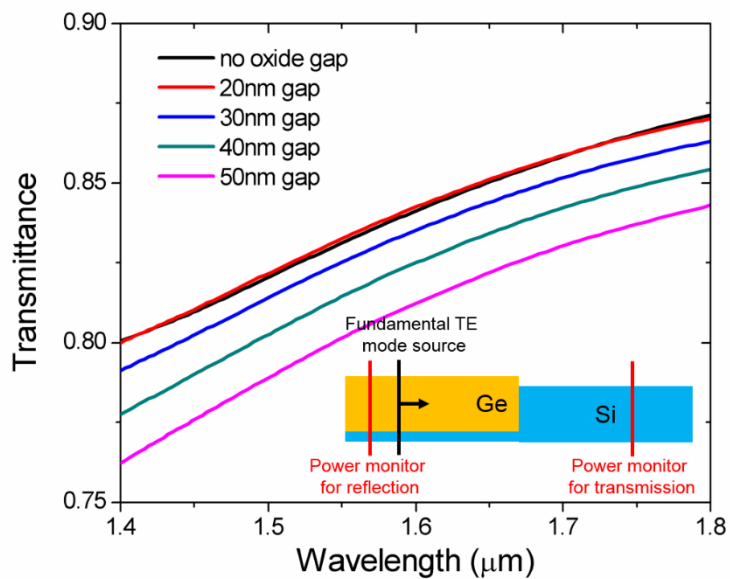


Figure 5.13 Transmittance of the fundamental TE mode from Ge to the Si waveguide for various oxide gaps

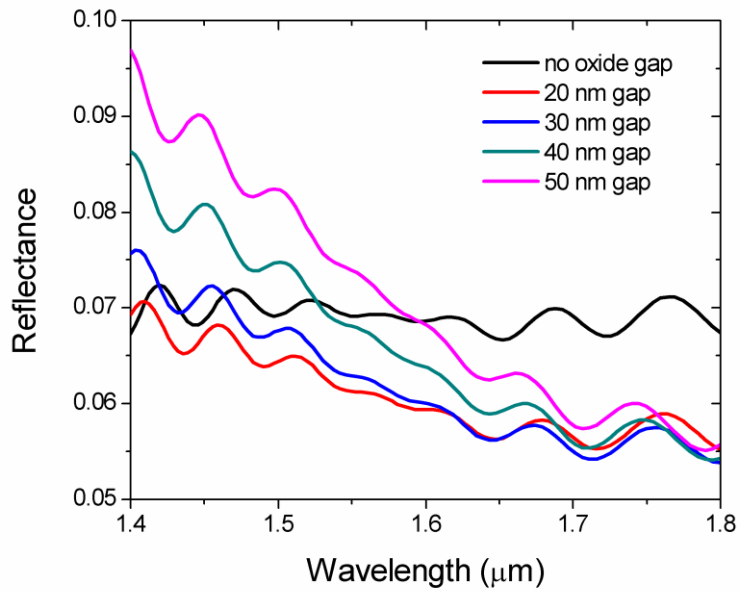


Figure 5.14 Reflectance of fundamental TE mode from Ge to Si waveguide for various oxide gaps

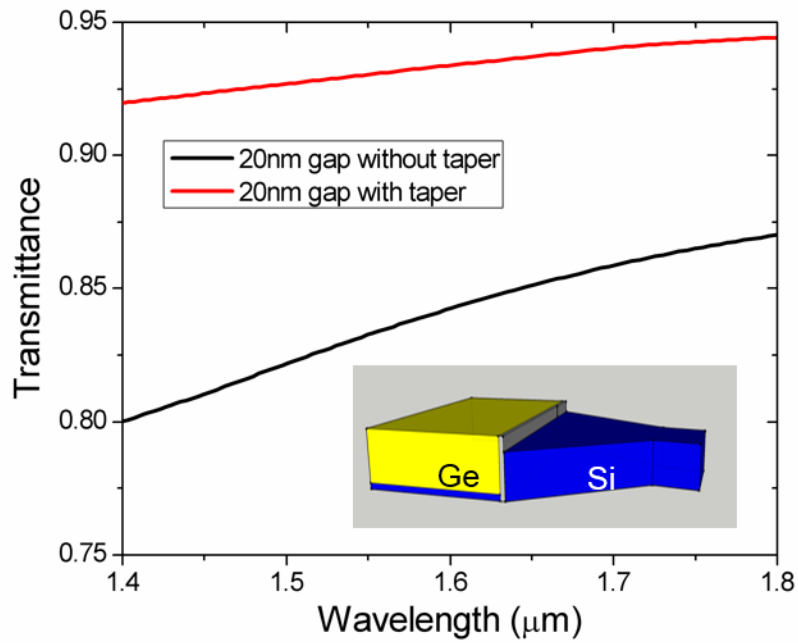


Figure 5.15 Transmittance of a fundamental TE mode from Ge to the tapered Si waveguide with a 20 nm oxide gap

We estimate the mode transmission (Figure 5.13) and reflection (Figure 5.14) for various oxide gaps (no gap, 20 nm gap, 30 nm gap, 40 nm gap and 50 nm gap). The transmittance reduces with a thicker oxide gap due to the scattering loss. The coupling efficiency is ~84% for no oxide gap or a 20 nm oxide gap and it is reduced to 81% for a 50 nm oxide gap at 1.6 μm . It indicates that the coupling efficiency is very sensitive to the oxide gap thickness. It will be a challenge to control the process accuracy to fabricate the oxide gap within the tens of nanometers, which is a requirement for the alignment error of the photolithography to be less than tens of nanometers. If we can fabricate a 20 nm oxide gap between Ge and Si waveguides, the coupling loss is about 1.5 dB. For the reflectance spectrums, all the structures show a reflection of 6% ~ 7% at 1.6 μm , which is due to the effective index difference between the Ge active region and the Si waveguide.

The fundamental method to mitigate the reflection at the Ge/Si waveguide interface is to reduce the effective refractive index difference. We then conduct the simulation with a Si waveguide taper from 1 μm to 500 nm width and a length of 10 μm (inserted figure in Figure 5.15). The transmittance is improved from 84% to 93% and the reflectance is reduced from 6% to 2.5% at 1.6 μm .

Another practical issue is that Ge might be more than 50 nm higher than the Si waveguide. For example, we find that the internal optical loss will go up with a thin Ge gain medium and a reasonable Ge thickness could be 300 nm. In this case, Ge will be 150 nm higher than the Si waveguide if Ge is grown on a 70 nm thick n-Si substrate. Figure 5.16 shows a reduced transmission of 69% labelled as “no height compensation”. The height compensation means that we fabricate a tapered a-Si layer on top of the Si waveguide to compensate the height difference between Ge and c-Si. Although the fabrication process will be complex with an a-Si

taper, the transmittance can then be increased to 91%. The reason is that the a-Si taper facilitates the mode size match at the Ge/Si waveguide interface.

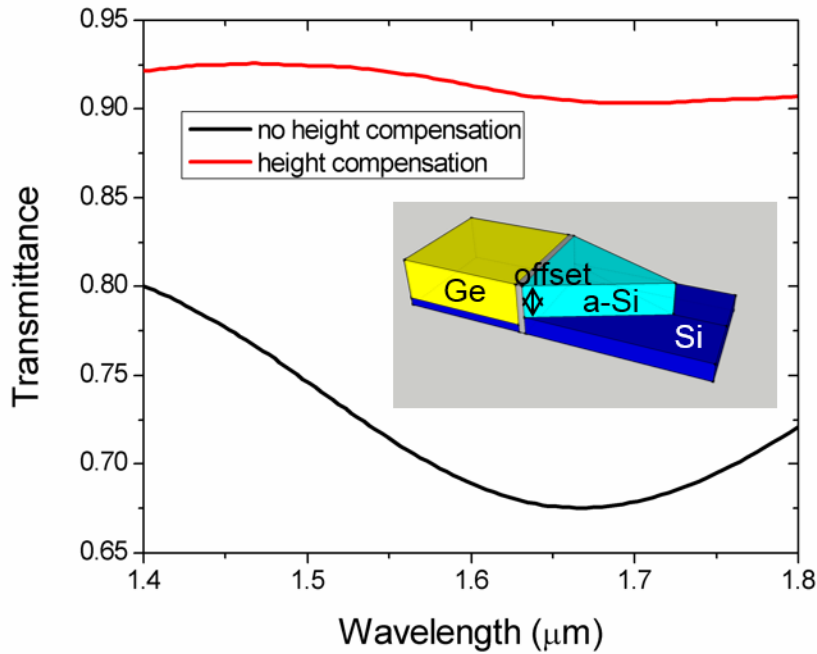


Figure 5.16 Transmittance of the fundamental TE mode from Ge to the Si waveguide with and without height compensation

From the above simulations, we can draw several conclusions for the Ge/Si coupling design:

- (1) The oxide gap between Ge and the Si waveguide has to be as small as possible such as 20 nm although it is a significant challenge for fabrication;
- (2) Tapering the Si waveguide is very efficient to reduce the reflection at the interface to the Ge waveguide;

(3) When we increase the Ge height to reduce the internal optical loss, the coupling efficiency drops dramatically. One solution is to use an a-Si taper on top of the Si waveguide for height compensation.

5.4 Fabrication Process Flows

At the end of this chapter, we will present a detailed process flow to fabricate the Ge DBR laser on the SOI wafer. Figure 5.17 shows a schematic illustration of the process flow. We start with a SOI wafer with 220 nm Si and 1~2 μm SiO_2 . The thickness of Si is chosen by the thickness of a single mode Si waveguide. In Step 1, the wafer is first implanted by phosphorus in a selected area where the Ge will grow and the metal contact will form. The implantation is intended not to amorphize the whole Si because Ge needs to grow epitaxially on the single crystal Si. After the dopant activation by annealing, this part of Si is etched to ~ 70 nm by reactive ion etching.

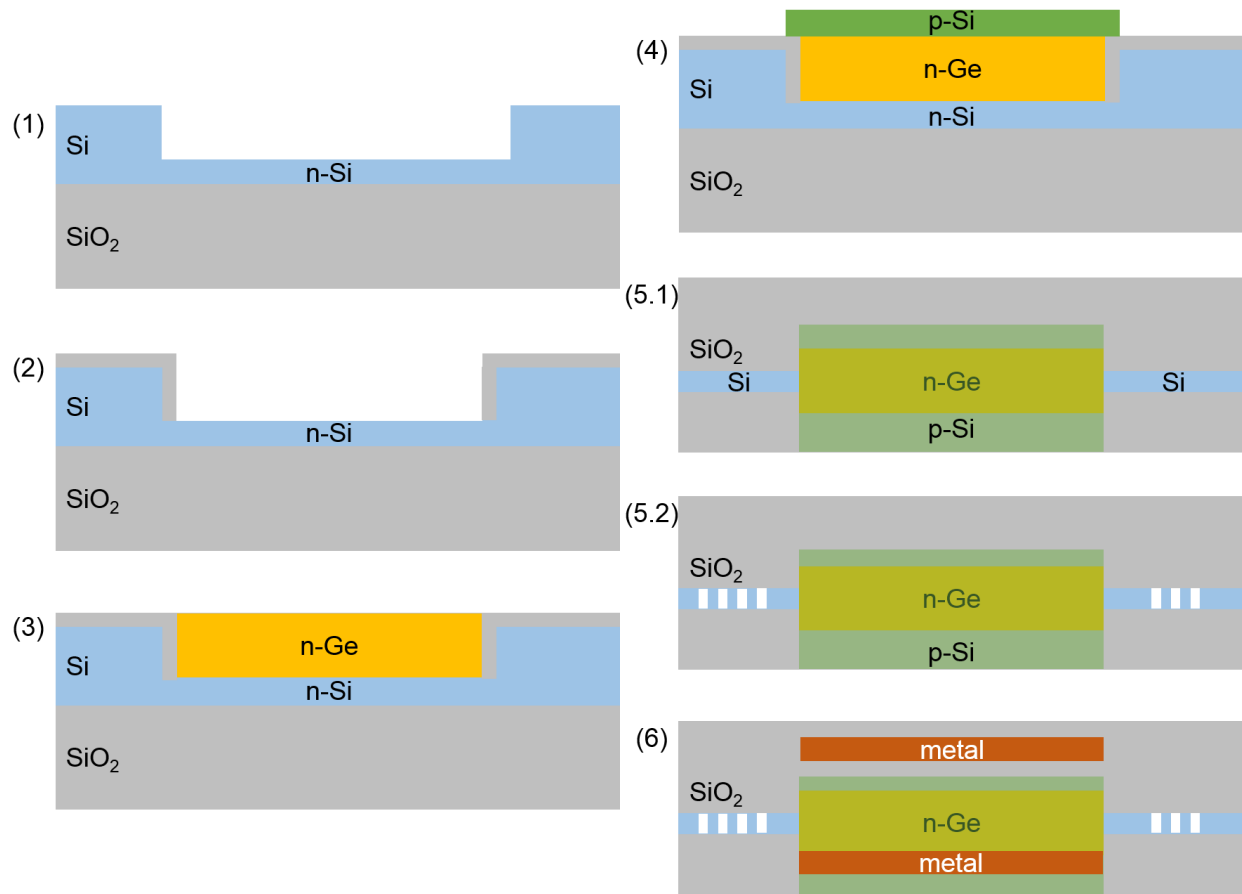


Figure 5.17 Process flow for fabricating a Ge DBR laser on SOI with off-center coupling

In Step 2, we prepare the wafer for the Ge selective growth. We deposit a 300 ~ 500 nm thick oxide layer on the wafer by PECVD and then planarize the oxide by CMP. Then SiO₂ is etched by RIE to form a trench for the Ge growth. In order to prepare a damage-free growth surface, we will not etch through the oxide layer to the Si surface but instead leave a 10~15 nm thick oxide layer and then use buffered oxide etchant (BOE) to remove the last few nanometers of oxide. Another key feature as mentioned before is that the oxide sidewall has to be as vertical as possible for trench filling. In Step 3, n-Ge is grown by UHVCVD with a standard two-step growth and followed by P delta layers as a diffusion source. After the Ge growth, the wafer is

annealed by RTA with a 100 nm oxide cladding layer on top to activate and drive the dopants into the single crystalline Ge. The oxide cap is then removed by BOE and CMP is applied to planarize the Ge waveguide. In Step 4, we deposit the amorphous Si on the planarized wafer instead of the polycrystalline Si. The reason is to expose the wafer to the temperature as low as possible to prevent the dopant out-diffusion from Ge. The amorphous Si has to be annealed in a tube overnight while the temperature is gradually increasing from room temperature to 450 °C in order to out-diffuse H₂ inside of the amorphous layer. The wafer is then sent for boron implantation and then dopant activation at 750 °C for ~ 1min by RTA with the aim to get an active p-type carrier concentration of $1 \times 10^{20} \text{ cm}^{-3}$. The amorphous Si is then etched to only cover Ge as shown in the transparent green rectangular in Step 5.1. In Step 5, we define the single mode silicon waveguides (Step 5.1) and DBR gratings on the Si waveguides (Step 5.2) by dry etching. Step 6 is the metallization and the typical metals we use for contacting are Ti (100 nm)/ Al (1000 nm)/ Ti (100 nm) multi-layers. The metal contact position follows the discussion in Section 5.2.

Chapter Summary

In this chapter, we design an external cavity Ge laser using distributed Bragg reflector (DBR) gratings on Si waveguides. A detailed discussion on the cross section design is presented in order to mitigate the internal optical loss from the cladding and metal layers and also to improve the current injection uniformity across the Ge waveguide. Some key design features are to have thin heavily doped Si cladding layers, to have metal contacts away from the Ge active waveguide and to use a diagonal current injection. The DBR grating design is aimed to achieve single mode operation by controlling the FWHM of the grating reflectance spectrum. A periodic grating of

$\text{Si}_3\text{N}_4/\text{SiO}_2$ on the Si waveguide is proposed to achieve a FWHM of 2.5 nm. We can also change the number of the grating periods to adjust the reflectance and transmittance of the grating. We then discuss the coupling between Ge and the Si waveguide. A thin oxide with the thickness around 20~50 nm is required between the Ge active region and the Si waveguide to keep a high coupling efficiency while avoiding the Ge growth from the Si waveguide sidewall. For the off-centered coupling of a wide Ge waveguide to a single mode Si waveguide, a Si waveguide taper or an a-Si height compensator might be necessary to reduce the coupling loss. In the end of this chapter, we present an example of the process flow to fabricate the Ge DBR laser on the SOI platform with the emphasis on some critical process steps. With all the above designs, we can have an integrable Ge laser on SOI with a lower threshold, higher differential quantum efficiency and single mode emission.

Chapter 6

Summary and Future Work

6.1 Summary

Germanium (Ge) is an optically active material for Silicon-based light emitters with the advantages of Si-CMOS compatibility and monolithic integration. It has great potential to be used as the light emitter for Si photonics. Tensile strain and n-type doping are two key properties of Ge to achieve gain. In Chapter 1, we first described background in Si photonic and then reviewed recent progress in Ge materials and devices for light emission. Finally we discussed the theory in laser physics regarding gain, lasing threshold current and quantum efficiency.

In Chapter 2, we focused on theoretical understandings of Ge gain material and laser performances. Heavy n-type doping was observed to change the Ge electronic band structure by the band gap narrowing effect. We also found a failure of using a simple Drude model to explain

free carrier absorption in n-Ge. We therefore modified the optical gain simulation based on the above two new observations in Ge. We found a broad gain bandwidth of ~ 200 nm from 1550 nm to 1750 nm and a higher net materials gain. We predicted a theoretical lasing threshold current density of $5\sim 10$ kA/cm² in the Ge laser device with the n-type doping concentration of mid- 10^{19} cm⁻³ at room temperature. Additionally, the Ge PL performance with temperature dependence attracted our attentions. The increasing PL with temperature was due to the thermalization of electrons from the indirect L valleys to the direct Γ valley and a further reduction of PL with temperature was found to be related to the non-radiative recombination in Ge. Our simulation explained the PL peak intensity change with temperature very well for n-type doped Ge. We then predicted that the Ge laser device would have a better temperature stability regarding the threshold current than the III-V laser including the non-radiative recombination in n-Ge.

In Chapter 3, we focused on the single crystalline Ge growth on Si in oxide trenches using UHVCVD. The selective growth lead to the faceting in Ge because of the different growth rates of crystal orientations. We developed a suitable photolithography and oxide etch process to get the vertical oxide sidewall for Ge trench filling. We also tested the Ge growth in the T-shape corners to improve the reflectivity at the waveguide end. This T-shape structure would also be useful for Ge/Si waveguide coupling in the external cavity laser. Ge non-buffer growth was explored with different trench openings from 800 nm to 20 μ m. We observed single crystalline growth when the oxide trench width is smaller than 2.25 μ m. Furthermore, we developed a chemical mechanical polishing (CMP) process for the over-grown Ge materials. The Ge CMP process was selective to oxide, flexible to change in the CMP rate by the DI water dilution and controllable for a minimum dishing of Ge in the oxide trenches.

In Chapter 4, we focused on the n-type doping related processes and understandings in Ge. N-type doping helped to increase the direct band transition in Ge for light emission. We developed a delta-doping method to grow a dopant source on the *in situ* doped single crystalline Ge without introducing extra defects into Ge. We then used rapid thermal annealing to drive the dopant into the underlying Ge. The dopant enhanced diffusion was discovered to speed up the drive-in process. The active n-type concentration in Ge was able to reach up to $5 \times 10^{19} \text{ cm}^{-3}$ using the delta doping source and annealing process. A comprehensive dopant diffusion simulation was also developed to predict the annealing temperature and time to achieve high n-type doping and uniform distribution in Ge. Since the dopant source layer had a disrupted Ge growth, we used the developed CMP process to remove it after the dopant drive-in. We also used plan-view transmission electron microscopy to examine the threading dislocation density (TDD) in n-Ge for both blanket films and trench grown waveguides. We found a high TDD of $\sim 1 \times 10^8 \text{ cm}^{-2}$ in the $1 \mu\text{m}$ thick blanket Ge with a doping concentration of $3 \times 10^{18} \text{ cm}^{-3}$ after high temperature annealing at $850 \text{ }^\circ\text{C}$ for 40 min. The TDD was also as high as $1 \times 10^9 \text{ cm}^{-2}$ in the 350 nm thick and $1 \mu\text{m}$ wide Ge waveguide. One possible reason was that the heavy n-type doping resulted in the charged dislocation lines and Coulombic repulsion inhibited the dislocation annihilation. Another possible reason is that the tensile strain in the $1 \mu\text{m}$ wide Ge waveguide is too small to cause dislocations to glide towards the Ge/oxide interface. Further study and understanding was required to lower the threading dislocation density in n-Ge waveguides to make an efficient Ge laser with a lower threshold current.

In Chapter 5, we designed an external cavity Ge laser using distributed Bragg reflector (DBR) gratings on Si waveguides. A detailed discussion on the cross section design was presented to mitigate the internal optical loss from claddings and metal layers and to improve the

current injection uniformity across the Ge waveguide. Some key design features include the thin heavily doped Si cladding layers, the metal contacts not directly above the Ge active waveguide and the diagonal current injection. The aim of the DBR grating design was to achieve a single mode operation by controlling the FWHM of the grating reflectance spectrum. A periodic grating of $\text{Si}_3\text{N}_4/\text{SiO}_2$ on the Si waveguide was proposed to achieve 2.5 nm FWHM. We were able to change the number of the grating periods to adjust the reflectance and transmittance of the grating. We also discussed the coupling between Ge and Si waveguides and different designs were presented to increase the coupling efficiency. A thin oxide around 20~50 nm was required between the Ge active region and the Si waveguide to keep a high coupling efficiency while avoiding Ge growth from the Si waveguide sidewall. For the off-center coupling of a wide Ge waveguide to a single mode Si waveguide, tapered Si waveguides or a-Si height compensators might be necessary to reduce the coupling loss. In the end of this chapter, we presented an example of process flow to fabricate the Ge DBR laser on SOI with the emphasis on some critical process steps.

6.2 Future Work

Ge as a light emitting material has small maturity and its properties have not been fully understood. Ge laser as a recently demonstrated device still needs the performance improvement for the commercial applications, which may take time. There are a lot more to investigate, to understand and to improve regarding Ge materials and devices for light emission.

As mentioned in Chapter 2, higher tensile strain can extend the Ge gain spectrum to mid-IR region while lowering the threshold current. The benefit of undoped Ge with high enough

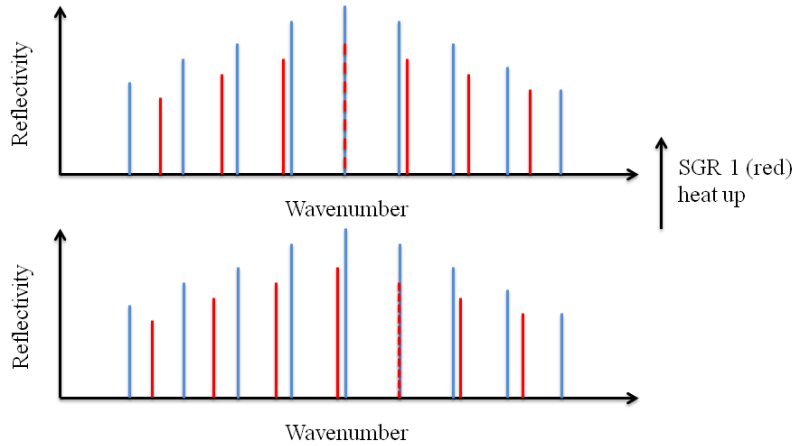
tensile strain is the higher differential quantum efficiency and thus higher power efficiency of Ge laser. The research on Ge mid-IR laser will facilitate the use of Si photonics in mid-IR sensing or imaging applications.

As mentioned in Chapter 4, the threading dislocation density in heavily doped n-Ge is as high as $1 \times 10^8 \sim 1 \times 10^9 \text{ cm}^{-2}$ after the high temperature thermal treatment. The reasons which may prevent the threading dislocations to glide or annihilate are still undetermined. The solution to this problem has not been completely settled. One possibility to keep both high n-type doping and low threading dislocation density is to grow an intrinsic Ge layer with low TDD first and then use dopant diffusion by delta doping diffusion sources or external diffusion sources.

Another problem for the current Si/Ge/Si pnn junction is that Si cladding layers have to be heavily doped to $1 \times 10^{19} \text{ cm}^{-3} \sim 1 \times 10^{20} \text{ cm}^{-3}$ for efficient hole injection and metal contacting. The heavy doping in the Si cladding layer leads to high optical absorption. It would be very beneficial to design some kind of separate confinement heterostructure (SCH) laser as in the III-V quantum well laser to keep optical mode away from contact layers.



(a)



(b)

Figure 6.1 (a) Cavity structure of a widely tunable Ge laser. (b) Lasing mode selection and tuning by aligning the reflection peaks in both spectra of the sampled gratings (SGRs).

Additionally, with our knowledge on the DBR grating laser design, we can use two sampled Bragg gratings (SGRs) incorporated into the laser cavity as reflective mirrors to make a tunable Ge laser. The Ge laser cavity consists of tensile-strained highly doped Ge as the gain medium, a phase tuning section, and two reflective mirrors formed by SGRs (Figure 6.1a). Each grating has a series of periodically placed small grating sections. Since the grating section is repeated in space, its transfer function is periodic in the frequency domain after Fourier transform. This creates a periodic reflection spectrum, with the free spectral range (FSR) determined by the spatial spacing of these grating sections. The wavelength-tuning approach is based on the Vernier effect. As shown in Figure 6.1b, we will use two sampled gratings that have slightly different FSRs on the two sides of the Ge gain medium, corresponding to the red and blue sets of spectral peaks in the reflectivity profiles. When two peaks from each transfer function are aligned, other adjacent peaks will not be aligned due to the slightly different FSRs. In this way, one can choose the lasing wavelength (or frequency) over a relatively large

bandwidth. Tunability will be added, when one or both gratings have a shifted spectrum by thermal or electrical tuning. As an example, we can heat the grating SGR, which causes an increased index and peak wavelength (or a decreased peak wavenumber/frequency), then the two gratings are aligned at an adjacent peak, and the lasing frequency can be moved by one FSR. We can estimate the achievable tuning bandwidth to be about 60 nm, with the two FSRs of nearly 8 nm and a linewidth of 1 nm.

Appendix

Appendix I. Phosphorus Diffusion Modeling in n-Ge

We use MATLAB code to simulate the P diffusion in Ge by FDTD.

```
%% Calculuates the diffusion profile

k1=1.38e-23; % Boltzmann constant
e=1.6e-19; % electron elementary charge
T=673; % temperature for delta layer 400 degree
kT=k1*T/e;

%% time and space grid information

dt = 1; % units of s
dx = 2; % units of nm

t_Ge_0= 600; % thickness of in situ doped germanium in nm
dt_Ge = 20; % thickness of the encapsulating intrinsic Ge
% number of steps in each layer

N_Ge_d = floor(dt_Ge/dx); % number of simulation steps in delta-Ge
N_Ge_0 = floor(t_Ge_0/dx); % number of simulation steps in in situ Ge
N_Ge = floor((t_Ge_0+dt_Ge)/dx); % the total number of step in Ge

x = [0:1:N_Ge]*dx;

%% Diffusion constants with temperature

Nc_Ge=1.04e19;
Nv_Ge=6.0e18;
Eg0_Ge=0.7437;
a_Ge=4.774e-4;
b_Ge=235;
Eg_Ge=Eg0_Ge-a_Ge*T^2/(b_Ge+T); % bandgap of Ge with temperature
n_i_Ge=sqrt(Nc_Ge*Nv_Ge)*(T/300)^1.5*exp(-Eg_Ge/(2*kT)); % intrinsic carrier
concentration in Ge

D_P_Ge_0 = 0.1; % intrinsic diffusivity of P in in situ Ge, units of nm^2/s,
at growth temperature of 400 °C
D_P_Ge_00 = 0.3; % intrinsic diffusivity of P in delta Ge, units of nm^2/s,
at growth temperature of 400 °C

D_P_Ge_1 = 0/n_i_Ge; % single charge diffusivity of P in in situ Ge, at
growth temperature of 400 °C
D_P_Ge_11 = 0/n_i_Ge; % single charge diffusivity of P in delta Ge, at growth
temperature of 400 °C
```

```

D_P_Ge_2 = 0/(n_i_Ge^2); % double charge diffusivity of P in in situ Ge, at
growth temperature of 400 °C
D_P_Ge_22 = 0/(n_i_Ge^2); %double charge diffusivity of P in delta Ge, at
growth temperature of 400 °C

D_P_0 = [D_P_Ge_00*ones(N_Ge_d,1);D_P_Ge_0*ones(N_Ge_0+1,1)];
D_P_1 = [D_P_Ge_11*ones(N_Ge_d,1);D_P_Ge_1*ones(N_Ge_0+1,1)];
D_P_2 = [D_P_Ge_22*ones(N_Ge_d,1);D_P_Ge_2*ones(N_Ge_0+1,1)];
D_P = [D_P_0,D_P_1,D_P_2];
    % ones: returns an m-by-n matrix of ones

%% Initial concentrations

implant_max = 1.53e21; % unit cm^-3
C_P_as_doped = implant_max; % initial P peak concentration in delta layer

C_P_0_L = C_P_as_doped; %Phosphorus, left boundary in cm^-3
C_P_0_R = 7e18; %phosphorus, right boundary in cm^-3
C_P_Ge_0 = 7e18; %Phosphorus, in in situ Germanium in cm^-3
C_P_Ge_d = 1e10; %Phosphorus, in intrinsic delta Germanium in cm^-3
C_P = [C_P_Ge_d*ones(N_Ge_d,1);C_P_0_L;C_P_Ge_0*ones(N_Ge_0,1)]; % Phosphorus
concentration distribution, in cm^-3

%% Compute Second Differential Operator

N = length(C_P);
A = zeros(N); % returns an n-by-n matrix of zeros.

A_k = zeros(1,N); % returns an m-by-n matrix of zeros.
A_k(1) = 1;
A_k(2) = -2;
A_k(3) = 1;

for k = 2:N-1
    A(k,:) = circshift(A_k',k-2)'; % B = circshift(A,shiftsize) circularly
shifts the values in the array, A, by shiftsize elements.
end

A(1)=-1;
A(N+1)=1;
A(N^2)=-2;
A(N*(N-1))=1;

%% To calculate the P concentration depth profile in as grown delta Ge

% First 10min Loops
M1 =600; % simulation steps

for k = 1:M1
    C_P(311)= 7e18;
    C_P = C_P + diff_forward_step_delm3_pileup(C_P,D_P,dt,dx,A);
end

```

```

% Second 10min Loops
C_P_0_L = 1.53e21;
N_Ge_d = floor(dt_Ge*2/dx);
N_Ge_d_2 = floor(dt_Ge/dx);
N_Ge = floor((t_Ge_0+dt_Ge*2)/dx); % add another layer of delta Ge
x = [0:1:N_Ge]*dx; % update the simulation steps
% update the P diffusivity and P concentration
D_P_0 = [D_P_Ge_00*ones(N_Ge_d,1);D_P_Ge_0*ones(N_Ge_0+1,1)];
D_P_1 = [D_P_Ge_11*ones(N_Ge_d,1);D_P_Ge_1*ones(N_Ge_0+1,1)];
D_P_2 = [D_P_Ge_22*ones(N_Ge_d,1);D_P_Ge_2*ones(N_Ge_0+1,1)];
D_P = [D_P_0,D_P_1,D_P_2];
C_P_2 = [C_P_Ge_d*ones(N_Ge_d_2,1);C_P_0_L;C_P(2:N)]; % Phosphorus, in cm^-3

N = length(C_P_2);
A = zeros(N); % returns an n-by-n matrix of zeros.

A_k = zeros(1,N); % returns an m-by-n matrix of zeros.
A_k(1) = 1;
A_k(2) = -2;
A_k(3) = 1;
for k = 2:N-1,
    A(k,:) = circshift(A_k',k-2)';
end
A(1)=-1;
A(N+1)=1;
A(N^2)=-2;
A(N*(N-1))=1;

M2 =600; % simulation steps

for k = 1:M2
    C_P_2(321)= 7e18;
    C_P_2 = C_P_2 + diff_forward_step_delm3_pileup(C_P_2,D_P,dt,dx,A);
end

%%%%%%%%%% Depending on the number of delta layers, we have to repeat the
similar simulation steps to grow new Ge delta layers while P diffuses under
the growth temperature. Because the simulation code is very similar, I will
omit the repeated steps

%% Annealing simulation
T=973; % RTA temperature 700 degree
kT=k1*T/e;
dt = 0.0002; % the simulation time difference

Eg_Ge=Eg0_Ge-a_Ge*T^2/(b_Ge+T); % Ge bandgap at annealing temperature
n_i_Ge=sqrt(Nc_Ge*Nv_Ge)*(T/300)^1.5*exp(-Eg_Ge/(2*kT)); % intrinsic carrier
concentration in Ge at annealing temperature

D_P_Ge_0 = 0; % intrinsic diffusivity of P in in situ Ge, units of nm^2/s,
at annealing temperature of 700 °C
D_P_Ge_00 = 1200; % intrinsic diffusivity of P in delta Ge, units of nm^2/s,
at growth temperature of 700 °C
D_P_Ge_1 = 0/n_i_Ge; single charge diffusivity of P in in situ Ge, units of
nm^2/s, at annealing temperature of 700 °C

```

```

D_P_Ge_11 = 0/n_i_Ge; % single charge diffusivity of P in delta Ge, units of
nm^2/s, at growth temperature of 700 °C
D_P_Ge_2 = 11/(n_i_Ge^2); % double charge diffusivity of P in in situ Ge,
units of nm^2/s, at growth temperature of 700 °C
D_P_Ge_22 = 0/(n_i_Ge^2); % double charge diffusivity of P in delta Ge, units
of nm^2/s, at growth temperature of 700 °C

D_P_0 = [D_P_Ge_00*ones(N_Ge_d,1);D_P_Ge_0*ones(N_Ge_0+1,1)];
D_P_1 = [D_P_Ge_11*ones(N_Ge_d,1);D_P_Ge_1*ones(N_Ge_0+1,1)];
D_P_2 = [D_P_Ge_22*ones(N_Ge_d,1);D_P_Ge_2*ones(N_Ge_0+1,1)];
D_P = [D_P_0,D_P_1,D_P_2];

M10 = 300000; % simulation steps for RTA for 1min

for k = 1:M10
    C_P_9(1)=C_P_9(1)-8.1e19*dt; % 8.1e19 is the P out-diffusion speed at the
surface
    C_P_9(401)=C_P_9(401)+5e20*dt; % 5e20 is the P accumulation speed at the
Ge/Si interface
    C_P_9 = C_P_9+ diff_forward_step_delm3_pileup(C_P_9,D_P,dt,dx,A);
end

% simulation result plot
semilogy(x,C_P_9,'linewidth',5)
ylim([1e17,1e21])
xlim([0,800])
title('delm16o 700C 1min simulation','FontSize',20)
xlabel('depth (nm)','FontSize',15)
ylabel('concentration (cm-3)','FontSize',15)
set(gca,'FontSize',15)

%%%%%%%%% The defined function diff_forward_step_delm3_pileup(C,D,dt,dx,A)

%% to calculate the approximate change in dopant distribution for a given
time step due to 1st, 2nd, 3rd order diffusion.
%'C' is the 1-D vector of concentration versus distance.
%'D' is a length 3 vector containing the diffusion constants in the same
units as 'dx^2/dt/C^k', where 'k' is the index of the diffusion constant
(ie., D0, D1, or D2).
%'dt' is the time step.
%'dx' is the spatial step.
%A is the linear matrix operator approximation to the second derivative
operator with respect to x, 'd^2/dx^2'.
%'Delta_C' is a vector containing the cahange in concentraion as a function
of distance.

function Delta_C = diff_forward_step_delm3_pileup(C,D,dt,dx,A)

D0 = [D(:,1)];
D1 = [D(:,2)];
D2 = [D(:,3)];
C_temp = C;
C_2 = C_temp.*C_temp;
C_3 = C_temp.*C_2;
D_C_temp = (dt/dx^2).*(D0.*(A*C_temp)+(1./2)*D1.*(A*C_2)+(1./3)*D2.*(A*C_3));
Delta_C = D_C_temp(1:end);

```

Appendix II. Electrical Simulation of Ge pnn Junction

We use the commercial software Sentaurus to simulate electron and hole distribution in Si/Ge/Si pnn junction. The physical model and material parameters have been described in detail in Chapter 5. We mainly present the three main simulation code here.

%% The first code is called laser.bnd; It defines the simulation material and structure and metal contact position

```
Silicon "bottom" {cuboid [(0 0 0.5) (5 0.05 0.57)]} % Define bottom n-Si
Germanium "active" {cuboid [(1.5 0 0.57) (2.5 0.05 0.87)]} % Define Ge
Silicon "top" {cuboid [(1 0 0.87) (3 0.05 0.97)]} % Define top p-Si
Oxide "left" {cuboid [(0 0 0.57) (1.5 0.05 0.87)]} % Define left oxide trench
Oxide "right" {cuboid [(2.5 0 0.57) (4 0.05 0.87)]} % Define right oxide trench
Oxide "base" {cuboid [(0 0 0.2) (5 0.05 0.5)]} % Define base oxide on SOI

Contact "p_contact" {rectangle [(1 0 0.97) (1.5 0.05 0.97)]} % Define
metal contact to p-Si
Contact "n_contact_r" {rectangle [(4 0 0.57) (5 0.05 0.57)]} % Define
metal contact to n-Si
```

%% The second code is called laser.cmd; It defines the simulation mesh, doping concentration in each segment

```
Definitions {

    # Define a grid
    Refinement "coarse" {MaxElementSize = (0.025 0.025 0.025)
MinElementSize = (0.01 0.01 0.01)} % Define coarse mesh
    Refinement "fine" {MaxElementSize = (0.01 0.01 0.01) MinElementSize =
(0.002 0.002 0.002)} % Define fine mesh

    # Define Dopings
    Constant "p_plus" {Species = "BoronActiveConcentration" Value = 1.0e+20}
% Define p-type doping concentration in p-Si
    Constant "n_plus" {Species = "PhosphorusActiveConcentration" Value =
1.0e+19} % Define n-type doping concentration in n-Si
    Constant "n_active" {Species = "PhosphorusActiveConcentration" Value =
5.0e+19} % Define n-type doping concentration in n-Ge

}

# Here we place the mesh and doping previously defined

Placements {

    # Place mesh
```

```

    Refinement "bot_oxide" {Reference = "coarse" RefineWindow = cuboid [(0
0 0.2) (5 0.05 0.5)]}
    Refinement "bot_si" {Reference = "fine" RefineWindow = cuboid [(0 0 0.5)
(5 0.05 0.57)]}
    Refinement "ge" {Reference = "fine" RefineWindow = cuboid [(1.5 0 0.57)
(2.5 0.05 0.87)]}
    Refinement "left_oxide" {Reference = "coarse" RefineWindow = cuboid [(0
0 0.57) (1.5 0.05 0.87)]}
    Refinement "right_oxide" {Reference = "coarse" RefineWindow = cuboid
[(2.5 0 0.57) (4 0.05 0.87)]}
    Refinement "top_si" {Reference = "fine" RefineWindow = cuboid [(1 0
0.87) (3 0.05 0.97)]}

    # Place Doping
    Constant "n_si" {Reference = "n_plus" EvaluateWindow {Element = cuboid
[(0 0 0.5) (5 0.05 0.57)] }}
    Constant "p_top" {Reference = "p_plus" EvaluateWindow {Element = cuboid
[(1 0 0.87) (3 0.05 0.97)] }}
    Constant "n_germanium" {Reference = "n_active" EvaluateWindow {Element
= cuboid [(1.5 0 0.57) (2.5 0.05 0.87)] }}

    }

%% The third code is called laser_des.cmd; It defines the physical model to
be used in the simulation, execute and output the simulation results

# Contacts section
Electrode {
    { Name = "n_contact_r" Voltage = 0}
    { Name = "p_contact" Voltage = 0}
}

# File section
File {
    Parameter = "Germanium_mobility_Recombination.par"
    Grid = "laser_msh.grd"
    Doping = "laser_msh.dat"
    Plot = "R_laser_plot_des.dat"
    Current = "R_laser_curr_des.plt"
    Output = "R_laser_out_des.log"
}

# Physics Section
Physics {
    Temperature = 300
    AreaFactor = 1
    Fermi
    EffectiveIntrinsicDensity(noBandGapNarrowing)
    Mobility( ConstantMobility DopingDependence (Masetti))
    Recombination( SRH (DopingDependence))
    HeteroInterface
    Thermionic
}

# Plot Section
Plot {
    eMobility hMobility
    eVelocity hVelocity
    eQuasiFermiPotential hQuasiFermiPotential
    eQuasiFermiEnergy hQuasiFermiEnergy
}

```

```

ElectricField/Vector Potential SpaceCharge
Doping DonorConcentration AcceptorConcentration
TotalCurrent
eCurrent
hCurrent
BandGap Affinity
ConductionBandEnergy ValenceBandEnergy
eEffectiveStateDensity hEffectiveStateDensity
eCurrentDensity hCurrentDensity
EffectiveIntrinsicDensity
IntrinsicDensity
}
# Math Section
Math {
  Method=Pardiso (RecomputeNonSymmetricPermutation IterativeRefinement)
  WallClock
  Extrapolative
  Digits=8
  Notdamped=200
  Iterations=400
  Derivatives
  AvalDerivatives
  RelErrControl
  CNormPrint
  RhSMin=1.0e-07
  RecBoxIntegr
  RhsFactor=1e20
}
# Solve Section
Solve {
  Poisson
  Plugin {Poisson Electron Hole}
  Quasistationary (
    InitialStep=0.01 MaxStep=0.07 MinStep=0.001
    Goal {name="p_contact" voltage=1.5}
  )
  {Plugin {Poisson Electron Hole}}
}
}

```

References

1. Peercy, P.S., *The drive to miniaturization*. Nature, 2000. **406**(6799): p. 1023-1026.
2. Moore, G.E., *Cramming more components onto integrated circuits (Reprinted from Electronics, pg 114-117, April 19, 1965)*. Proceedings of the Ieee, 1998. **86**(1): p. 82-85.
3. www.itrs.net.
4. Shum, C.K., F. Busaba, and C. Jacobi, *IBM ZEC12: THE THIRD-GENERATION HIGH-FREQUENCY MAINFRAME MICROPROCESSOR*. Ieee Micro, 2013. **33**(2): p. 38-47.
5. Moroz, V. *Transition from Planar MOSFETs to FinFETs and its Impact on Design and Variability*. in *CMOSET 2012 VLSI Circuits Devices and Technologies Track*. 2012. Vancouver.
6. Nam Sung, K., *Leakage Current: Moore's Law Meets Static Power*, A. Todd, et al., Editors. 2003. p. 68-75.
7. Thompson, S.E. and S. Parthasarathy, *Moore's law: the future of Si microelectronics*. Materials Today, 2006. **9**(6): p. 20-25.
8. Muller, D.A., *A sound barrier for silicon?* Nature Materials, 2005. **4**(9): p. 645-647.
9. Blake, G., R.G. Dreslinski, and T. Mudge, *A Survey of Multicore Processors A review of their common attributes*. Ieee Signal Processing Magazine, 2009. **26**(6): p. 26-37.
10. Huang, X.J., et al., *Sub-50 nm p-channel FinFET*. Ieee Transactions on Electron Devices, 2001. **48**(5): p. 880-886.
11. Wimer, S., *Planar CMOS to multi-gate layout conversion for maximal fin utilization*. Integration, the VLSI Journal, 2014. **47**(1): p. 115-122.
12. Mark Liu, J.S., Cliff Hou. in *2014 TSMC Technology Symposium*.
13. Brunco, D.P., et al., *Germanium MOSFET devices: Advances in materials understanding, process development, and electrical performance*. Journal of the Electrochemical Society, 2008. **155**(7): p. H552-H561.
14. Heyns, M. and W. Tsai, *Ultimate Scaling of CMOS Logic Devices with Ge and III-V Materials*. Mrs Bulletin, 2009. **34**(7): p. 485-492.
15. Colombeau, B., et al., *Advanced CMOS devices: Challenges and implant solutions*. Physica Status Solidi a-Applications and Materials Science, 2014. **211**(1): p. 101-108.
16. Lim, A.E.J., et al., *Review of Silicon Photonics Foundry Efforts*. Ieee Journal of Selected Topics in Quantum Electronics, 2014. **20**(4): p. 12.
17. Zuffada, M. *Low cost silicon photonics technology platform: plans, perspectives and roadmap*. in *ECOC 2013 - workshop on PICs*. 2013. London.
18. Chen, S., et al. *DSENT - A Tool Connecting Emerging Photonics with Electronics for Opto-Electronic Networks-on-Chip Modeling*. in *Networks on Chip (NoCS), 2012 Sixth IEEE/ACM International Symposium on*. 2012.
19. *Intel, Facebook Collaborate on Future Data Center Rack Technologies*. 2013; Available from: http://newsroom.intel.com/community/intel_newsroom/blog/2013/01/16/intel-facebook-collaborate-on-future-data-center-rack-technologies.
20. *Silicon photonics: big investments, small business*. 2012, Yole Developpement.

21. Cardenas, J., et al., *Low loss etchless silicon photonic waveguides*. Optics Express, 2009. **17**(6): p. 4752-4757.
22. Vlasov, Y. and S. McNab, *Losses in single-mode silicon-on-insulator strip waveguides and bends*. Optics Express, 2004. **12**(8): p. 1622-1631.
23. Bauters, J.F., et al., *Silicon on ultra-low-loss waveguide photonic integration platform*. Optics Express, 2013. **21**(1): p. 544-555.
24. Spencer, D.T., et al. *Integrated Si₃N₄/SiO₂ ultra high Q ring resonators*. in *Photonics Conference (IPC), 2012 IEEE*. 2012.
25. Ishikawa, Y., et al., *Strain-induced enhancement of near-infrared absorption in Ge epitaxial layers grown on Si substrate*. Journal of Applied Physics, 2005. **98**(1): p. -.
26. Luan, H.-C., et al., *High-quality Ge epilayers on Si with low threading-dislocation densities*. Applied Physics Letters, 1999. **75**(19): p. 2909-2911.
27. Yamamoto, Y., et al., *Low threading dislocation density Ge deposited on Si (100) using RPCVD*. Solid-State Electronics, 2011. **60**(1): p. 2-6.
28. Huang, Z.H., et al., *Effectiveness of SiGe buffer layers in reducing dark currents of Ge-on-Si photodetectors*. Ieee Journal of Quantum Electronics, 2007. **43**(3-4): p. 238-242.
29. Yin, T., et al., *31GHz Ge n-i-p waveguide photodetectors on Silicon-on-Insulator substrate*. Optics Express, 2007. **15**(21): p. 13965-13971.
30. Ahn, D., et al., *High performance, waveguide integrated Ge photodetectors*. Optics Express, 2007. **15**(7): p. 3916-3921.
31. Vivien, L., et al., *High speed and high responsivity germanium photodetector integrated in a Silicon-on-insulator microwaveguide*. Optics Express, 2007. **15**(15): p. 9843-9848.
32. Novack, A., et al., *Germanium photodetector with 60 GHz bandwidth using inductive gain peaking*. Optics Express, 2013. **21**(23): p. 28387-28393.
33. Kang, Y., et al., *Monolithic germanium/silicon avalanche photodiodes with 340 GHz gain-bandwidth product*. Nature Photonics, 2009. **3**(1): p. 59-63.
34. Wang, X., et al., *80 GHz bandwidth-gain-product Ge/Si avalanche photodetector by selective Ge growth*. Ofc: 2009 Conference on Optical Fiber Communication, Vols 1-5. 2009. 1164-1166.
35. Bowers, J.E., et al., *High-gain high-sensitivity resonant Ge/Si APD photodetectors*. Infrared Technology and Applications Xxxvi, Pts 1 and 2, 2010. **7660**.
36. Vivien, L., et al., *42 GHz p.i.n Germanium photodetector integrated in a silicon-on-insulator waveguide*. Optics Express, 2009. **17**(8): p. 6252-6257.
37. Soref, R.A. and B.R. Bennett, *Electrooptical effects in Silicon*. Ieee Journal of Quantum Electronics, 1987. **23**(1): p. 123-129.
38. Green, W.M.J., et al., *Ultra-compact, low RF power, 10 gb/s silicon Mach-Zehnder modulator*. Optics Express, 2007. **15**(25): p. 17106-17113.
39. Liu, A., et al., *High-speed optical modulation based on carrier depletion in a silicon waveguide*. Optics Express, 2007. **15**(2): p. 660-668.
40. Dong, P., et al., *Low V-pp, ultralow-energy, compact, high-speed silicon electro-optic modulator*. Optics Express, 2009. **17**(25): p. 22484-22490.
41. Xu, Q., et al., *12.5 Gbit/s carrier-injection-based silicon micro-ring silicon modulators*. Optics Express, 2007. **15**(2): p. 430-436.
42. Timurdogan, E., et al. *Vertical Junction Silicon Microdisk Modulators at 25Gb/s*. in *Optical Fiber Communication Conference/National Fiber Optic Engineers Conference 2013*. 2013. Anaheim, California: Optical Society of America.

43. Liu, J., et al., *Waveguide-integrated, ultralow-energy GeSi electro-absorption modulators*. Nature Photonics, 2008. **2**(7): p. 433-437.
44. Roth, J.E., et al., *Optical modulator on silicon employing germanium quantum wells*. Optics Express, 2007. **15**(9): p. 5851-5859.
45. Jacobsen, R.S., et al., *Strained silicon as a new electro-optic material*. Nature, 2006. **441**(7090): p. 199-202.
46. Chmielak, B., et al., *Pockels effect based fully integrated, strained silicon electro-optic modulator*. Optics Express, 2011. **19**(18): p. 17212-17219.
47. Rong, H.S., et al., *A continuous-wave Raman silicon laser*. Nature, 2005. **433**(7027): p. 725-728.
48. Cloutier, S.G., P.A. Kossyrev, and J. Xu, *Optical gain and stimulated emission in periodic nanopatterned crystalline silicon*. Nature Materials, 2005. **4**(12): p. 887-891.
49. Walters, R.J., G.I. Bourianoff, and H.A. Atwater, *Field-effect electroluminescence in silicon nanocrystals*. Nature Materials, 2005. **4**(2): p. 143-146.
50. Purnawirman, et al., *C- and L-band erbium-doped waveguide lasers with wafer-scale silicon nitride cavities*. Optics Letters, 2013. **38**(11): p. 1760-1762.
51. Groenert, M.E., et al., *Monolithic integration of room-temperature cw GaAs/AlGaAs lasers on Si substrates via relaxed graded GeSi buffer layers*. Journal of Applied Physics, 2003. **93**(1): p. 362-367.
52. Fang, A.W., et al., *Electrically pumped hybrid AlGaInAs-silicon evanescent laser*. Optics Express, 2006. **14**(20): p. 9203-9210.
53. Liang, D. and J.E. Bowers, *Recent progress in lasers on silicon*. Nature Photonics, 2010. **4**(8): p. 511-517.
54. Liang, D., et al., *Electrically-pumped compact hybrid silicon microring lasers for optical interconnects*. Optics Express, 2009. **17**(22): p. 20355-20364.
55. Sun, X., et al., *Electrically pumped hybrid evanescent Si/InGaAsP lasers*. Optics Letters, 2009. **34**(9): p. 1345-1347.
56. Hulme, J.C., J.K. Doyle, and J.E. Bowers, *Widely tunable Vernier ring laser on hybrid silicon*. Optics Express, 2013. **21**(17): p. 19718-19722.
57. Liu, J., et al., *Tensile-strained, n-type Ge as a gain medium for monolithic laser integration on Si*. Optics Express, 2007. **15**(18): p. 11272-11277.
58. Liu, J.F., et al., *Ge-on-Si laser operating at room temperature*. Optics Letters, 2010. **35**(5): p. 679-681.
59. Camacho-Aguilera, R.E., et al., *An electrically pumped germanium laser*. Optics Express, 2012. **20**(10): p. 11316-11320.
60. Fang, Y.Y., et al., *Perfectly tetragonal, tensile-strained Ge on Ge_{1-y}Sn_y buffered Si(100)*. Applied Physics Letters, 2007. **90**(6).
61. Bai, Y., et al., *Growth of highly tensile-strained Ge on relaxed In(x)Ga(1-x)As by metalorganic chemical vapor deposition*. Journal of Applied Physics, 2008. **104**(8).
62. Huo, Y.J., et al., *Strong enhancement of direct transition photoluminescence with highly tensile-strained Ge grown by molecular beam epitaxy*. Applied Physics Letters, 2011. **98**(1): p. 3.
63. de Kersauson, M., et al., *Effect of increasing thickness on tensile-strained germanium grown on InGaAs buffer layers*. Journal of Applied Physics, 2013. **113**(18): p. 7.
64. Lim, P.H., et al., *Enhanced direct bandgap emission in germanium by micromechanical strain engineering*. Optics Express, 2009. **17**(18): p. 16358-16365.

65. Boztug, C., et al., *Tensilely Strained Germanium Nanomembranes as Infrared Optical Gain Media*. *Small*, 2013. **9**(4): p. 622-630.
66. de Kersauson, M., et al., *Optical gain in single tensile-strained germanium photonic wire*. *Optics Express*, 2011. **19**(19): p. 17925-17934.
67. Ghrib, A., et al., *Control of tensile strain in germanium waveguides through silicon nitride layers*. *Applied Physics Letters*, 2012. **100**(20): p. 4.
68. Velha, P., et al. *Process-induced strain bandgap reduction in Germanium nanostructures*. in *Lasers and Electro-Optics (CLEO), 2012 Conference on*. 2012.
69. Simoen, E., et al., *Ion-implantation issues in the formation of shallow junctions in germanium*. *Materials Science in Semiconductor Processing*, 2006. **9**(4-5): p. 634-639.
70. Poon, C.H., et al., *Dopant loss mechanism in n(+)/p germanium junctions during rapid thermal annealing*. *Journal of the Electrochemical Society*, 2005. **152**(12): p. G895-G899.
71. Chui, C.O., et al., *Germanium n-type shallow junction activation dependences*. *Applied Physics Letters*, 2005. **87**(9).
72. Woo-Shik, J., et al. *Enhancement of Phosphorus Dopant Activation and Diffusion Suppression by Fluorine Co-Implant in Epitaxially Grown Germanium*. in *Silicon-Germanium Technology and Device Meeting (ISTDM), 2012 International*. 2012.
73. Kim, J., et al., *Activation of Implanted n-Type Dopants in Ge Over the Active Concentration of $1 \times 10^{20} \text{ cm}^{-3}$ Using Coimplantation of Sb and P*. *Electrochemical and Solid State Letters*, 2010. **13**(1): p. II12-II15.
74. Ding, L., et al., *Dependences of photoluminescence from P-implanted epitaxial Ge*. *Optics Express*, 2012. **20**(8): p. 8228-8239.
75. Janssens, T., et al., *Heavy ion implantation in Ge: Dramatic radiation induced morphology in Ge*. *Journal of Vacuum Science & Technology B*, 2006. **24**(1): p. 510-514.
76. Sun, X., *Ge-on-Si light-emitting materials and devices for silicon photonics*, in *Massachusetts Institute of Technology. Dept. of Materials Science and Engineering*. 2009, Massachusetts Institute of Technology.
77. Oehme, M., J. Werner, and E. Kasper, *Molecular beam epitaxy of highly antimony doped germanium on silicon*. *Journal of Crystal Growth*, 2008. **310**(21): p. 4531-4534.
78. Oehme, M., et al., *Direct bandgap narrowing in Ge LED's on Si substrates*. *Optics Express*, 2013. **21**(2): p. 2206-2211.
79. Yu, H.-Y., et al., *Germanium In Situ Doped Epitaxial Growth on Si for High-Performance n(+)/p-Junction Diode*. *Ieee Electron Device Letters*, 2009. **30**(9): p. 1002-1004.
80. Cheng, S.-L., et al., *Room temperature 1.6 um electroluminescence from Ge light emitting diode on Si substrate*. *Optics Express*, 2009. **17**(12): p. 10019-10024.
81. Nam, D., et al., *Electroluminescence from strained germanium membranes and implications for an efficient Si-compatible laser*. *Applied Physics Letters*, 2012. **100**(13): p. 4.
82. Velha, P., et al., *Direct band-gap electroluminescence from strained n-doped germanium diodes*. 2012 Conference on Lasers and Electro-Optics (Cleo), 2012: p. 2.
83. Sun, X., et al., *Room-temperature direct bandgap electroluminescence from Ge-on-Si light-emitting diodes*. *Optics Letters*, 2009. **34**(8): p. 1198-1200.
84. Camacho-Aguilera, R., et al. *Electroluminescence of highly doped Ge pnn diodes for Si integrated lasers*. in *Group IV Photonics (GFP), 2011 8th IEEE International Conference on*. 2011.

85. Larry A. Coldren, S.W.C., *Diode Lasers and Photonic Integrated Circuits*. 1999: John Wiley & Sons, Inc.
86. Tsai, C.Y., et al., *Theoretical model for intravalley and intervalley free-carrier absorption in semiconductor lasers: Beyond the classical Drude model*. Ieee Journal of Quantum Electronics, 1998. **34**(3): p. 552-559.
87. Wang, X., et al., *Infrared absorption of n-type tensile-strained Ge-on-Si*. Optics Letters, Accepted.
88. Haas, C., *Infrared absorption in heavily doped n-type Germanium*. Physical Review, 1962. **125**(6): p. 1965-&.
89. Wagner, J., *Band-gap narrowing in heavily doped Silicon at 20 and 300K studied by photoluminescence*. Physical Review B, 1985. **32**(2): p. 1323-1325.
90. Camacho-Aguilera, R., et al., *Direct band gap narrowing in highly doped Ge*. Applied Physics Letters, 2013. **102**(15): p. 152106-152106-3.
91. Yan, C., et al., *Analysis of Threshold Current Behavior for Bulk and Quantum-Well Germanium Laser Structures*. Selected Topics in Quantum Electronics, IEEE Journal of, 2013. **19**(4): p. 1901009-1901009.
92. Jain, S.C. and D.J. Roulston, *A simple expression for band gap narrowing (BGN) in heavily doped Si, Ge, GaAs and GexSi1-x strained layers*. Solid-State Electronics, 1991. **34**(5): p. 453-465.
93. Walle, C.G.V.d., *Band lineups and deformation potentials in the model-solid theory*. Physical Review B, 1989. **39**(3): p. 1871-1883.
94. El Kurdi, M., et al., *Band structure and optical gain of tensile-strained germanium based on a 30 band k center dot p formalism*. Journal of Applied Physics, 2010. **107**(1): p. 7.
95. Camacho-Aguilera, R. *Monolithically integrated Ge CMOS laser*. in *Proc. SPIE, Next-Generation Optical Networks for Data Centers and Short-Reach Links*. 2014.
96. Camacho-Aguilera, R.E., et al., *High active carrier concentration in n-type, thin film Ge using delta-doping*. Optical Materials Express, 2012. **2**(11): p. 1462-1469.
97. Cai, Y., et al., *Chemical Mechanical Polishing of Selective Epitaxial Grown Germanium on Silicon*. Ecs Journal of Solid State Science and Technology, 2014. **3**(2): p. P5-P9.
98. Sun, X.C., et al., *Direct gap photoluminescence of n-type tensile-strained Ge-on-Si*. Applied Physics Letters, 2009. **95**(1).
99. http://www.nextnano.com/nextnano3/input_parser/database/docu/effective_masses.htm.
100. Sugawara, Y., et al., *Influence of band alignment on recombination in pseudomorphic Si1-xGex/Si quantum wells*. Applied Physics Letters, 2005. **86**(1): p. -.
101. Chen, Y.-Y., et al., *GeO2 Passivation for Low Surface Recombination Velocity on Ge Surface*. Ieee Electron Device Letters, 2013. **34**(3): p. 444-446.
102. Virgilio, M., et al., *Photoluminescence, recombination rate, and gain spectra in optically excited n-type and tensile strained germanium layers*. Journal of Applied Physics, 2013. **114**(24).
103. Schenk, A., *A model for the field and temperature-dependence of shockley-read-hall lifetimes in silicon*. Solid-State Electronics, 1992. **35**(11): p. 1585-1596.
104. Liu, J., et al., *Tensile-strained, n-type Ge as a gain medium for monolithic laser integration on Si*. Opt. Express, 2007. **15**(18): p. 11272-11277.
105. Tyagi, M.S. and R. Van Overstraeten, *Minority carrier recombination in heavily-doped silicon*. Solid-State Electronics, 1983. **26**(6): p. 577-597.

106. Patel, J.R. and L.R. Testardi, *ELECTRONIC EFFECTS ON DISLOCATION VELOCITIES IN HEAVILY DOPED GERMANIUM*. Applied Physics Letters, 1977. **30**(1): p. 3-5.
107. *Extended Defects in Germanium: Fundamental and Technological Aspects*. Springer Series in Materials Science, ed. E.S. Cor Claeys. 2009: Springer Berlin Heidelberg.
108. Hirth, J.P.N.F.R.N.D.M.S., *Dislocations in solids*. 1979.
109. *Sentaurus Device User Guide*. 2010, Synopsys. Inc. p. Version E-2010.12.
110. Nahory, R.E., M.A. Pollock, and J.C. Dewinter, *Temperature-dependence of InGaAsP double-heterostructure laser characteristics*. Electronics Letters, 1979. **15**(21): p. 695-696.
111. Meyerson, B.S., *Low-temperature silicon epitaxy by ultrahigh vacuum/chemical vapor deposition*. Applied Physics Letters, 1986. **48**(12): p. 797-799.
112. Cannon, D.D., et al., *Germanium-rich silicon-germanium films epitaxially grown by ultrahigh vacuum chemical-vapor deposition directly on silicon substrates*. Applied Physics Letters, 2007. **91**(25): p. -.
113. Fitzgerald, E.A., et al., *TOTALLY RELAXED GEXSII-X LAYERS WITH LOW THREADING DISLOCATION DENSITIES GROWN ON SI SUBSTRATES*. Applied Physics Letters, 1991. **59**(7): p. 811-813.
114. Giovane, L.M., et al., *Correlation between leakage current density and threading dislocation density in SiGe p-i-n diodes grown on relaxed graded buffer layers*. Applied Physics Letters, 2001. **78**(4): p. 541-543.
115. Liu, J., et al., *Deformation potential constants of biaxially tensile stressed Ge epitaxial films on Si(100)*. Physical Review B, 2004. **70**(15): p. 155309.
116. Yu, H.Y., et al., *High-Efficiency p-i-n Photodetectors on Selective-Area-Grown Ge for Monolithic Integration*. Ieee Electron Device Letters, 2009. **30**(11): p. 1161-1163.
117. Liu, J., *GeSi photodetectors and electro-absorption modulators for Si electronic-photonic integrated circuits*, in *Department of Materials Science and Engineering*. 2007, Massachusetts Institute of Technology.
118. Jones, S.H., et al., *Patterned substrate epitaxy surface shapes*. Journal of Crystal Growth, 1991. **108**(1-2): p. 73-88.
119. Camacho-Aguilera, R.E., et al., *Ge-on-Si Bufferless Epitaxial Growth for Photonic Devices*. ECS Transactions, 2013. **50**(9): p. 469-473.
120. Liu, J., *GeSi Photodetectors and Electro-absorption Modulators for Si Electronic-photonic Integrated Circuits*. 2007, Massachusetts Institute of Technology.
121. Camacho-Aguilera, R.E., et al., *High active carrier concentration in n-type, thin film Ge using delta-doping*. Opt. Mater. Express, 2012. **2**(11): p. 1462-1469.
122. Ong, P., et al., *Ge- and III/V-CMP for Integration of High Mobility Channel Materials*, in *China Semiconductor Technology International Conference 2011*, H. Wu, et al., Editors. 2011. p. 647-652.
123. Hydrick, J.M., et al., *Chemical Mechanical Polishing of Epitaxial Germanium on SiO₂-patterned Si(001) Substrates*, in *Sige, Ge, and Related Compounds 3: Materials, Processing, and Devices*, D. Hara, et al., Editors. 2008. p. 237-248.
124. Peddeti, S., et al., *Chemical Mechanical Polishing of Ge Using Colloidal Silica Particles and H₂O₂*. Electrochemical and Solid State Letters, 2011. **14**(7): p. H254-H257.

125. Peddetti, S., et al., *Chemical mechanical planarization of germanium shallow trench isolation structures using silica-based dispersions*. Microelectronic Engineering, 2012. **93**: p. 61-66.
126. Matovu, J.B., et al., *Chemical Mechanical Polishing of Ge in Hydrogen Peroxide-Based Silica Slurries: Role of Ionic Strength*. Journal of the Electrochemical Society, 2011. **158**(11): p. H1152-H1160.
127. Xia, X. and G. Ahmadi, *Surface removal rate in chemical-mechanical polishing*. Particulate Science and Technology, 2002. **20**(3): p. 187-196.
128. Stine, B.E., et al., *Rapid characterization and modeling of pattern-dependent variation in chemical-mechanical polishing*. Ieee Transactions on Semiconductor Manufacturing, 1998. **11**(1): p. 129-140.
129. Trumbore, F.A., et al., *Solid Solubilities of Antimony, Arsenic, and Bismuth in Germanium from a Saturation Diffusion Experiment*. Journal of the Electrochemical Society, 1962. **109**(8): p. 734-738.
130. I. Barin, O.K., O. Kubaschewski, *Thermo-chemical Properties of Inorganic Substances*. 1973, New York: Springer-Verlag.
131. V. I. Fistul, A.G.Y., A. A. Gvelesiani, V. N. Tsygankov, R. L. Korchazhkina, *Solubility and Segregation of Electrically Active Phosphorus in Ge*. Izv. Akad. Nauk SSSR, Neorg. Mater, 1975. **11**: p. 539-541.
132. Zakharov, N.D., Rozhansk.Vn, and Korchazh.Rl, *Defects Appearing under Precipitation of Solid-Solution of Phosphorus in Germanium*. Fizika Tverdogo Tela, 1974. **16**(5): p. 1444-1450.
133. R. W. Olesinski, N.K., G. J. Abbaschian, *The Ge-P (Germanium-Phosphorus) System*. Bulletin of Alloy Phase Diagrams, 1985. **6**(3): p. 262-266.
134. Tsai, H.W. and D.S. Lin, *Comparison of thermal reactions of phosphine on Ge(100) and Si(100) by high-resolution core-level photoemission*. Surface Science, 2001. **482**: p. 654-658.
135. Brückner, S., *Atomic scale in situ control of Si(100) and Ge(100) surfaces in CVD ambient in Mathematics and Natural Sciences*. 2013, Humboldt University.
136. Leycuras, A., *Arsenic segregation and passivation in the heteroepitaxy of Ge/GaAs*. Applied Physics Letters, 1995. **66**(14): p. 1800-1802.
137. Sun, X., et al., *Optical Bleaching of Thin Film Ge on Si*. ECS Trans., 2008. **16**(10): p. 881-883.
138. Goh, K.E.J., et al., *Effect of encapsulation temperature on Si : P delta-doped layers*. Applied Physics Letters, 2004. **85**(21): p. 4953-4955.
139. Oberbeck, L., et al., *Encapsulation of phosphorus dopants in silicon for the fabrication of a quantum computer*. Applied Physics Letters, 2002. **81**(17): p. 3197-3199.
140. Schubert, E.F., *DELTA DOPING OF III-V-COMPOUND SEMICONDUCTORS - FUNDAMENTALS AND DEVICE APPLICATIONS*. Journal of Vacuum Science & Technology a-Vacuum Surfaces and Films, 1990. **8**(3): p. 2980-2996.
141. Scappucci, G., et al., *Phosphorus atomic layer doping of germanium by the stacking of multiple delta layers*. Nanotechnology, 2011. **22**(37).
142. Scappucci, G., G. Capellini, and M.Y. Simmons, *Influence of encapsulation temperature on Ge:P delta-doped layers*. Physical Review B, 2009. **80**(23).
143. Yamamoto, Y., et al., *Phosphorus atomic layer doping in Ge using RPCVD*. Solid-State Electronics, 2013. **83**: p. 25-29.

144. Fazio, A., et al., *Microscopic picture of the single vacancy in germanium*. Physical Review B, 2000. **61**(4): p. R2401-R2404.
145. Werner, M., H. Mehrer, and H.D. Hochheimer, *Effect of hydrostatic-pressure, temperature, and doping on self-diffusion in Germanium*. Physical Review B, 1985. **32**(6): p. 3930-3937.
146. Bracht, H. and S. Brotzmann, *Atomic transport in germanium and the mechanism of arsenic diffusion*. Materials Science in Semiconductor Processing, 2006. **9**(4-5): p. 471-476.
147. Brotzmann, S. and H. Bracht, *Intrinsic and extrinsic diffusion of phosphorus, arsenic, and antimony in germanium*. Journal of Applied Physics, 2008. **103**(3).
148. Cannon, D.D., *Strain-engineered CMOS-compatible germanium photodetectors*. 2003, Massachusetts Institute of Technology: Cambridge, Massachusetts, United States.
149. Fahey, P.M., P.B. Griffin, and J.D. Plummer, *Point-defects and dopant diffusion in silicon*. Reviews of Modern Physics, 1989. **61**(2): p. 289-384.
150. Normand, P., et al., *A pile-up phenomenon during Arsenic diffusion in silicon-on-insulator structures formed by oxygen implantation*. Journal of Applied Physics, 1989. **66**(8): p. 3585-3589.
151. Tsouroutas, P., et al., *Modeling and experiments on diffusion and activation of phosphorus in germanium*. Journal of Applied Physics, 2009. **105**(9).
152. Carroll, M.S. and R. Koudelka, *Accurate modelling of average phosphorus diffusivities in germanium after long thermal anneals: evidence of implant damage enhanced diffusivities*. Semiconductor Science and Technology, 2007. **22**(1): p. S164-S167.
153. Chui, C.O., et al., *Activation and diffusion studies of ion-implanted p and n dopants in germanium*. Applied Physics Letters, 2003. **83**(16): p. 3275-3277.
154. Bartels, A., E. Peiner, and A. Schlachetzki, *THE EFFECT OF DISLOCATIONS ON THE TRANSPORT-PROPERTIES OF III/V-COMPOUND SEMICONDUCTORS ON SI*. Journal of Applied Physics, 1995. **78**(10): p. 6141-6146.
155. Luan, H.-C., *Ge photodetectors fo Si microphotronics*. 2001, Massachusetts Institute of Technology.
156. Wang, G., et al., *A model of threading dislocation density in strain-relaxed Ge and GaAs epitaxial films on Si (100)*. Applied Physics Letters, 2009. **94**(10).
157. Patel, J.R. and Chaudhur.Ar, *CHARGED IMPURITY EFFECTS ON DEFORMATION OF DISLOCATION-FREE GERMANIUM*. Physical Review, 1966. **143**(2): p. 601-&.
158. Luong, T.K.P., et al., *Control of tensile strain and interdiffusion in Ge/Si(001) epilayers grown by molecular-beam epitaxy*. Journal of Applied Physics, 2013. **114**(8).
159. Silvestri, H.H., et al., *Diffusion of silicon in crystalline germanium*. Semiconductor Science and Technology, 2006. **21**(6): p. 758-762.
160. Fitzgerald, E.A., et al., *Dislocations in relaxed SiGe/Si heterostructures*. Physica Status Solidi a-Applied Research, 1999. **171**(1): p. 227-238.
161. Masetti, G., M. Severi, and S. Solmi, *MODELING OF CARRIER MOBILITY AGAINST CARRIER CONCENTRATION IN ARSENIC-DOPED, PHOSPHORUS-DOPED, AND BORON-DOPED SILICON*. Ieee Transactions on Electron Devices, 1983. **30**(7): p. 764-769.
162. Hellings, G., et al., *Electrical TCAD Simulations of a Germanium pMOSFET Technology*. Ieee Transactions on Electron Devices, 2010. **57**(10): p. 2539-2546.